SAKARYA UNIVERSITY
JOURNAL OF SCIENCE

SAKARYA
ÜNİVERSİTESİ

i

Osman Sönmez
Department of Civil Engineering
Sakarya University
Sakarya - Türkiye
osonmez@sakarya.edu.tr

Serap Coşansu
Department of Food Engineering
Sakarya University
Sakarya - Türkiye
scosansu@sakarya.edu.tr

Tahsin Turgay
Department of Architecture
Sakarya University
Sakarya - Türkiye
turgay@sakarya.edu.tr

Ufuk Durmaz
Department of Mechanical Engineering
Sakarya University
Sakarya - Türkiye
udurmaz@sakarya.edu.tr

Section Editor (Civil Engineering)

Issa Al-Harthy
Department of Civil and Architectural Engineering
Sultan Qaboos University
Oman
aissa@squ.edu.om

Jamal Khatib
Department of Civil Engineering
University of Wolverhampton
United Kingdom
jmkhatib@wlv.ac.uk

Khalifa Al-Jabri
Department of Civil and Architectural Engineering
Sultan Qaboos University
Oman
aljabri@squ.edu.om

Hakan Alp
Department of Geophysical Engineering
İstanbul University-Cerrahpaşa
İstanbul - Türkiye
hakanalp@iuc.edu.tr

Tuba Tatar
Department of Civil Engineering
Sakarya University
Sakarya - Türkiye
ttatar@sakarya.edu.tr

Gökhan Dok
Department of Civil Engineering
Sakarya University of Applied Sciences
Sakarya - Türkiye
gokhandok@subu.edu.tr

Section Editor (Chemistry)

Can Serkan Keskin
Department of Chemistry
Sakarya University
Sakarya - Türkiye
ckeskin@sakarya.edu.tr

Murat Tuna
Department of Chemistry
Sakarya University
Sakarya - Türkiye
tuna@sakarya.edu.tr

Nahit Gencer
Department of Biochemistry
Balıkesir University
Sakarya - Türkiye
ngencer@balikesir.edu.tr

Section Editor (Biology)

Sezen Toksoy Köseoğlu
Department of Biology
Sakarya University
Sakarya - Türkiye
sezentoksoy@sakarya.edu.tr

Nihan Akıncı Kenanoglu
Department of Biology
Çanakkale Onsekiz Mart University
Çanakkale - Türkiye
nakinci@comu.edu.tr

Oğuz Kurt
Department of Biology
Manisa Celal Bayar University
Manise - Türkiye
oguz.kurt@cbu.edu.tr

Sezgi Somuncu
Department of Biology
Sakarya University
Sakarya - Türkiye
sezgisomuncu@sakarya.edu.tr

Section Editor (Mathematics)

Murat Sarduvan
Department of Mathematics
Sakarya University
Sakarya - Türkiye
msarduvan@sakarya.edu.tr

Selma Özçağ
Department of Mathematics
Hacettepe University
Ankara - Türkiye
sozcag@hacettepe.edu.tr

Necati Olgun
Department of Mathematics
Gaziantep University
Gaziantep - Türkiye
olgun@gantep.edu.tr

Ali Demir
Department of Mathematics
Kocaeli University
Kocaeli - Türkiye
ademir@kocaeli.edu.tr

Section Editor (Computer Science and Engineering)

Fahrettin Horasan
Computer Science and Engineering
Kırıkkale University
Kırıkkale - Türkiye
fhorasan@kku.edu.tr

Kevser Ovaz Akpınar
Computer Science and Engineering
Rochester Dubai Institute of Technology
Dubai
kxocad1@rit.edu

Muhammed Maruf Öztürk
Computer Science and Engineering
Süleyman Demirel University
Isparta - Türkiye
muhammedozturk@sdu.edu.tr

Mustafa Akpinar
Computer Science and Engineering
High Tech Collages
United Arab Emirates
mustafakpinar@gmail.com

Section Editor (Physics)

Ceren Tayran
Department Physics
Gazi University
Ankara - Türkiye
c.tayran@gazi.edu.tr

Section Editor (Industrial Engineering)

Feyza Gürbüz
Department Industrial Engineering
Erciyes University
Kayseri - Türkiye
feyza@erciyes.edu.tr

Mehmet Emin Aydın
Department Industrial Engineering
University of The West of England Bristol
England
mehmet.aydin@uwe.ac.uk,

Barış Yüce
Department Industrial Engineering
University of Exeter
United Kingdom
b.yuce@exeter.ac.uk

Benjamin Durakovic
Department Industrial Engineering
International University of Sarajevo
Bosnia and Herzegovina
bdurakovic@ius.edu.ba

Section Editor (Mechanical Engineering)

Elif Eker Kahveci
Department of Mechanical Engineering
Sakarya University
Sakarya - Türkiye
eeker@sakarya.edu.tr

Erman Aslan
Department of Mechanical Engineering
Kocaeli University
Kocaeli - Türkiye
erman.aslan@kocaeli.edu.tr

Abderrahmane Benbrik
Department of Mechanical Engineering
M'hamed Bougara University
Egypt
abderrahmane.benbrik@univ-boumerdes.dz

Ali Cemal Benim
Department of Mechanical Engineering
Düsseldorf University of Applied Sciences
Germany
alicemal@prof-benim.com

Shi-Chune Yao
Department of Mechanical Engineering
Carnegie Mellon University
USA
sy0d@andrew.cmu.edu

Section Editor
(Environmental Sciences and Engineering)

Senay Çetin Doğruparmak
Department of Environmental Engineering
Kocaeli University
Kocaeli - Türkiye
senayc@kocaeli.edu.tr

Section Editor (Food Science)

Aslı Uçar
Department of Food Sciences
Ankara University
Ankara - Türkiye
aucar@ankara.edu.tr

Section Editor
(Electrical and Electronics Engineering)

Francesco De Paulis
Department of Electrical and Electronics Engineering
L'Aquila University
Italy
francesco.depaulis@univaq.it

Rıfkı Terzioğlu
Department of Electrical and Electronics Engineering
Bolu Abant Izzet Baysal University
Bolu - Türkiye
rifkiterzioğlu@ibu.edu.tr

Section Editor (Architecture)

İsmail Hakkı Demir
Department of Architecture
Sakarya University
Sarkaya - Türkiye
idemir@sakarya.edu.tr

Section Editor (Materials Science)

Miraç Alaf
Department Metallurgical and Materials Engineering
Bilecik Şeyh Edebali University
Bilecik - Türkiye
mirac.alaf@bilecik.edu.tr

English Language Editor

Seçkin Arı
Department of Computer Engineering
Sakarya University, Sakarya-Türkiye
ari@sakarya.edu.tr

Editorial Assistant

Evrim Yüksel
Department of Environmental Enginering
Instıtute of Sciences, Sakarya University
Sakarya-Türkiye
eyuksel@sakarya.edu.tr

Statistical Editor

Önder Gökmen Yıldız
Department of Mathematics
Bilecik Şeyh Edebali University, Bilecik-Türkiye
ogokmen.yildiz@bilecik.edu.tr

Indexing

Scopus®

DOAJ

TÜBİTAK
ULAKBİM
TR DİZİN

ERIHPLUS
EUROPEAN REFERENCE INDEX FOR THE
HUMANITIES AND SOCIAL SCIENCES

Academic Search Premier
EBSCOhost

Business Source® Premier

Business Source® Elite

Contents

Synthesis of SiO2 NPs from Sodium Bentonite and their Use in Photocatalytic Activity and Adsorption Applications

Abdulmuin Elkatuf [iD], Nurşah Kütük* [iD]

Sivas Cumhuriyet University, Faculty of Engineering, Deparment of Chemical Engineering, Sivas, Türkiye, muinka34@gmail.com, nkutuk@cumhuriyet.edu.tr, ror.org/04f81fm77
*Corresponding Author

ARTICLE INFO	ABSTRACT
	Silica nanoparticles (SiO$_2$ NPs) are a material that is used in many areas and are obtained by various methods and attracts the attention of researchers with its many properties such as photocatalysis, adsorbent and non-toxicity. In this study, sodium bentonite was used as a raw material to synthesize silica nanoparticles. In the FTIR results of the prepared SiO$_2$ NPs, the Si-O-Si band indicating the formation of NPs is remarkable. The morphology structure was determined to be an agglomerated structure similar to a spherical form in SEM images. In the other part of the study, the photocatalytic degradation of methylene blue (MB) dye was investigated with SiO$_2$ NPs. The results revealed that 80% degradation was achieved in 60 min and the process complied with the second order reaction kinetics. The effect of MB in aqueous solution was investigated for its use as an adsorbent. After 60 minutes, 90% dye removal was achieved and it was determined that the process fit pseudo-second-order kinetic model (PSO).

1. Introduction

Nanotechnology is a multidisciplinary science with synthesis methods and application areas that emerged in the 21st century [1]. The term nanoparticle represents materials with a size between 1-100 nm and at least one dimension. At these small sizes, particles change their properties due to the laws of quantum mechanics [2]. Nanotechnological developments are emerging in many application areas such as drug delivery, sensors, diagnostics, bioimaging, agriculture, food and water treatment [1, 3–5]. Nanoparticles of many metal and metal oxide elements are synthesized and attract the attention of researchers [4].

Silica (SiO2) is a compound that is abundant and widespread throughout the world, including plants and grains [6]. Silica-based nanoparticles are important materials due to their easy preparation, high surface functionality, particle size adjustable during synthesis, and biocompatible properties [3]. Amorphous silica in particular is widespread in nature and is used in various applications [7]. According to research, silica nanoparticles are the 2nd most produced nano-sized material in the world. For this reason, research on the subject has diversified [6].

Bentonite is known as a clay that is a good source of silica. It contains aluminum and silica together. Acid and alkali exposures are used successively to try to separate these components from each other [8]. It can be divided into two depending on whether it contains Na and Ca ions. Sodium bentonite has a high water absorption capacity due to the Na ion it contains [9].

Water pollution is a problem that deeply affects human life. There are many methods for cleaning water in addition to membrane, adsorption,

photodegradation, chemical oxidation, precipitation, osmosis and filtration [10, 11]. However, some of these methods take time and cause new waste materials to emerge [11]. The use of photocatalytic properties of nanoparticles for the removal of pollutants in water pollution treatment has attracted attention in recent years. Because the specific surface area is important at this point. A good photocatalyst is expected to have features such as being cheap, stable, inert and easily available [10]. Similarly, adsorption is an effective and low-cost system used in water treatment. It is basically a mass transfer process in which the solid phase in the aqueous solution is transferred to the sorbent surface [12].

Synthetic dyes are harmful chemicals used in a variety of applications such as paper, food, leather and pharmaceuticals. They can also be released uncontrolled as industrial waste. They have serious damage to the ecosystem [13]. Methylene blue (MB) is a cationic and blue colored dye known as methylthioninium chloride [14, 15]. It is generally used in the textile industry and other areas for dyeing purposes. MB, which has toxic properties, is carcinogenic, not biodegradable and has an aromatic ring structure. It is a harmful compound that can affect human health at many points [15, 16].

In this study, sodium bentonite was used as a silica precursor raw material to synthesize SiO_2 NPs. SiO_2 NPs was prepared by treating with NaOH and HCl. The chemical structure and morphological properties of the obtained nanoparticles were examined by Fourier Transmittance Infrared (FTIR), Energy dispersive X-ray (EDX) and Scanning Electron microscopy (SEM) analyses. SiO_2 NPs synthesized for use in water treatment were used in photodegradation and adsorption processes. For this purpose, cationic MB dye was selected as the model dye compound.

2. Material and Methods

2.1. Materials

Sodium bentonite, which was used as raw material to prepare NPs, was purchased from Carben. Sodium hydroxide pellets were supplied from Honeywell Fluka, hydrochloric acid (HCl,

37%) solution was supplied from Merck, MB was supplied from Isolab firm, and hydrogen peroxide (H_2O_2, %30) was supplied from Tekkim company.

2.2. Preparation of SiO_2 NPs

Sodium bentonite clay was used as a silica precursor in this study. The method used in our study was modified from those applied to fly ash and sodium bentonite in the literature [8, 17]. In the literature, the synthesis of sodium silicate by treating the raw material with NaOH and then treating sodium silicate with acid to obtain SiO_2 is also known as the sol-gel method [18]. 1 g of sodium bentonite was mixed with 8 M NaOH at 90 ⁰C for 90 min. After the mixture cooled, it was filtered with filter paper. 5 M HCl solution was added dropwise to the filtrate. This process was continued until a thin gel layer was formed and the pH was determined as 9.6 at this time. The temperature at this time was 30 ⁰C. The addition of HCl was stopped when the gel was formed. It was covered and left to age for 24 h. The next day, the suspension was filtered with filter paper and dried in an oven at 40 ⁰C for 24 h.

2.3. Photocatalytic activity

For photocatalytic degradation experiments, 50 ml of 10 mg/L MB solution was added to a 100 mL volumetric flask and a certain amount of synthesized photocatalyst was added to the solution and the mixture was stirred on a magnetic stirrer. Then, H_2O_2 was added to the suspension to provide oxidation and mixed. Before irradiation, it was stirred in the dark for 30 minutes to reach an adsorption/desorption equilibrium between the MB molecule and the catalyst. Then, the UV lamp (366 nm, UVA) lights were turned on and the solution was irradiated with UV light for 60 minutes, and during this time, samples were taken from the suspension every 15 minutes and absorbance was measured on a UV/vis spectrophotometer. The wavelength at which MB gives maximum absorbance is 664 nm. The equation for calculating the $\% \, degradation$ is given in Equation 1.

$$Degradation \, (\%) = (Co - C)/Co \times 100 \qquad (1)$$

C_o is the initial dye concentration (t = 0) and C is the dye concentration after irradiation for the selected time point.

Various kinetic models have been proposed in the literature to understand the degradation mechanism of azo dyes over time. The most commonly used models include first and second order kinetic models [19]. Photocatalytic degradation reactions are planned to be explained by first order reaction kinetics (Equation 2) and second order reaction kinetics (Equation 3). Here k_1 v k_2 are the first and second order reaction kinetic constants, respectively. C_o is the concentration at the initial time and C_t is the concentration at time t. The unit of concentrations is mg/L. Time is indicated by t (min) [20, 21].

$$ln\ (C_t\ /C_o) = -k_1 t \qquad (2)$$

$$1/C - 1/C_o = k_2 t \qquad (3)$$

2.4. Adsorption process

The usability of SiO$_2$ NPs as an adsorbent was tested in the removal of MB solution from an aqueous solution. The initial dye concentration was determined as 10 mg/L and the aqueous solution volume (V, mL)) as 100 mL. Adsorbent (m, g) was added to the dye solution at its own pH and the mixture was provided. In order to examine the effect of the contact time, absorbance values of samples taken from the mixture at certain time intervals were determined in UV/vis spectroscopy at 664 nm. *Adsorption* (%) and adsorption capacity (q_t) are given in Equations 4 and 5. Here m is known as the amount of adsorbent (g). The unit of adsorption capacity is also mg/g. Pseudo-second-order kinetic model (PSO) is presented in Equation 6. Here q_e (mg/g) is the equilibrium absorption capacity and k_2 is the model constant [22].

$$\%Adsorption = \frac{Co-C}{Co} x100 \qquad (4)$$

$$q_t = \frac{(C_o-C_t).V}{m} \qquad (5)$$

$$\frac{t}{qt} = \frac{1}{k_2.qe^2} + \frac{1}{qe}t \qquad (6)$$

2.5. Characterization

The chemical structure of the SiO$_2$ NPs was investigated by Attenuated Total Reflection-Fourier Transform Infrared (ATR-FTIR, Bruker, Tensor II) spectroscopy in the wavelength range of 4000-400 cm^{-1}. Scanning electron microscope (SEM-EDX, Tescan Mira 3 XMU) was used to analyze the NPs formation in terms of size and shape. The elemental content of the structure was determined by Energy dispersive X-ray (EDX).

3. Results and Discussion

3.1. FTIR

The chemical structure of the synthesized SiO$_2$ NPs was analyzed by FTIR spectroscopy and is presented in Figure 1. The peaks on the spectrum represent the chemical structure of the SiO$_2$ NPs structure. The band appearing at 3395 cm^{-1} can be attributed to the stretching caused by the binding of water molecules and silanols [2]. This peak additionally represents the asymmetric stretching vibration of the Si-O-Si bond, indicating the formation of silica NPs [23]. The peak at 1641 cm^{-1} can be attributed to O-H bonding from water, the large peak at 1059 cm^{-1} to Si-O stretching, and the peak at 801 cm^{-1} to Si-O-Si symmetric stretching [24]. It has been reported that the region between 400 and 1200 cm^{-1} is the region representing silica. The peaks occurring at 440.97 cm^{-1} can be attributed to the vibration band of Si-O-Si and the peak at 708 cm^{-1} can be attributed to the symmetric stretching vibration of Si-O-Si [17]. The peaks of the nanoparticle are in agreement with the literature and demonstrate the successful synthesis of SiO$_2$ NPs.

3.2. SEM

The morphological structure of SiO$_2$ NPs was examined with SEM images shown in Figure 2. The particles show a structure similar to a

spherical form in different sizes in the range of 50-110 nm. It can be said that the nanoparticles
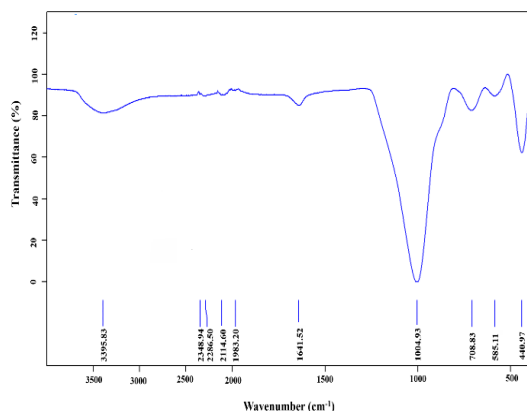
Figure 1. FTIR spectrum of SiO_2 NPs

are agglomerates [5]. According to the literature, these NPs with spherical shape, which are agglomerated, have a significant surface-to-volume ratio and active sites. These active sites increase the absorption of UV light and enable them to be a good photocatalyst [2].

The EDX data graph of SiO_2 NPs is given in Figure 3. The elemental structure of the nanoparticle is understood by weight and atomically. When the percentages are examined here, it is remarkable that there is more than twice the oxygen of silicon. This oxygen may also be excess oxygen coming from sodium bentonite or NaOH that does not react. However, the oxygen element is still at least twice the weight and atomic weight of the silicon element. In this case, it is thought that the synthesized nanoparticle may be SiO_2.

From the results, it is seen that there are elements such as Na, Cl, Al and C. It is thought that the reason for this is the impurities in the raw materials and the HCl, NaOH solutions used [23].

The possible reaction mechanism in SiO_2 NPs synthesis is given below [17, 25, 26]. Here, firstly (Equation 7) it can be assumed that silicates from sodium bentonite react with NaOH to form Na_2SiO_3. In Equation 8, silicic acid, which is the product of the HCl treatment process, appeared when the pH was 9.6 and the

temperature was 30 ⁰C. According to the literature, this reaction is the basis of the sol-gel method. In Equation 9, it is seen that silicic acid can transform into Si-O-Si and silicon hydroxide species [17, 27].

$$SiO_2 + 2NaOH \rightarrow Na_2SiO_3 + H_2O \qquad (7)$$

$$Na_2SiO_3 + H_2O + HCl \rightarrow Si(OH)_4 \text{ (nano silica)} + H_2O + 2NaCl \qquad (8)$$

$$Si\text{-}OH + Si\text{-}OH \leftrightarrow \text{-}Si + H_2O \qquad (9)$$
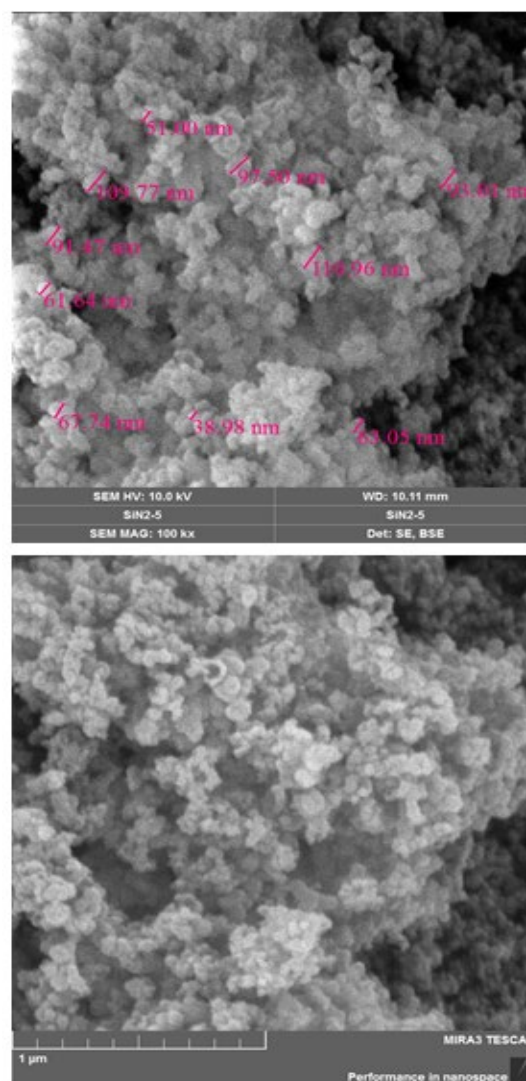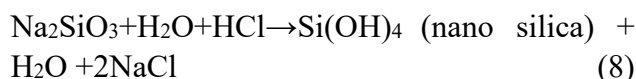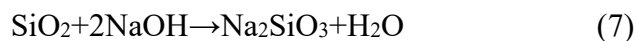
Figure 2. SEM images of SiO_2 NPs
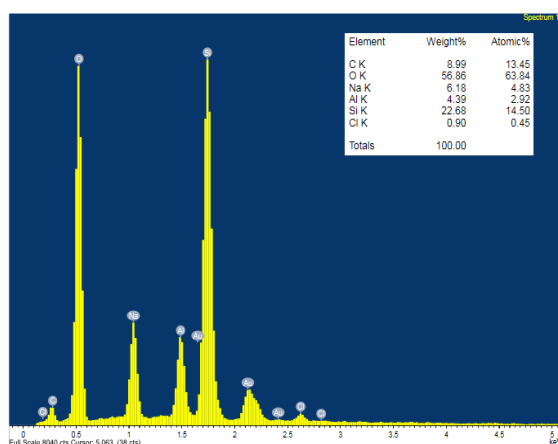
Figure 3. EDX data of SiO$_2$ NPs

3.3. Photocatalytic degradation

A calibration graph was obtained by plotting the MB solution prepared at different concentrations (0.1-12 mg/L) and the absorbance measurements read in UV/vis spectroscopy at 664 nm. The equation (y=0.1722x+0.1867) obtained from this graph was used to convert the absorbance values to MB concentration values.

The degradation process of MB dye using UV lamp was investigated against time using SiO$_2$ NPs. The reason for using H$_2$O$_2$ in the photodegradation process is to increase efficiency [4].

The amount of photocatalyst and the volume ratio of the dye solution were kept constant as 1 mg/mL. In Figure 4, the UV spectrum of the MB solution at t0 and t60 after the degradation process started is given. Thus, the effectiveness of SiO$_2$ NPs as a photocatalyst is revealed after 60 minutes. It is seen that the solution shows maximum absorbance at 664 nm as expected and the absorbance peak intensity decreases at the end of 60 min. It was determined that the dye underwent 80% degradation at the end of 60 min in the presence of SiO$_2$ NPs photocatalyst. According to the literature, photocatalyst properties may increase due to electron-hole pairs that may form on the surface of nanoparticles. This may be caused by oxygen defects in the SiO$_2$ NPs structure [2].
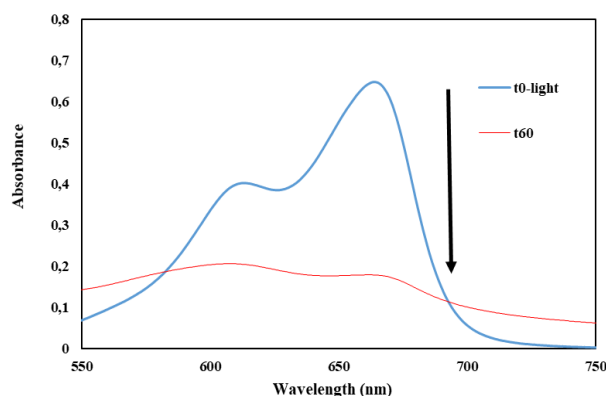
Figure 4. UV spectra of MB at time t0 and time t60

Figures 5 and 6 show the graphs of the first and second order kinetic models. For this purpose, samples were taken from the dye solution at 0, 15, 30, 45 and 60 min for 60 min and their concentrations were calculated. It is seen that the degradation process is compatible with the second order kinetic model. The kinetic model constants k$_1$ were determined as 0.0379 min^{-1} and k$_2$ as 0.306 L/mg.min.
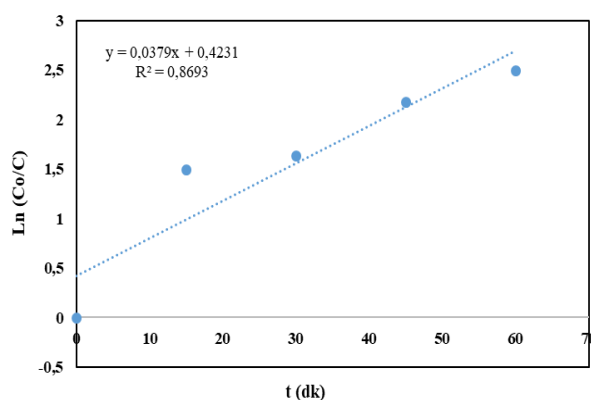
Figure 5. Graph of first order reaction kinetic model
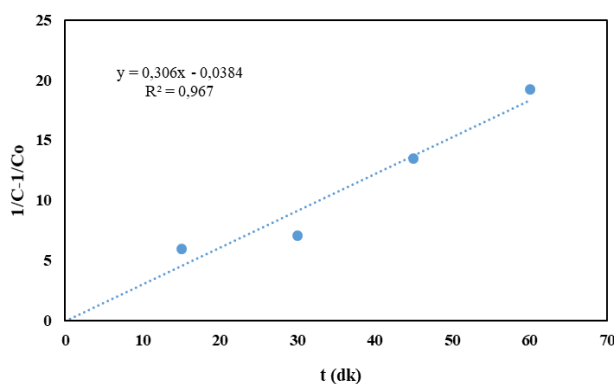
Figure 6. Graph of second order reaction kinetic model

It is well known that crystalline silica has a significant band gap. Therefore, it is difficult to

photoexcite in various UVA, UVB and visible radiation regions. However, structural defects facilitate photoexcitation [28].

Figure 7 shows the degradation rate of MB against time. According to this data, the degradation of MB occurred rapidly after the first 15 minutes. Then, it is seen that the degradation rate slowed down. This result shows that SiO_2 NPs synthesized from sodium bentonite can be used as a good photocatalyst and affects the degradation process in a short time. Among these, SiO_2 NPs is thought to be a photocatalyst that can accelerate photocatalytic degradation and can be easily synthesized. Table 1 shows the comparison of SiO_2 NPs as a photocatalyst with the literature. When Table 1 is examined, it is seen that different dyes or drugs and different working times are used. In addition, the UV lamps and systems used differ. This affects the degradation efficiency. In the light of all these data, it can be said that the SiO_2 we used in our study is a good photocatalyst despite the process not being optimized and reaches a high degradation efficiency in a short time.
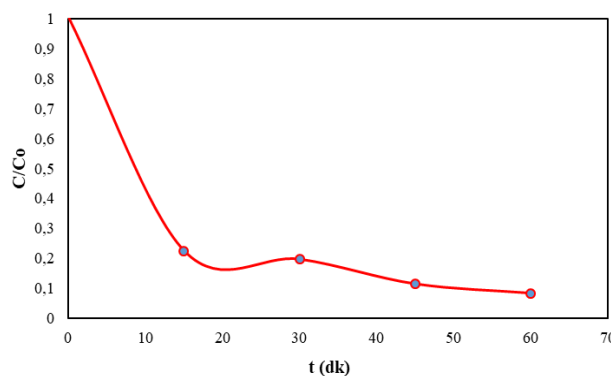
Figure 7. Degradation (%) graph

Table 1. Photocatalysts used in literature and process information

Photocatalyst	Sorbate	Time (min)	Degradation (%)	References
SiO_2-TiO_2	MB	30	85	[29]
Ag/Silica nanocomposite	Ciprofloxacin	180	98	[10]
SiO_2 NPs	Methyl orange	90	95	[2]
SiO_2 NPs	MB	90	98	[2]
SiO_2 NPs	MB	60	80	This study

3.4. Adsorption process

MB from an aqueous solution was removed by SiO_2 NPs synthesized from sodium silicate during the course of 60 minutes of contact time. The effect of contact time on adsorption (%) and adsorption capacity (q_t) is presented in Figure 8. It is seen that the dye adsorbed very quickly onto the adsorbent in the first 15 min. Afterwards, there was no significant change in adsorption and adsorption capacity. At the end of the adsorption process, 90% dye removal and 9.68 mg/g adsorption capacity were achieved.
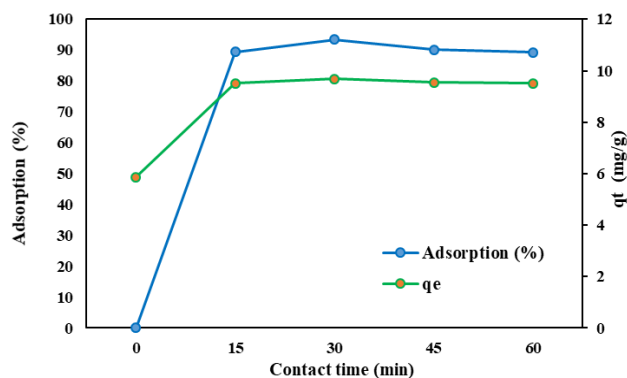
Figure 8. Effect of contact time on adsorption and q_t

When the PSO kinetic model graph given in Figure 9 is examined, it can be said that the MB adsorption of SiO_2 NPs follows the PSO model because the regression (R^2=0.9999) value is almost close to 1. The PSO kinetic model suggests that there is a chemical bond between the dye and sorbent molecules and relates this to the adsorption capacity [11]. In this case, it can be said that there is a chemical reaction between

SiO_2 NPs and MB molecules. It can be said that SiO_2 NPs synthesized from sodium bentonite are not only an effective photocatalyst but also an efficient adsorbent. SiO_2 and nanomaterials prepared with SiO_2 used in various dyes in the literature and their process results are given in Table 2. It is noteworthy that SiO_2 NPs removes the dye from the aqueous solution in a short time. The effectiveness of SiO_2 NPs in the photocatalytic degradation and adsorption parts of the study is promising to achieve good results without optimizing the process.
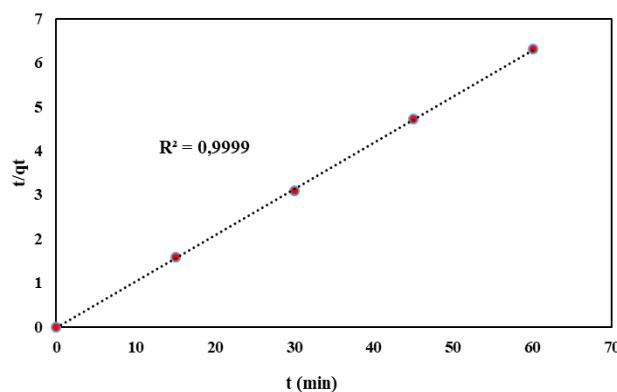
Figure 9. Graph of PSO kinetic model

Table 2. Adsorbents used in literature and process information

Sorbent	Sorbate	Adsorption (%)	Contact time (min)	References
SiO_2 NPs	MB	95.1	180	[27]
SiO_2-TiO_2	MB	88.6	30	[29]
SiO_2	Safranin O	96	60	[30]
SiO_2	Methyl orange	73	80	[30]
SiO_2NP	MB	90	60	This study

4. Conclusion

In this study, it was aimed to prepare SiO_2 NPs by processing sodium bentonite clay with chemical method. According to FTIR, SEM and EDX analysis, spherical nanoparticles in the range of 50-100 nm were obtained. It was revealed that 80% photodegradation was achieved when SiO_2 NPs were used as photocatalysts and 90% dye removal was achieved when used as adsorbents. These results were obtained for a contact time of 60 min and for MB dye for both processes. It was determined that the degradation process was compatible with second order reaction kinetics. It is thought that there is an interaction between the chemical dye and SiO_2 NPs because the adsorption process follows PSO. The study is aimed to be used in the future in process optimization in the removal of pollutants from aqueous solutions or in application areas such as drug delivery and therapeutic effect.

Article Information Form

The Declaration of Conflict of Interest
No conflict of interest or common interest has been declared by authors.

Authors' Contribution
Conceptualization, N.K; methodology, N.K. and A.K; validation, N.K.; investigation, N.K. and A.K.; data curation, N.K.; writing—original draft preparation, N.K.; writing—review and editing, N.K.; visualization, N.K.; supervision, N.K.; project administration, A.K and N.K. All authors have read and agreed to the published version of the manuscript.

Artificial Intelligence Statement
No artificial intelligence tools were used while writing this article.

References

[1] K. A. Altammar, "A review on nanoparticles: Characteristics, synthesis, applications, and challenges," Frontier in Microbiology. vol. 14, 1155622, 2023.

[2] A. I. Biradar, P.D. Sarvalkar, S. B. Teli, C. A. Pawar, P. S. Patil, N. R. Prasad, "Photocatalytic degradation of dyes using one-step synthesized silica nanoparticles," Materials Today: Proceedings. vol. 43, pp. 2832–2838, 2021.

[3] T. I. Janjua, Y. Cao, F. Kleitz, M. Linden, C. Yu, A. Popat, "Silica nanoparticles: A review of their safety and current strategies to overcome biological barriers," Advanced Drug Delivery Reviews. vol. 203, 115115, 2023.

[4] N. Kütük, S. Çetinkaya, "Green synthesis of copper oxide nanoparticles using black , green and tarragon tea and investigation of their photocatalytic activity for methylene blue," Pamukkale University Journal of Engineering Sciences. vol. 28, no. 7, pp. 954–962, 2022.

[5] J. Hwang, J. H. Lee, J. Chun, "Facile approach for the synthesis of spherical mesoporous silica nanoparticles from sodium silicate," Materials Letters. vol. 283, pp. 1–4, 2021.

[6] Y. Huang, P. Li, R. Zhao, L. Zhao, J. Liu, S. Peng, X. Fu, X. Wang, R. Luo, R. Wang, Z. Zhang, "Silica nanoparticles: Biomedical applications and toxicity," Biomedicine & Pharmacotherapy. vol. 151, 113053, 2022.

[7] C. C. M. C. Carcouët, M. W. P. Van De Put, B. Mezari, P. C. M. M. Magusin, J. Laven, P. H. H. Bomans, H. Friedrich, A. C. C. Esteves, N. A. J. M. Sommerdijk, R. A. T. M. Van Benthem, G. De With, "Nucleation and growth of monodisperse silica nanoparticles," Nano Letters. vol. 14, no. 3, pp. 1433–1438, 2014.

[8] U. Zulfiqar, T. Subhani, S. W. Husain, "Synthesis and characterization of silica nanoparticles from clay," Journal of Asian Ceramic Societies. vol. 4, no. 1, pp. 91–96, 2016.

[9] N. Muhammad, S. Siddiqua, "Calcium bentonite vs sodium bentonite: The potential of calcium bentonite for soil foundation," Materials Today: Proceedings. vol. 48, pp. 822–827, 2022.

[10] M. Golmohammadi, H. Hanafi-Bojd, M. Shiva, "Photocatalytic degradation of ciprofloxacin antibiotic in water by biosynthesized silica supported silver nanoparticles," Ceramics International. vol. 49, no. 5, pp. 7717–7726, 2023.

[11] A. Kul, Rıza, H. Koyuncu, A. Turan, A. Aldemir, "Comparative Research of Isotherm, Kinetic, and Thermodynamic Studies for Neutral Red Adsorption by Activated Carbon Prepared from Apple Peel," Water, Air, & Soil Pollution. vol. 234, no. 6, pp. 1–26, 2023.

[12] R. Rashid, I. Shafiq, P. Akhter, M. J. Iqbal, M. Hussain, "A state-of-the-art review on wastewater treatment techniques: The effectiveness of adsorption method," Environmental Science and Pollution Research. vol. 28, no. 2021, pp. 9050–9066, 2021.

[13] I. Din, Muhammad, R. Khalid, J. Najeeb, Z. Hussain, "Fundamentals and photocatalysis of methylene blue dye using various nanocatalytic assemblies- a critical review," Journal of Cleaner Production. vol. 298, 126567, 2021.

[14] T. Cwalinski, W. Polom, L. Marano, G. Roviello, A. D. Angelo, N. Cwalina, M. Matuszewski, F. Roviello, J. Jaskiewicz, K. Polom, "Methylene Blue — Current Knowledge, Fluorescent Properties, and Its Future Use," Journal of Clinical Medicine. vol. 9, no. 11, 3538, 2020.

[15] O. P. Oladoye, T. Ajiboye, Oladiran, E. Omotola, Oyinkansola, J. Oyewola, Olusola, "Methylene blue dye: Toxicity and potential elimination technology from wastewater," Results in Engineering. vol. 16, 100678, 2022.

[16] W. A. Hammad, M. A. Darweesh, N. Zouli, S. M. Osman, B. Eweida, M. H. A. Amr, "Adsorption of cationic dye onto Raphanus seeds: Optimization, adsorption kinetics, thermodynamic studies," Scientific Reports. vol. 14, 17827, 2024.

[17] V. K. Yadav, M. H. Fulekar, "Green synthesis and characterization of amorphous silica nanoparticles from fly ash," Materials Today: Proceedings. vol. 18, pp. 4351–4359, 2019.

[18] P. Sharma, J. Prakash, R. Kaushal, "An insight into the green synthesis of SiO_2 nanostructures as a novel adsorbent for removal of toxic water pollutants," Environmental Research. vol. 212, 113328, 2022.

[19] A. Mohagheghian, R. Ghaneei-Motlagh, K. Ayagh, M. Shirzad-Siboni, "Visible-light photocatalytic degradation of two textile dyes by recyclable ZnO-Perlite: Kinetic models and cost analysis," International Journal of Environmental Analytical Chemistry. vol. 105, no. 5, pp. 1185–1207, 2025.

[20] J. Zhang, Z. Lin, Z. Yu, Y. Zhang, D. Liang, Y. Chen, Y. Chen, P. Chen, H. Liu, W. Lv, G. Liu, "Simplified synthesis of direct Z-scheme Bi_2WO_6/PhC_2Cu heterojunction that shows enhanced photocatalytic degradation of 2,4,6-TCP: Kinetic study and mechanistic insights," Journal of Hazardous Materials. vol. 459, 132065, 2023.

[21] A. Balakrishnan, K. Gopalram, S. Appunni, "Photocatalytic degradation of 2,4-dicholorophenoxyacetic acid by TiO_2 modified catalyst: Kinetics and operating cost analysis," Environmental Science and Pollution Research. vol. 28, no. 25, pp. 33331–33343, 2021.

[22] S. Sadaf, H. N. Bhatti, "Batch and fixed bed column studies for the removal of Indosol Yellow BG dye by peanut husk," Journal of the Taiwan Institute of Chemical Engineers. vol. 45, no. 2, pp. 541–553, 2014.

[23] J. Marousek, A. Marouskov, R. Periakaruppan, G. M. Gokul, A. Anbukumaran, A. Bohata, P. Kriz, J. Barta, P. Cerny, P. Olsan, "Silica nanoparticles from coir pith synthesized by acidic sol-gel method improve germination economics," Polymers. vol. 14, no. 2, 2022.

[24] M. Rafigh, Sayyid, A. Heydarinasab, "Mesoporous Chitosan − SiO_2 Nanoparticles: Synthesis, Characterization, and CO_2 Adsorption Capacity," ACS Sustainable Chemistry and Engineering. vol. 5, pp. 10379–10386, 2017.

[25] F. da S. Bruckmann, A. C. Pimentel, A. R. Viana, T. da R. Salles, L. M. F. Krause, S. R. Mortari, I. Z. da Silva, C. R. B. Rhoden, "Synthesis, characterization and cytotoxicity evaluation of magnetic nanosilica in L929 cell line," Disciplinarum Scientia - Ciências Naturais e Tecnológicas. vol. 21, no. 3, pp. 01–14, 2020.

[26] P. Sharma, J. Kherb, J. Prakash, R. Kaushal, "A novel and facile green synthesis of - SiO_2 nanoparticles for removal of toxic water pollutants," Applied Nanoscience. vol. 13, no. 1, pp. 735–747, 2023.

[27] A. Samy, A. M. Ismail, H. Ali, "Environmentally friendly mesoporous SiO_2 with mixed fiber / particle morphology and large surface area for enhanced dye adsorption," Journal of Materials Science. vol. 58, no. 4, pp. 1586–1607, 2023.

[28] G. Romolini, M. G. D. Ricciarelli, L. T. G. Zampini, "Photocatalytic activity of silica and silica - silver nanocolloids based on photo - induced formation of reactive

oxygen species," Photochemical & Photobiological Sciences. vol. 20, no. 9, pp. 1161–1172, 2021.

[29] U. Mahanta, M. Khandelwal, A. S. Deshpande, "TiO_2 @ SiO_2 nanoparticles for methylene blue removal and photocatalytic degradation under natural sunlight and low-power UV light," Applied Surface Science. vol. 576, no. PA, pp. 151745, 2022.

[30] S. S. Batool, Z. Imran, K. Rasool, M. Ahmad, M.A. Rafiq, "Enhanced adsorptive removal of toxic dyes using SiO_2 nano fibers," Solid State Sciences. vol. 55, pp. 13–20, 2016.

The Use of Synthesized Zinc Oxysulphide Nanoparticles in Phosphate Phosphorus Removal from Synthetic Wastewater and Statistical Analysis

Nilüfer Ülgüdür [iD]

Düzce University, Faculty of Engineering, Department of Environmental Engineering, Düzce, Türkiye, niluferulgudur@duzce.edu.tr, ror.org/04175wc52

ARTICLE INFO	ABSTRACT
	This study investigated the phosphate phosphorus (PO_4-P) removal potential of zinc oxysulfide (ZnO_xS_y) nanoparticles obtained by fifteen varying component ratios. The statistical meaning of the distinct synthesis compositions was evaluated by regression analysis based on the response of PO_4-P removal efficiencies. The results indicated that ZnO_xS_y nanoparticles could remove PO_4-P by 99.5% without optimization of the adsorption process (Initial PO_4-P concentration: 15 mg/L, adsorbent dose: 1 g/L, pH: 4.31, contact time: 2 hr). However, the synthesis compositions of ZnO_xS_y nanoparticles strongly effect the PO_4-P removal efficiency. The data could be interpreted by regression analysis with a high R^2 of 89.61% and p value of 0.000. The main component that positively affect the PO_4-P removal efficiency was hydrogen peroxide, whereas sodium sulfide component had a limited effect.

1. Introduction

Phosphorus is a nutrient for living things. However, it can be regarded as a pollutant when severe consequences of its prevalence in water bodies such as eutrophication is considered. Therefore, phosphorus pollution in water bodies should be controlled by eliminating the discharges of or treating phosphorus containing wastes and wastewaters [1, 2]. The oxidation states of phosphorus are +II, +III, +IV, and +V and the coordination numbers range from one to six [3]. The removal of phosphorus from water should have supposedly been simple depending on the positive charge related to the oxidation state of the phosphorus. Since the positively charged pollutants can be removed by conventional adsorbents such as zeolites and clay due to their opposite (negative) surface charges [4].

However, phosphorus forms oxyanions in water (i.e. dihydrogen phosphate- $H_2PO_4^-$, hydrogen phosphate -HPO_4^{2-} and phosphate- PO_4^{3-}), which can convert positively charged phosphorus element into negatively charged compounds by attracting oxygen elements in water depending on the pH value [5]. Thus, the removal of phosphorus from aqueous solutions become challenging.

Several methods have been offered for phosphorus removal from aqueous environment such as physico-chemical, biological and/or combinations [6, 7]. However, these methods have several limitations that can be regarded as the lack of cost-effectiveness and high removal efficiencies, the generation of toxic products or wastes which requires to be further handling [7]. Adsorption processes have been considered as a widely applicable pollutant removal process based on the high removal efficiencies, cost-effectiveness and easy application [8-10]. Nanoparticles and the derivative composites are emerging adsorbents for phosphorus removal due to their reactivities, selectivity and high surface areas [11,12].

Lanthanum-zirconium binary metal oxide nanoparticles [10] and ceria-loaded biochar [12] are among the emerging adsorbents produced with the aim of phosphate phosphorus (PO4-P) removal. These adsorbents offer high removal efficiencies, selectivity for PO4-P and fast removal kinetics [11, 12]. However, the use of rare earth metals such as lanthanum and ceria, can increase the overall cost of the process due to their lower abundance and relatively high costs [13].

Relatively economical alternatives of the nanoparticles can also be used as PO4-P adsorbents. Nanoscale zero valent iron (nZVI) has been widely used adsorbents in water treatment due to its reaction and reduction potential with most of the pollutants in aqueous environment. nZVI dose of 1 g/L can remove 76.8 mg PO4-P when the initial concentration is 100 mg/L [14], while silica nanoparticles obtained from rice husk ash had PO4 adsorption capacity of 9.08 mg/g [15]. Iron-manganese oxide spinel with $MnFe_2O_4$ structure exhibited PO4-P adsorption efficiency of 98.52% (adsorbent dosage: 2.5 g/L, PO4-P concentration: 10 ppm) [16].

These studies apparently demonstrate the efficiency of nanoparticles in PO4-P removal from aqueous environment. However, the variability in synthesis conditions of nanoparticles can considerably affect the key features of the adsorbents such as particle size, shape and functional groups [17-19]. Therefore, the synthesis conditions should be optimized depending on the target pollutant to identify the critical components in the synthesis to reach an efficient treatment process.

Zinc (Zn) is one of the abundant, low-cost and environmentally friendly material [20], which can be used in adsorbent synthesis. Furthermore, Zn can improve the selectivity in adsorption processes for enhancing PO4-P removal [21, 22]. To date, Zn has been incorporated into nanoparticles and their composites such as in the form of CaZnFeZr; MgFeZr and MgZnFe [21]. On the other hand, zinc oxysulfide (ZnO_xS_y) nanoparticles have been synthesized and used for the removal of another oxyanion, i.e. arsenic, from aqueous solutions [23]. However, there is

no study investigated PO4-P removal using ZnO_xS_y nanoparticles.

This study aims at identification of the optimum chemical synthesis conditions of ZnO_xS_y nanoparticles for the removal of PO4-P from aqueous environment. To this purpose, ZnO_xS_y nanoparticles were synthesized under varying compositions of the chemical components. Batch PO4-P adsorption tests were performed for each synthesis. The results were evaluated by fitting a regression model to reach an efficient PO4-P adsorbent.

1. General Methods

1.1. Synthesis of zinc oxysulfide particles

ZnO_xS_y particles were synthesized according to the method proposed by Uppal et al [23]. Briefly, zinc chloride ($ZnCl_2$) was dissolved in deionized water. Concentrated ammonium hydroxide solution (NH_4OH, 25%, will be denoted as NH_4) was added to the solution. Sodium sulfide nonahydrate ($Na_2S.9H_2O$, will be denoted as Na_2S) and hydrogen peroxide (H_2O_2, 30%) were added to the solution, respectively. The process for the formation of ZnO_xS_y was carried out under continuous stirring and at approximately 90°C. The formed precipitate was filtered and washed thoroughly with deionized water. ZnO_xS_y nanoparticles were then dried in the oven at 65°C overnight. Fifteen forms of ZnO_xS_y nanoparticles with varying components were synthesized and used in the study.

1.2. Batch adsorption tests

Synthetic phosphate solution was prepared by dissolving potassium dihydrogen phosphate (KH_2PO_4) in deionized water. The initial concentration of PO4-P was set to 15 mg/L. The initial pH of the solution was 4.31. The adsorbent dose was 1 g/L. The batch adsorption experiment was performed for each adsorbent in a rotary mixer at 70 rpm using 50 mL centrifuge tubes. The solution was immediately filtered from 0.22 μm pore-sized nylon syringe filters.

PO4-P was measured spectrophotometrically by ascorbic acid method according to the Standard methods [24]. The following formula was used to

calculate the removal of the adsorption process [25]:

$$R(\%) = \frac{(C_o - C_e)}{C_o} x100 \qquad (1)$$

where C_o and C_e represent the initial and final concentrations of PO$_4$-P in the solution (mg/L) and R represents the PO$_4$-P removal efficiency.

1.3. Regression model analysis

Minitab Statistical Software 22 was used to identify the optimum regression equation considering the system components. This equation representing the best correlation between the synthesis components and PO$_4$-P removal efficiency had a significant statistical meaning ($p < 0.05$).

3. Results and Discussion

3.1. The synthesis of zinc oxysulfide particles and adsorption tests

The synthesis compositions of components of ZnCl$_2$, NH$_4$, Na$_2$S and H$_2$O$_2$ are given in Table 1. A white precipitate initially formed as NH$_4$ was added and then disappeared as more NH$_4$ was added. NH$_4$ of 0.5 mL was the initial point for the precipitate formation, whereas 3 mL represented the initial stage for precipitate disappearance. The amount of Na$_2$S were determined based on the weight ratios of 1:0.5 (Zn-1, Zn-2, Zn-4, Zn-11, Zn-13), 1:1 (Zn-3, Zn-5, Zn-6, Zn-12, Zn-14) and 1:5.25 (Zn-7, Zn-8, Zn-9, Zn-10, Zn-15). H$_2$O$_2$ was added in 0, 2 and 10 mL in different synthesis.

The PO$_4$-P removal efficiencies ranged approximately from 4.0% to 99.5% using fifteen individual syntheses (Table 1). This change indicated that the variances in synthesis conditions had significant effect on the removal efficiency of the target pollutant from aqueous solutions [17]. The adsorption test was conducted to compare the PO$_4$-P removal efficiency of ZnO$_x$S$_y$ nanoparticles without any optimization of batch adsorption tests. Indeed, the high removal efficiency using Zn-2 nanoparticles (removal: 99.5%, initial PO$_4$-P concentration: 15 mg/L, adsorbent dose: 1 g/L, pH: 4.31, contact time: 2 hr) revealed that ZnO$_x$S$_y$ had significant PO$_4$-P removal efficiency from aqueous environment. The lowest PO$_4$-P removal efficiency was observed using Zn-7 nanoparticles under the same operating conditions.

3.2. Evaluation of the regression model

Minitab Statistical Software 22 was used to obtain best applicable regression model. This method is particularly useful to define the relationship between one **dependent parameter** (removal efficiency) and one or more **independent parameter** (predictors) [26]. The independent parameters were determined as NH$_4$, Na$_2$S and H$_2$O$_2$. The order of interactions and terms were adjusted in model, which enable the model to be flexible enough to capture complex, non-linear, and interactive effects of NH$_4$, Na$_2$S and H$_2$O$_2$ on removal efficiency. The two-sided confidence interval (higher and lower) around the estimated value indicated that the true value would fall within this range with 95% probability. The 95% level of confidence is generally acceptable in most scientific and industrial applications. Each parameter was evaluated by Type III sum of squares to show the contribution of each parameter while accounting for all others [27].

Several regression models were obtained until the regression equation had a statistical meaning, which was regarded as a p value below 0.05 [28]. The statistically acceptable regression model equation (with a p value of 0.000) represented the mathematical relationship between the predictors of NH$_4$, Na$_2$S and H$_2$O$_2$ and the response parameter (PO$_4$-P removal efficiency) according to analysis of variance (ANOVA) analysis. The regression model is presented in Equation 2.

$$R = 56.1\ NH_4 - 1.05\ Na_2S + 5.34\ H_2O_2 \qquad (2)$$
$$- 20.8\ NH_4^2 + 1.093\ NH_4^3$$

where NH$_4$ in mL, Na$_2$S in g and H$_2$O$_2$ in mL, R in %.

Table 1. The components used in the synthesis of ZnO_xS_y nanoparticles and the adsorbent codes

Adsorbent	$ZnCl_2$, g	NH_4, mL	Na_2S, g	H_2O_2, mL	PO_4-P removal, %
Zn-1	3 g	0.50	1.50	10.00	90.024
Zn-2	3 g	2.00	1.50	10.00	99.525
Zn-3	3 g	0.50	3.00	10.00	98.575
Zn-4	3 g	3.00	1.50	10.00	40.380
Zn-5	3 g	2.00	3.00	10.00	80.523
Zn-6	3 g	3.00	3.00	10.00	59.857
Zn-7	3 g	2.00	15.75	0.00	4.038
Zn-8	3 g	3.00	15.75	0.00	19.715
Zn-9	3 g	2.00	15.75	2.00	18.290
Zn-10	3 g	3.00	15.75	2.00	13.777
Zn-11	3 g	16.00	1.50	0.00	65.321
Zn-12	3 g	16.00	3.00	0.00	74.347
Zn-13	3 g	16.00	1.50	2.00	12.352
Zn-14	3 g	16.00	3.00	2.00	68.884
Zn-15	3 g	16.00	15.75	10.00	73.159

The regression model presented three different coefficient of determination (R^2) values as R-sq, R-sq(adj), and R-sq(pred) (Table 2). R-sq value was 89.61% which indicated that the model explained 89.61% of the variability in the removal efficiency based on the amounts of NH_4, Na_2S, and H_2O_2 used. This suggested a strong correlation between the model and the input parameters. R-sq(adj) value (84.42%) took the number of predictors in the model into account, to prevent overfitting. R-sq(adj) value indicated that the model had a correlation of 84.42% among the parameters after adjusting the number of input parameters in the model [29].

The high R-sq(adj) value suggested that the model parameters were effective, and the model is not overfitted by including unnecessary predictors. R-sq(pred) was observed to be 71.44%, which was a value to assess the predictive power of the model for the data that was not included in modeling data set. R-sq(pred) is calculated by a formula that eliminates an observation from the data set, estimates the regression equation, and assesses how well the model predicts the eliminated observation [30]. Even though the predictive power was lower than R-sq, the values of R-sq and R-sq(pred) were compatible.

The normal probability plot of residuals (errors) indicates whether the residuals are approximately normally distributed or not, which represents one of the key assumptions of linear regression on model fitting to the data. The residuals of the data were mostly on or close to the redline (Figure 1a).

This fact indicated the residuals were almost normally distributed.

Table 2. The regression model fitting parameters

	R-sq		89.61%
Regression model	R-sq(adj)		84.42%
	R-sq(pred)		71.44%
Terms	Coefficient	T-Value	p-Value
NH_4	56.1	1.97	0.077
Na_2S	-1.05	-0.87	0.402
H_2O_2	5.34	3.57	0.005
NH_4^2	-20.8	-1.94	0.081
NH_4^3	1.093	1.94	0.081

Additionally, the histogram of the residuals (Figure 1b) controls whether the residuals fit to the normal distribution. The residuals are not perfectly resembled a normal distribution as indicated also by the normal probability of the plot (Figure 1a). The most negative residual on the normal probability plot suggested the potential presence of an outlier. However, repeated synthesis and batch adsorption tests confirmed that this data point is a valid observation and not an outlier. This indicated that the observed deviation could stem from the inherent variability of the system. Alternatively, it could result from limitations in the model's ability to fully capture all underlying factors influencing the response. The residuals versus fits plot serves for comprehending how randomly residuals are distributed with respect to fitted values. The residuals versus fits plot (Figure 1c) showed a limited random distribution of residuals. This suggests that the predictive capability of the model can be improved through further refinement, such as additional synthesis

experiments or batch adsorption tests to better capture the variability in the system. The random distribution of the residual versus observation order plot (Figure 1d) indicated that there are no time- or order-related biases, and the performance of the model is consistent over the experimental sequences.

3.3. The effect of components used in the synthesis on removal efficiency

Linear NH_4 term had a p-value 0.077. This was slightly higher than the threshold of statistically meaningful data (0.05). It had a large coefficient in the regression model equation (56.1) (Table 2). The p values of the quadratic (NH_4^2) and cubic terms (NH_4^3) of NH_4 (0.081) were also higher than 0.05. These facts suggested that NH_4 could have a significant positive but not a definite impact on the removal efficiency. The positive effect indicates that the larger the amount of NH_4, the more the removal of PO_4-P from the aqueous solution. However, the coefficients of NH_4^2 (-20.8) and NH_4^3 (1.093) revealed that as the volume of NH_4 increased at very high levels, the positive impact on the removal of PO_4-P diminished or even turned to negative.

Na_2S having a p value of 0.402 was statistically insignificant, which reflected Na_2S did not have a considerable effect on the removal efficiency. However, it should be noted that the addition of Na_2S is a compulsory application to form ZnO_xS_y nanoparticles. Therefore, the evaluation of 'statistically insignificant' was based on the range of Na_2S amounts added during the synthesis. Na_2S has a little decreasing effect on removal efficiency, considering the coefficient in the regression equation (-1.05). H_2O_2 component influences the removal efficiency, based on the p value as statistically significant (p: 0.005). The positive coefficient of H_2O_2 in regression analysis (5.34) also indicated the addition of H_2O_2 improves the removal efficiency.
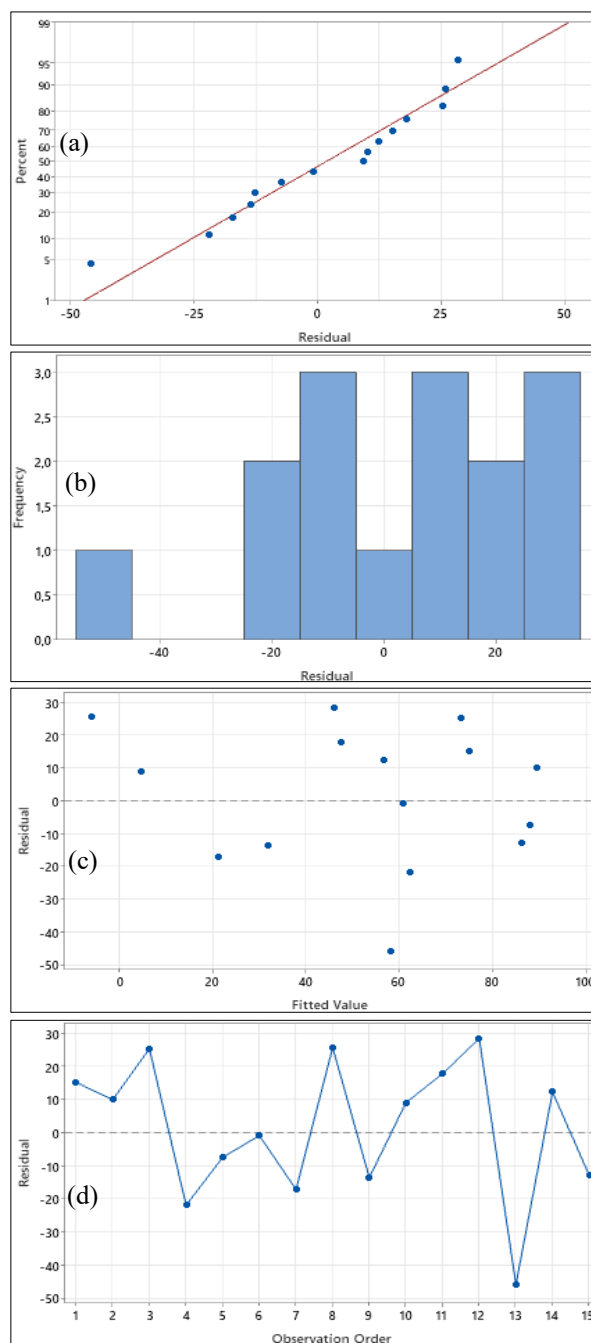
Figure 1. (a) Normal probability plot of residuals, (b) Histogram, (c) Residuals versus fits, (d) Residuals versus observation order

Pareto chart is the graphical representation on which factors have significant effects on the removal of PO_4-P. The related chart (Figure 2) also confirmed the outcomes derived from p values and coefficients of input parameters in regression analysis. H_2O_2 is the powerful component that positively effects the removal efficiency depending on the critical value above 2.228, which is indicated as the redline on Figure 2. The terms of NH_4, NH_4^2 and NH_4^3 can be interpreted as being close to the critical value of 2.228. Thus, NH_4 could be taken as a component

that have effect on the removal efficiency. The effect of Na_2S can be regarded as limited due to the standardized effect below the critical value. However, Na_2S is a compulsory component in the synthesis of ZnO_xS_y particles. Thus, its effect is limited in the concentration range applied during synthesis.
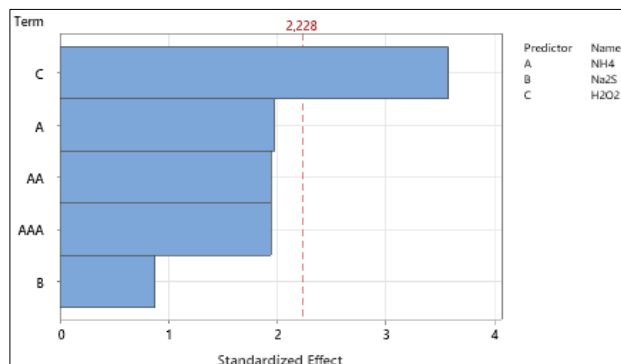
Figure 2. Pareto chart of the standardized effects

4. Conclusion

ZnO_xS_y nanoparticles were synthesized using different proportions of components and PO_4-P removal performance was tested. The PO_4-P removal efficiency was 99.5% when the initial PO_4-P concentration was 15 mg/L, adsorbent dose: 1 g/L, pH: 4.31, within a contact time of 2 hrs. The removal of PO_4-P was modelled by regression analysis with a high R^2 of 89.61% and p value 0.000. The main component that positively affect the removal performance was H_2O_2 by considering the statistical meaning. NH_4 component was close to the borderline of the statistical meaning, which indicated the importance of this component. Even though Na_2S component was found not to have statistically meaning, it should be noted that the model was composed and run in a pre-determined value.

Article Information Form

The Declaration of Conflict of Interest/ Common Interest
No conflict of interest or common interest has been declared by the author.

Artificial Intelligence Statement
No artificial intelligence tools were used while writing this article.

Copyright Statement
The author owns the copyright of their work published in the journal and their work is published under the CC BY-NC 4.0 license.

References

[1]   Y. Ren, W. Zheng, X. Duan, N. Goswami, Y. Liu, "Recent advances in electrochemical removal and recovery of phosphorus from water: A review," Environmental Functional Materials, vol. 1, no. 1, pp. 10–20, 2022.

[2]   C. Korkmaz, G. D. Değermenci N. Değermenci, "Removal of phosphate from aqueous solution using anion exchange resin: Equilibrium, isotherms and kinetics," Fibers and Polymers, vol. 24, pp. 3753–3760, 2023.

[3]   I. Haiduc, "Phosphorus–Nitrogen Compounds," in Encyclopedia of Inorganic and Bioinorganic Chemistry, John Wiley & Sons, Ltd., 2006.

[4]   Z. Li, R. S. Bowman, "Sorption of chromate and PCE by surfactant-modified clay minerals," Environmental Engineering Science, vol. 15, no. 3, 1998.

[5]   U. Kafkafi, "Oxyanion Sorption on Soil Surfaces," in Inorganic Contaminants in the Vadose Zone. Ecological Studies, vol. 74, B. Bar Yosef, N. J. Barrow, and J. Goldshmid, Eds., Springer, Berlin, Heidelberg, 1989.

[6]   J. T. Bunce, E. Ndam, I. D. Ofiteru, A. Moore, D. W. Graham, "A review of phosphorus removal technologies and their applicability to small-scale domestic wastewater treatment systems," Frontiers in Environmental Science, vol. 6, no. 8, 2018.

[7]   J. Suazo Hernández, P. Sepúlveda, L. Cáceres Jensen, J. Castro Rojas, P. Poblete Grant, N. Bolan, M. L. Mora, "nZVI-based nanomaterials used for phosphate removal from aquatic systems," Nanomaterials, vol. 13, 2023.

[8] C. Karaman, Z. Aksu, "Modelling of Remazol Black-B adsorption on chemically modified waste orange peel: pH shifting effect of acidic treatment," Sakarya University Journal of Science, vol. 24, no. 5, pp. 1135–1150, 2020.

[9] İ. Konuk Akça, R. Köklü, "Removal of paracetamol by powdered activated carbon synthesized from orange peels," Sakarya University Journal of Science, vol. 27, no. 1, pp. 168–180, 2023.

[10] F. Akti, "Effect of modifier agents on particle size and surface functional groups of calcined eggshell: Test in adsorption of remazol yellow," Sakarya University Journal of Science, vol. 24, no. 1, pp. 272–280, 2020.

[11] Y. Du, X. Wang, G. Nie, L. Xu, Y. Hu, "Enhanced phosphate removal by using La-Zr binary metal oxide nanoparticles confined in millimeter-sized anion exchanger," Journal of Colloid and Interface Science, vol. 580, pp. 234–244, 2020.

[12] Y. Wang, X. Xie, X. Chen, C. Huang, S. Yang, "Biochar-loaded Ce^{3+}-enriched ultra-fine ceria nanoparticles for phosphate adsorption," Journal of Hazardous Materials, vol. 396, p. 122626, 2020.

[13] Y. Yu, L. Yu, K. Y. Koh, C. Wang, J. P. Chen, "Rare-earth metal based adsorbents for effective removal of arsenic from water: A critical review," Critical Reviews in Environmental Science and Technology, vol. 48, no. 22–24, pp. 1127–1164, 2018.

[14] I. Maamoun, R. Eljamal, O. Falyouna, K. Bensaida, Y. Sugihara, O. Eljamal, "Insights into kinetics, isotherms and thermodynamics of phosphorus sorption onto nanoscale zero-valent iron," Journal of Molecular Liquids, vol. 328, 2021.

[15] T. T. Nguyen, "Effective removal of phosphate from waste water based on silica nanoparticles," Hindawi Journal of Chemistry, vol. 2022, 2022.

[16] W. Brontowiyono, I. Patra, S. A. Hussein, Alimuddin, A. B. Mahdi, S. E. Izzat, D. M. Al Dhalemi, A. K. O. Aldulaim, R. M. R. Parra, L. A. B. Arenas, Y. K. Mustafa, "Phosphate ion removal from synthetic and real wastewater using $MnFe_2O_4$ nanoparticles: A reusable adsorbent," Acta Chimica Slovenica, vol. 69, pp. 681–693, 2022.

[17] S. Rathod, S. Preetam, C. Pandey, S. P. Bera, "Exploring synthesis and applications of green nanoparticles and the role of nanotechnology in wastewater treatment," Biotechnology Reports, vol. 41, p. e00830, 2024.

[18] C. Quintero Quiroz, N. Acevedo, J. Zapata Giraldo, L. E. Botero, J. Quintero, D. Zárate Trivinõ, J. Saldarriaga, V. Z. Pérez, "Optimization of silver nanoparticle synthesis by chemical reduction and evaluation of its antimicrobial and toxic activity," Biomaterials Research, vol. 23, no. 27, 2019.

[19] P. Szczyglewska, A. Feliczak Guzik, I. Nowak, "Nanotechnology–general aspects: A chemical reduction approach to the synthesis of nanoparticles," Molecules, vol. 28, p. 4932, 2023.

[20] W. Nie, H. Cheng, Q. Sun, S. Liang, X. Lu, B. Lu, J. Zhou, "Design strategies toward high-performance Zn metal anode," Small Methods, vol. 8, 2024.

[21] A. Drenkova Tuhtan, M. Sihtmäe, K. Uke, H. Vija, M. Oppmann, J. Prieschl, K. Mandel, A. Kahru, "Synthesis and ecotoxicity screening of reusable, magnetically harvestable metal oxide/hydroxide nanocomposites for safe and sustainable removal and recovery of phosphorus from wastewater," Journal of Cleaner Production, vol. 444, p. 141287, 2024.

[22] M. Schneider, A. Drenkova Tuhtan, W. Szczerba, C. Gellermann, C. Meyer, H. Steinmetz, K. Mandel, G. Sextl, "Nanostructured ZnFeZr oxyhydroxide

precipitate as efficient phosphate adsorber in waste water: understanding the role of different material-building-blocks," Environmental Science: Nano, vol. 4, pp. 180–190, 2017.

[23] H. Uppal, S. Chawla, A. G. Joshi, D. Haranath, N. Vijayan, N. Singh, "Facile chemical synthesis and novel application of zinc oxysulfide nanomaterial for instant and superior adsorption of arsenic from water," Journal of Cleaner Production, vol. 208, pp. 458–469, 2019.

[24] APHA, Standard Methods for the Examination of Water and Wastewater, 23rd ed. American Public Health Association (APHA), 2017.

[25] H. Wang, X. Liang, Y. Liu, T. Li, K. Y. A. Lin, "Recycling spent iron-based disposable-chemical-warmer as adsorbent for As(V) removal from aqueous solution," Resources, Conservation and Recycling, vol. 168, 2021.

[26] S. Prasad, "Regression," in Advanced Statistical Methods, Singapore: Springer Nature Singapore, 2024.

[27] L. R. LaMotte, "A formula for Type III sums of squares," Communications in Statistics- Theory and Methods, vol. 49, no. 13, pp. 3126–3136, 2020.

[28] U. Knief, W. Forstmeier, "Violating the normality assumption may be the lesser of two evils," Behavior Research Methods, vol. 53, pp. 2576–2590, 2021.

[29] L. Jerome, "Multiple linear and non-linear regression in Minitab," MSOR Connections, vol. 9, no. 3, 2009.

[30] K. P. Burnham, D. R. Anderson, "Multimodel inference: Understanding AIC and BIC in model selection," Sociological Methods and Research, vol. 33, no. 2, pp. 261–304, 2004.

Investigation of the Impact of Intersection Designs, Signalization, and Directions of Intersection Arms on Microscopic Networks: The Case of Erzurum Province

Zühal Zirek [iD], Muhammed Ali Çolak* [iD]

Erzincan Binali Yildirim University, Faculty of Engineering and Architecture, Department of Civil Engineering, Erzincan, Türkiye, zuhalzirek@gmail.com, macolak@erzincan.edu.tr, ror.org/02h1e8605
*Corresponding Author

ARTICLE INFO	ABSTRACT
	Transportation has an important connection in many aspects such as economic growth, trade, tourism and social interaction. Today, the demand for transportation services is increasing with the rapid socio-economic development. This increase brings with it various traffic problems. Effective intersection design in preventing congestion, delays and accidents is of great importance in terms of ensuring traffic safety and sustainability. In this study, Gürcükapı Intersection and Taşhan Intersection were remodeled with Aimsun software in order to reduce the density at the intersections in Erzurum province and to meet traffic needs. Signalization was added to the modeled intersections, the directions of the intersection arms were changed and four alternative scenarios were created with these changes using current scenario. A total of five scenarios, including the current scenario and the developed alternatives, were evaluated and compared based on travel time, delay time, waiting time, speed, queuing, instant CO_2, NO_x, PM (Particulate Matter) and VOC (Volatile Organic Compounds) values. As a result of the comparison, the scenario in which the current intersection arm direction and Gürcükapı and Taşhan intersections are modernized and there is no signaling system was determined as the most effective scenario.

1. Introduction

The expansion and alteration of urban areas result in an increase in the human population and intensified economic activities. This situation increases the variety of urban activities while concurrently improving citizens' mobility and transportation needs. The unchecked and rapid proliferation of vehicles has led to inadequate lanes for the surplus cars, prompting the conversion of at-grade intersections into multi-level intersections, and resulting in the transformation of urban roads into ring roads and ultimately into fully controlled access highways [1]. In modern culture, speed has become an essential requirement, and goals have gained importance due to time constraints. In this case, individuals' efforts to achieve safety, comfort, and convenience shape their lifestyles [2].

Intersections are the most conspicuous sites of traffic congestion on highways and promote safe traffic flow when constructed appropriately. Nonetheless, in instances of insufficient design, they pose the possibility of precipitating accidents [3]. Intersection design, a fundamental component of urban planning, encompasses technical analyses to guarantee the safety of road users and promote seamless transit between converging roadways. An effective intersection design must decrease vehicular wait times, alleviate traffic congestion, and ensure a secure environment for pedestrians.

The development, implementation, and optimization of traffic control and management strategies are critical to ensure that intersections operate efficiently over time [4]. This process requires updating the geometric design to

respond to constantly changing needs. However, there are difficulties in determining ideal lane widths. Although wide lanes are advantageous in terms of comfort of use and safety, they are generally not preferred due to reasons such as project costs and narrowing of the surrounding area [5]. This situation requires careful planning and evaluation to ensure balance in intersection design. Estimating emissions about environmental implications is essential for efficient traffic management and intersection design [6].

The design of intersections must consider the geographical, demographic, economic, and social attributes of the region. The distinct dynamics of each region are the paramount factors that influence the efficacy of intersecting configurations [7]. Traffic simulation programs significantly enhance the efficient planning of transportation networks and the reduction of safety issues. These algorithms provide robust instruments for evaluating dynamic transportation issues that cannot be implemented under real-world circumstances [8]. The simulated environment allows for the observation of results minutes, hours, days, and even weeks prior to those obtained from the identical experiment conducted in the real world [9]. In the initial phase of all simulation programs, the problems are defined, and the corresponding solutions are included into the program. The validity-consistency test involves evaluating the correlation between the simulated designs and the current conditions. In the event that the test results are deemed unsuitable, the simulations will be re-executed [10].

When examining studies on traffic, it is evident that various works focus on human behavior [11-12] and [13-15] the geometric and systematic arrangements within traffic networks. A review of the literature reveals various studies related to traffic simulation. Çakıcı and Murat [13] proposed a computational approach to determine the optimal signal timing and phase plan in the design of signalized roundabouts. In their study, they conducted performance analyses based on delay criteria by considering different intersection types and phase plans. The research findings suggest that in scenarios with high left-turn ratios and increased numbers of signal

phases, alternative intersection designs may be more suitable than signalized roundabouts.

Bayata et al. [14] selected Erzincanpark as their study area to examine the significance of intersection coordination, traffic flow, and phase adjustments. They analyzed traffic volumes, signal optimization, travel time, queue length, delay, CO_2, NO_x, VOC emissions, and fuel consumption at intersections along Halitpaşa Street. The study results indicate that the Yıldız and Nedim Muratoğlu intersections should be redesigned as modern roundabouts to achieve optimal performance. Demiriz et al. [15] analyzed the increasing transportation demands and traffic congestion in Erzincan, where main arteries and intersections were found to be insufficient. Using the Aimsun program, simulations were conducted for the current situation and four alternative scenarios, with delay time and travel time serving as key design criteria, assessed through the Analytic Hierarchy Process (AHP). The study found reductions of up to 23% in travel time, 47% in delays, 48% in queue lengths, 11% in NO_x emissions, and 13% in CO_2 emissions, along with an increase of up to 30% in average speed.

Nguyen et al. [16] highlighted the impact of individual traffic behavior on environmental degradation and underscored the importance of innovation in sustainable mobility. The study demonstrated that agent-based models are particularly effective in addressing three key areas—resource usage, digital connectivity, and emerging forms of mobility—due to their ability to model heterogeneous individual behaviors. Furthermore, the authors evaluated existing simulators, examining both their modeling capabilities and identifying critical functional limitations. Çelikoglu and Dell'Orco [17] proposed a mesoscopic simulation methodology that incorporates vehicle acceleration and deceleration to address the complexities of flow propagation in transportation systems. The model is particularly effective in improving the accuracy of speed calculations on long road segments, such as highways. Simulation results indicate that the model realistically captures exit dynamics and is computationally efficient.

Mecheva et al. [18] present a methodology for integrating driver behaviors into traffic simulations by testing various car-following models and routing algorithms. Based on over 7,000 simulations using traffic data from Plovdiv, the study identifies the Contraction Hierarchies routing algorithm and the Krauss car-following model as providing the best overall performance and compatibility. In the study of Guo et al. [19], traffic simulation models were calibrated using extreme value theory, achieving alignment between simulated conflicts and field data. This approach enables more accurate crash predictions.

Qin et al. [20] developed a genetic algorithm-based calibration model in VISSIM for a signalized intersection in Beijing. By calibrating four driver behavior parameters, they reduced queue length error from 31.3% to 9.8% and travel time error from 15.2% to 7.3%, successfully replicating real-world traffic conditions. Zhang et al. [21] developed an efficient calibration framework for large-scale traffic simulators, based on meta-model simulation-based optimization algorithms. The meta-model incorporates analytical, structural, and problem-specific knowledge. It was applied to address a calibration problem for the Berlin network, which consists of 11,300 nodes. The proposed approach significantly enhances the computational efficiency of the calibration algorithm, achieving over 80% average reduction in simulation runtime. The results demonstrate the scalability of the approach and its suitability for calibrating large-scale, computationally intensive network simulators.

Although traffic congestion is often attributed to traffic signals, Moreno et al. [12] argue that human behavior also plays a significant role. To analyze the impact of human factors and their responses to the environment on traffic performance during waiting times, they developed an agent-based simulation that models both autonomous and social behaviors of road users. The results indicate that age is the most influential factor affecting individuals' behavior on the road. Xu et al. [22] present a system that operates using real-time data to deliver flexible signal control with the goal of reducing traffic congestion. The system offers three different control modes: fixed-time, multi-time, and adaptive. Supported by the SUMO simulation platform, the software enables smarter and more efficient traffic management.

Fabianova et al. [23] demonstrate how VISSIM software can be used to alleviate congestion at a signal-controlled intersection. To increase the throughput of a selected high-traffic intersection, two different improvement models were developed and simulated. The effectiveness of these models was evaluated based on vehicle queue lengths, a key indicator directly linked to traffic congestion. Both models significantly reduced queue lengths, particularly in the most congested directions. The first model achieved a 75% reduction in average queue length, while the second model improved the flow of right-turning vehicles and further reduced queues in other directions. Bindzar et al. [24] investigate the optimization of signal plans at urban intersections using ExtendSim8, a general-purpose simulation software, with the aim of alleviating traffic congestion. Based on real-world traffic data and observations, their modeling results show that this software can be an effective tool for urban traffic management.

Stevanovic et al. [25] demonstrate that traffic signal timings can be optimized using a three-dimensional Pareto analysis that considers mobility, safety, and environmental impacts. The proposed approach offers more balanced traffic management solutions by integrating both traditional methods and connected vehicle technologies. Cao et al. [26] aim to improve traffic management by using intelligent traffic light systems and simulations for continuous linear multiple intersections. Simulations conducted with Python and Vissim software provide an effective method for real-time adjustment of traffic signals at intersections, helping to reduce traffic congestion.

Baş et al. [27] simulated different intersection types using Aimsun software to reduce traffic congestion at the Tebrizkapı Intersection in Erzurum. They proposed the designs of a Modern Roundabout and a Grade-Separated Intersection as alternatives to the existing intersection type. Simulation results indicated that, despite its high cost, the Modern Roundabout design was the

most optimal solution. Bayata et al. [28] conducted a traffic simulation of seven signalized intersections in the city center of Erzincan and evaluated improvements across various parameters. Using the TOPSIS method, the ideal scenario was determined, resulting in significant improvements in factors such as CO_2 emissions, delay time, VOC and NO_x emissions, and queue length.

In the study by Demiriz et al. [29], the intersection near Erzincan Mengücek Gazi Education and Research Hospital—a major hub in the city with a capacity of 500 beds—was analyzed. During peak periods, up to 676 vehicles use roadside parking at this location. The study identified user expectations and needs, and simulated the intersection using the Microscopic Simulation Method with the Aimsun program. The most suitable intersection design was determined based on factors such as delay, travel time, stop duration, and overall feasibility. Xu et al. [30] adopted a data-driven approach to generate traffic behaviors from real-world driving logs. The method utilizes a two-level hierarchy between high-level intent inference and low-level driving behavior imitation to achieve high sample efficiency and behavior diversity, while also incorporating a planning module to ensure stable long-term behaviors. The method has been empirically validated with scenarios from two large-scale driving datasets, demonstrating balanced traffic simulation performance in terms of realism, diversity, and long-term stability.

Aimsun and other microsimulation tools accurately model traffic flow through the analysis of interactions among individual vehicles [31]. Urban planners and traffic engineers rely on simulation programs to increase the efficiency of transportation networks [32]. Aimsun was originally developed as a simulation tool for microscopic traffic studies in urban and extra-urban contexts, but it has since evolved. When the Aimsun software was first designed, intersection measurements were modeled in the AutoCAD program by taking points in the field and the existing values were used in the measurements [33].

Rodríguez et al. [34] used Aimsun software to simulate a new parking model with two sub-models: parking lot selection and search. This model, which accounted for sidewalk traffic, was implemented in microsimulation traffic software. Sub-model parameters were estimated using data from Santander, Spain, and a user preference survey. For policy testing, the model was executed in Aimsun via a Python 3.7 API. Yalçınlı et al. [35] report that it now generates simulation models at both mesoscopic and macroscopic scales. The microsimulation model's usefulness in depicting emissions is dependent on its ability to simulate vehicle dynamics and temporal evolution. The simulation phase faithfully duplicates each vehicle's dynamic behavior using several internal behavior models [36].

This study proposes to improve intersection design to address the growing transportation needs of Erzurum and alleviate traffic congestion. To improve traffic flow at the Erzurum Gürcükapı and Taşhan Intersections, we assessed the current conditions and conducted renovation studies. In this methodology, we developed four unique scenarios by rearranging the intersecting arms and integrating additional signaling systems. The research examined variables including travel time, delay time, waiting time, speed, queuing, and environmental effects—specifically instantaneous emissions of CO_2, NO_x, PM (Particulate Matter), and VOCs (Volatile Organic Compounds)—across five separate scenarios. To calculate the emission values, the emission model of Panis et al. [37] was used in Aimsun for the simulation scenarios created in this study. The aim was to improve sustainable and secure traffic flow. This document underscores the necessity for enhancements in the city's transportation infrastructure, particularly through the optimization of intersection efficiency.

In the study, different scenarios were analyzed using the Aimsun program and as a result of these analyzes, evaluations were made on parameters such as travel time, delay time, waiting time, speed, queuing, instant CO_2, NO_x, PM and VOC. In addition, the effects of geometric arrangements and direction changes on the intersection were examined and travel time,

delay time, queue lengths and waiting time were taken into account as criteria measuring traffic performance. As a result, it was determined which design and direction arrangements were more suitable and future traffic density changes were analyzed using count data. In this way, evaluations were made on the effective usability of the projects in the coming years.

1. Materials and Methods

1.1. Study area

The research area includes the Gürcükapı and Taşhan intersections in Erzurum province, as well as surrounding streets Taşhan and Habib Baba Street. Figure 1 depicts satellite images of the research area.

Figure 1. Satellite image of study area

Two alternative recommendations were chosen from a list of various choices, and 40 questionnaires were issued to see how changing the directions of Taşhan Street and Habib Baba Street might affect traffic flow for local businesses. A 3D model of the selected alternative projects, together with the current geometric configuration, was developed using SketchUp software. Data on intersection numbers and signal durations were obtained from the Transportation Planning Branch Directorate of Erzurum Metropolitan Municipality. Utilizing Aimsun simulation software, comparisons were conducted across three scenarios: the two

alternative designs and the existing intersection arrangement.

Traffic counts were performed at two intersections at peak hours on weekdays (morning, noon, and evening) and weekends (morning, noon, and evening) for a duration of one hour. The counts were derived from the vehicle types identified in the camera clip. Figures 2-5 present satellite imagery of the intersections along with the corresponding intersection count data.

Figure 2. Satellite image of Gürcükapı Intersection
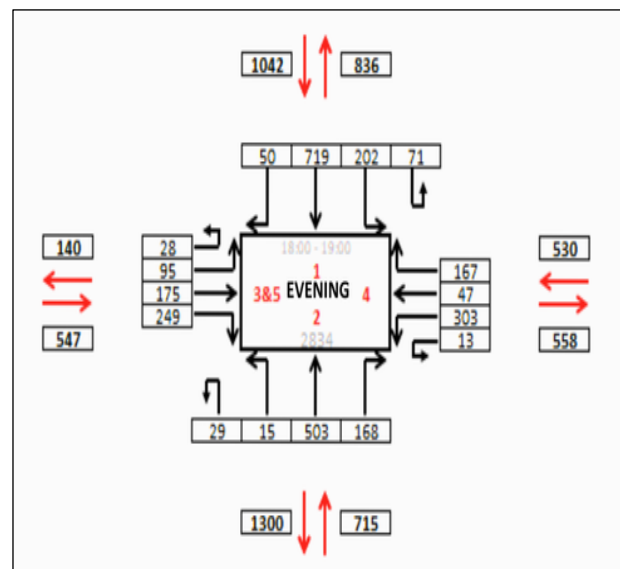
Figure 3. Vehicle Count Matrix of Gürcükapı Intersection (Evening 18:00-19:00)

Figure 4. Satellite image of Taşhan Intersection
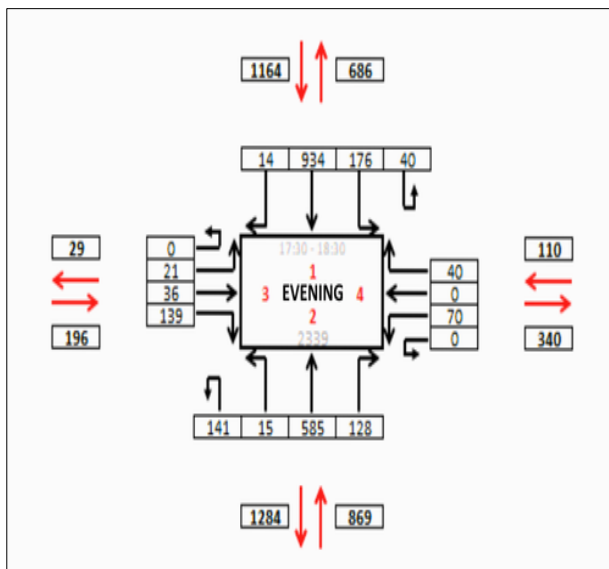
Figure 5. Vehicle Count Matrix of Taşhan Intersection (Evening 18:00-19:00)

1.2. Survey study

At the outset of the study, a structured survey was conducted targeting tradesmen operating within the Gürcükapı and Taşhan commercial districts. A total of 40 shop owners participated in the research. The findings showed a nearly even split: 49% of respondents favored changes—such as renovations, modernization, or improved business conditions—while 51% preferred to keep things as they are, indicating either satisfaction with the current setup or concerns about potential disruptions. Table 1 presents the questions from the survey conducted on these tradesmen.

1.3. Modeling of existing and alternative circumstances

When picking the type of intersection, it's important to think about things like safety, average delay, suitability for the land, and cost, and then choose the type that works best in these situations [38]. To better understand the performance of different intersection types, a comprehensive evaluation was conducted on ten distinct projects. This analysis focused on assessing the effectiveness of the selected intersection models by examining geometric arrangements and directional studies. These evaluations provide insight into how various intersection designs impact traffic flow, congestion, and overall accessibility. Figure 6-7 presents the existing and alternative situational models of the Gürcükapı and Taşhan intersections. Table 2 contains information about the current situation and scenarios.

Figure 6. Current state of Gürcükapı and Taşhan intersections
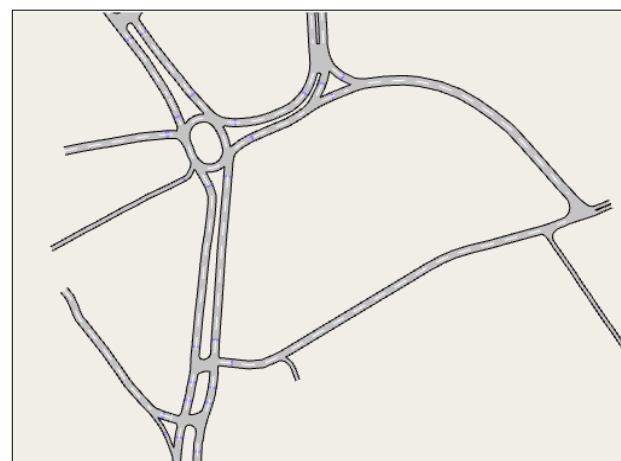
Figure 7. Alternative modeling of Gürcükapı and Taşhan intersections

Table 1. Gürcükapı-Ayaz Paşa direction survey study for commercial enterprise

	EXPLANATION	YES	NO	IF YOUR ANSWER NO, WHY?	
1	Are you satisfied with the current route from Gürcükapı Street to Kongre Street?				
2	Are you satisfied with the current route from Taşhan instersection to Ayaz Paşa?				
3	Do you think it is appropriate to use the one-way road from Kafaflar Street to Ayaz Paşa Street and use the Taşhan instersection as a two-way connection?				
4	Do you think it is healthy for the Ayaz Paşa Street-Bat Pazarı – Habib Baba road intersection to be used as a two-way street in terms of traffic safety?				
5	Do you find the median opening connecting Habib Baba to Gürcükapı Street appropriate?				
6	Do you think it is necessary to return from Habib Baba to Kafaflar Street?				
7	Do you think it would be appropriate to divert the traffic coming from Habib Baba Street behind the Gürcükapı Mosque?				
8	Do you think it would be appropriate to give the route from Kongre Street to Habib Baba?				
9	Which of our project direction alternatives would you prefer?	Alternative 1 ( )		Alternative 2 ( )	

Alternative 1(Current Direction)
- Coming from Istasyon Street, it continues in front of Guürcükapı Mosque to Kongre Street.
- Those coming from Habib Baba are connected to the Gürcükapı instersection from behind the Gürcükapı Mosque, without allowing those coming from Habib Baba to use the Gürcükapı instersection connection.
- Those coming from Gürcükapı will have a connection to Kafaflar Street, while those coming from Habib Baba and Kongre will not have a connection to Kafaflar Street.
- Those coming from Taşhan İnstersection will be able to go to Habib Baba by maintaining the current direction to Ayaz Paşa Street.
- Those coming from Ayaz Paşa will use Cedid and Eski Bat Pazarı in both directions.
- The Mahallebaşı direction route will continue in two directions.

Alternative 2 (Opposite Direction of Current State)
- Coming from the Istatsyon Street, it continues from the front of the Gürcükapı Mosque to the Kongre Street.
- They will be able to go to Habib Baba from Gürcükapı Street – Kongre Street.
- By changing the direction of Habib Baba Route, they will be able to go to Gölbaşı via the newly opened road.
- A connection will be provided from Habib Baba to Ayaz Paşa in the opposite direction of the existing road.
- There will again be two-way transportation from Habib Baba cemetery to Mahallebaşı
- Those coming from Mahallebaşı and Habib Baba will be able to go from Ayaz Paşa to Menderes Street.

Upon assessing the present circumstances, issues such as geometric irregularities at intersections, insufficient parking availability, double-row parking configurations, waste accumulation beyond designated lanes, inadequate pedestrian crossings jeopardizing safety, inappropriate spacing of existing pedestrian crossings, intersection geometry failing to adhere to roundabout specifications, turns lacking adequate storage areas, non-compliant islands, central medians not meeting established standards, complications at bus stops, directional ambiguities, and the absence of appropriate stops for articulated buses were identified.

These findings resulted in the development of project designs that integrated 10 unique directions and geometric alterations. Among the developed projects, progress was made on two alternative initiatives, considering the prevailing circumstances and minimizing damage to the geometric arrangement.

Gürcükapı Intersection: Despite the 2*2 configuration, Ayaz Paşa and Habib Baba Streets function unidirectionally due to the existing infrastructure and lane width. Vehicles entering from Ayaz Paşa Street continue to Gürcükapı Street and Kongre Street via Habib Baba Street. The project aims to decrease congestion at the Gürcükapı Intersection and plans to reorganize Habib Baba Street and Ayaz Paşa Street to create a counterclockwise ring.

When establishing one-way highways, it is essential to evaluate the origin and destination sites, intersections, land use issues, and the lengths of primary and secondary arteries [39]. One-way road implementations can be effective in cities with a systematic network configuration. Nevertheless, if the distances between roads are overly lengthy or if the road network is uneven, as observed in historic city centers, one-way systems may result in superfluous vehicular congestion and an escalation in traffic volume [40].

Table 2. Information about current status and alternative scenarios

	Geometrical Layout	Island Radius	Island	Signal Conditions	Direction Conditions
Current Status					
Gürcükapı	Currently, the lanes are used as either two-lane or single-lane configurations. The number of lanes fluctuates, leading to undefined lane spaces and the creation of double-row parking areas. The Gürückapı intersection is modeled as a roundabout, while the Taşhan intersection is modeled as a mini roundabout, with a four-node configuration.	15 m	None	The current signal system operates in 4 phases and in a storage format.	Ayaz Paşa Street flows towards Habib Baba Street, and Habib Baba Street directs traffic towards Kongre Street. A ring has been formed with a transition from Habib Baba Street to Gürcükapı Street.
Taşhan		7.75 m	4	None	
Same Direction Without Signaling					
Gürcükapı	In the design phase, the lanes have been set at 3 meters wide, with the remaining areas designated as parking pockets, and the leftover space has been allocated for sidewalks. At the Gürcü Kapı intersection, the island diameter has been increased to 30 meters. The existing Taşhan intersection with 4 nodes and the mini roundabout have been removed, and in their place, islands with a droplet shape have been designed, featuring separate entrances and exits.	30 m	None	The current signal system operates in 4 phases and in a storage format.	Same as "Current Status"
Taşhan		None	Teardrop Type Intersection	None	
Same Direction Without Signaling					
Gürcükapı	Same as "Same Direction Without Signaling"	30 m	None	The current signal system operates in 4 phases and in a storage format.	Same as "Current Status"
Taşhan		None	Teardrop Type Intersection	The signal assignment has been made to operate in 4 phases.	
Reveerse Direction With Signaling					
Gürcükapı	Same as "Same Direction Without Signaling"	30 m	None	The current signal system operates in 4 phases and in a storage format.	Gürcü Kapı Street flows towards Habib Baba Street and Kongre Street, while Habib Baba Street directs traffic towards Ayaz Paşa Street. Ayaz Paşa Street, in turn, forms a ring by directing traffic towards Cumhuriyet Street.
Taşhan		None	Teardrop Type Intersection	None	
Reverse Direction With Signaling					
Gürcükapı	Same as "Same Direction Without Signaling"	30 m	None	The current signal system operates in 4 phases and in a storage format.	Same as "Reverse Direction With Signaling"
Taşhan		None	Teardrop Type Intersection	The signal assignment has been made to operate in 4 phases.	

SketchUp is a widely used 3D modeling software, primarily employed in architecture, interior design, engineering, construction, and game design. Its compatibility with industry-standard file formats such as DWG and DXF, along with its seamless integration with other design software like AutoCAD, makes it an essential tool for professionals in various fields.

In this study, SketchUp was utilized to create a sub-database for the Aimsun program, which is used for traffic simulation and analysis. To ensure accuracy, buildings were modeled based on their real-world dimensions and appearance, providing a detailed visual representation. These models were then integrated into the program for further evaluation and project development.

Additionally, alternative intersection designs for Gürcükapı and Taşhan were modeled using SketchUp. Figures 8-9 illustrate different layout possibilities, while Figures 10-12 present signaling plans that compare the current traffic conditions with proposed alternative scenarios.

Figure 8. Alternative modeling of Gürcükapı Intersection with SketchUp

Figure 9. Alternative modeling of Taşhan Intersection with SketchUp
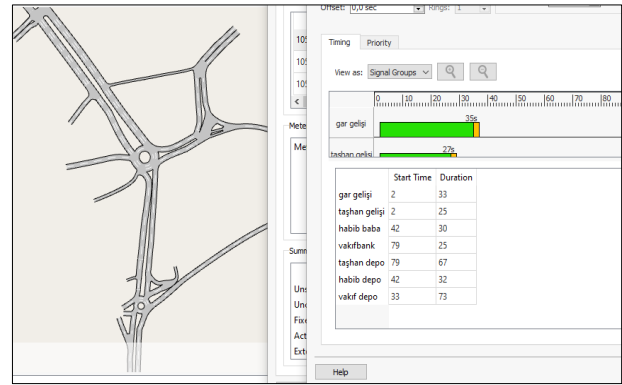
Figure 10. Current signal modelling of Gürcükapı Intersection
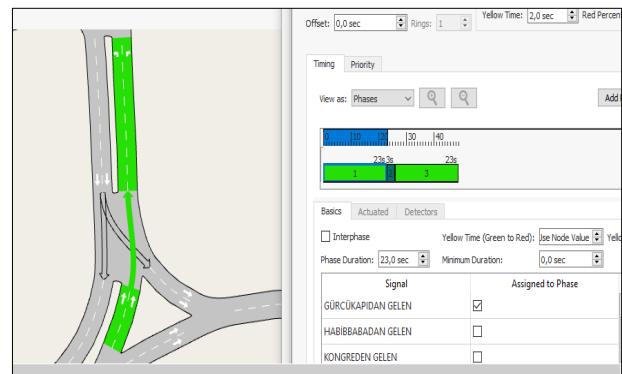
Figure 11. Signal modelling of Taşhan Intersection for alternative situations
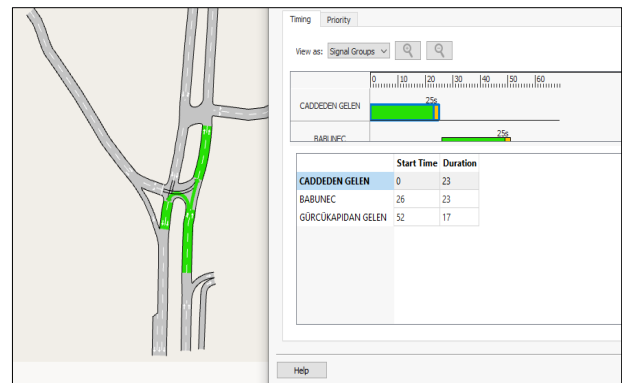
Figure 12. Signal modelling of Taşhan Intersection for alternative situations

2. Results and Discussion

The Aimsun program modeled the alternative projects as a SketchUp sub-model, arranging them according to new geometric designs. The existing intersection model, the geometrically arranged alternative project, and the geometrically arranged projects were simulated by changing the direction. The analysis values obtained later were compared in this section.

Figure 13. Comparison of the simulation findings between five scenarios using analysed metrics (IEM means Instantaneous Emission Model)

Figure 13 illustrates the simulation output results for the various scenarios. In this figure, it is indicated that the minimum delay time occurs in the same direction scenario without a signal (287.39), while the maximum delay time is observed in the reverse direction with a signal. While it is seen that signalization increases the delay time, it is found that the modernization of Gürcükapı and Taşhan intersections reduces the delays. It can be attributed that this situation is due to waiting at red lights. Changing the direction at the intersection also contributes to the delays.

When examining the speed parameter, it is observed that the current scenario (19.99) and the same-direction scenario with signals (19.97) produce the lowest speeds. On the other hand, the opposite-direction scenarios without signals (24.59) and with signals (25.37) yield similar speeds, indicating that a certain level of improvement is achieved by changing the directions of the intersection arms. However, the scenario that allows the fastest movement is the same-direction scenario without signals. This

suggests that changing the directions of the intersection arms does not provide significant benefits in terms of speed.

Similarly, the other parameters were obtained at least with the same direction scenario without a signal and at most with the reverse direction with a signal. This situation revealed that signalization increases queues, waiting time, travel time, and emissions (instant CO_2, NO_x, PM, and VOC), that the current situation is more efficient than the reverse direction of the junction arms, and that the modernization of the Gürcükapı and Taşhan junctions is effective on the mentioned parameters.

Figure 13 shows that the values for each parameter in the current situation and the unsignaled reverse direction scenarios are very close to each other. This means that the unsignaled reverse direction scenario is not likely to work and will only add to the costs. When the signaled same direction scenario is examined, it is found to be the second-best scenario for delay time, waiting time, and travel time; the second

worst scenario for average queue, instantaneous NO_x, VOC, and PM parameters; and the third worst scenario for instantaneous CO_2. The long travel times put pressure on the users participating in the traffic to reach the destination [41]. When this fact is combined with our findings, the fact that the scenario in question gives worse outputs than the current situation shows that it is meaningless to implement this scenario. The graph shows that the unsignaled same-direction scenario works at the Gürcükapı and Taşhan intersections, as well as on the roads that connect them. In this case, the study recommends implementing the scenario.

2.1. Comparison with other studies

In the study conducted by Çakıcı and Murat [13], a calculation method was developed for designing optimal signal timings and phase plans for approach lanes and flows around the roundabout. Although the study aligns with ours in the context of intersection optimization, its effectiveness was assessed by considering different intersection types and various phase plans, with delay as the primary performance criterion. This indicates a different perspective compared to our study. As such, it may serve as a valuable resource for future research aiming to evaluate intersection design from a broader perspective.

The findings of Bayata et al. [14] indicate that the Yıldız and Nedim Muratoğlu intersections in Erzincan should be designed as modern roundabouts to achieve optimal performance. Furthermore, for the Ergan Intersection, the study found no significant differences among the analyzed scenarios: signalized, four-leg (non-island), and modern roundabout designs. The study employed a decision-making methodology and, despite the evaluation of multiple alternatives, achieved successful results.

The study by Demiriz et al. [15] was carried out with the aim of alleviating the increasing traffic congestion in the city center of Erzincan, and therefore adopts a broad analytical perspective. In the study, 14 intersections were examined, and scenarios such as signal optimization, modern roundabouts, and grade-separated interchanges were evaluated. Using the Analytic Hierarchy Process (AHP), the most effective solution was identified as a combination of modern roundabouts and signal optimization.

Mecheva et al. [18] proposed a methodology that identifies the car-following model, routing algorithm, and their parameters, which best represent driving habits. This approach was implemented sequentially and in parallel using the urban mobility simulator SUMO and Python. The study offers opportunities to expand the methodology by incorporating additional adjustable components, such as lane-changing models or parameters. Their simulation-based solutions provide realistic and comprehensive results, with potential applications for intersection-based simulation studies in future research.

Zhang et al. [21] combined simulation-based optimization algorithms with Extreme Value Theory to optimize simulation calibration for large networks. This integration provided a framework for predicting traffic crashes through simulation. Their approach can serve as a guide for incorporating traffic safety considerations into intersection design in future studies.

3. Conclusion

The research designed four distinct scenarios that propose various geometric arrangements to improve the current situation at Gürcükapı and Taşhan intersections. These scenarios include four main options: signalized intersection, unsignalized intersection, signalized arm reverse intersection and a no-signal situation. Each scenario was compared with the current situation in terms of travel time, delay time, waiting time, speed, queuing and instantaneous emission values such as CO_2, NO_x, PM and VOC.

Following a thorough examination of the available data, it was determined that the option which demonstrated the most favourable performance of the four alternative scenarios presented a significant improvement in comparison to the current situation, particularly with regard to travel time, delay time and emission values. This scenario has been demonstrated to offer both an efficient travel experience and a reduction in traffic congestion

by considering traffic flow and environmental impacts. Consequently, Aimsun software was utilised as an effective tool in analysing and enhancing traffic networks at a micro scale, and the modelling process provided a significant solution for traffic management and environmental impact assessments. It is submitted that these findings can serve as a guide for local traffic policies and infrastructure development projects.

Article Information Form

Authors' Contribution
Conception / Design, Z. Zirek and M. A. Çolak; Data Collection, Z. Zirek and M. A. Çolak; Data Analysis / Interpretation, Z. Zirek and M. A. Çolak; Writing, Z. Zirek and M. A. Çolak; Technical Support / Material Support, Z. Zirek and M. A. Çolak; Critical Review of Content, Z. Zirek and M. A. Çolak; Literature Review, Z. Zirek and M. A. Çolak.

The Declaration of Conflict of Interest/ Common Interest
No conflict of interest or common interest has been declared by authors.

Artificial Intelligence Statement
No artificial intelligence tools were used while writing this article.

Copyright Statement

References

[1]   B. Kaba Genç, "Üniversite kampüslerinde sürdürülebilir karayolu ağının geometrik tasarımı: YTÜ Davutpaşa kampüsü örneği," Yüksek Lisans Tezi, Fen Bilimleri Enstitüsü, Yıldız Teknik Üniversitesi, İstanbul, 2018.

[2]   A. A. Camcı, "Kavşak tasarımında trafik simülasyon tekniklerinin kullanımı ve Sakarya için uygulamalar," Yüksek Lisans Tezi, Fen Bilimleri Enstitüsü, Sakarya Üniversitesi, Sakarya, 2019.

[3]   A. Sağlık, N. Ekiz, S. Bayram, M. Temiz, "Çanakkale Onsekiz Mart Üniversitesi Kavşağı peyzaj düzenlemesinin incelenmesi," PEYZAJ, vol. 2, pp. 78-85, 2020.

[4]   E. Papatzikou, A. Stathopoulos, "Rapid algorithm for finding the best combination of signaling phases using optimization methods," International Journal of Transportation Science and Technology, vol. 7, pp. 229-240, 2019.

[5]   S. Ataşoğlu, Sinyalize kavşaklarda farklı geometrik özelliklerin performans üzerine etkisinin incelenmesi, Yüksek Lisans Tezi, Fen Bilimleri Enstitüsü, Kırıkkale Üniversitesi, Kırıkkale, 2018.

[6]   L. Giannakos, E. Mintsis, S. Basbas, G. Mintsis, C. Taxilarits, "Simulating traffic and environmental effects of pedestrianization and traffic management. A comparison between static and dynamic traffic assignment," Transportation Research Procedia, vol. 24, pp. 313-320, 2017.

[7]   Z. Yetgin, "Kavşak tasarım-uygulama hatalarının analizine yönelik bir araştırma," Euroasia Journal of Mathematics, Engineering, Natural & Medical Sciences, vol. 7, pp. 149-157, 2020.

[8]   C. Vilarinho, G. Soares, J. Macedo, J. P. Tavares, R. J. Rossetti, "Capability-enhanced Aimsun with real-time signal timing control," Procedia-Social and Behavioral Sciences, vol. 111, pp. 262-271, 2014.

[9]   S. Akkaya, T. Engin, "Trafik simülasyon yazılımlarına genel bakış," Akıllı Ulaşım Sistemleri ve Uygulamaları Dergisi, vol. 5, pp. 157-168, 2022.

[10]   K. D. Alemdar, "Kavşak tasarımlarının karar verme teknikleri ile değerlendirilmesi," Yüksek Lisans Tezi, Fen Bilimleri Enstitüsü, Atatürk Üniversitesi, Erzurum, 2019.

[11] F. İ. Baş, M. Gökdağ, "The effect of fatigue and sleepiness upon driver behaviors," Erzincan University Journal of Science and Technology, vol. 12, pp. 850-862, 2019.

[12] A. C. Moreno, M. Moreno, C. Porras, J. Pavón "Human and environmental factors analysis in traffic using agent-based simulation," Applied Sciences, vol. 13, pp. 3499, 2023.

[13] Z. Çakıcı, Y. Ş. Murat, "Sinyalize dönel kavşaklar için hesap yöntemi önerisi ve performans analizi," Teknik Dergi, vol. 27, pp. 7569-7592, 2016.

[14] H.F. Bayata, F. İ. Baş, G. Ş. Mengi, "Traffic impact analysis of a regional shopping center using microsimulation with the Analytical Hierarchy Process (AHP) approach," Iranian Journal of Science and Technology, Transactions of Civil Engineering, vol. 49, pp. 1-9, 2024.

[15] A. O. Demiriz, O. Ü. Bayrak, H. F. Bayata, "Corridor capacity analysis with mesoscopic simulation: Erzincan province sample," Sādhanā, vol 46, pp. 10, 2021.

[16] J. Nguyen, S. T. Powers, N. Urquhart, T. Farrenkopf, M. Guckert, "An overview of agent-based traffic simulators," Transportation Research Interdisciplinary Perspectives, vol. 12, pp. 100486, 2021.

[17] H. B. Celikoglu, M. Dell'Orco, "Mesoscopic Simulation Of A Dynamic Link Loading Process," Transportation Research Part C: Emerging Technologies, vol. 15, pp. 329-344, 2007.

[18] T. Mecheva, R. Furnadzhiev, N. Kakanakov, "Modeling driver behavior in road traffic simulation," Sensors, vol. 22, pp. 9801, 2022.

[19] Y. Guo, T. Sayed, L. Zheng, M. Essa, "An extreme value theory based approach for calibration of microsimulation models for safety analysis," Simulation Modelling Practice and Theory, vol. 106, pp. 102172, 2021.

[20] Y. Qin, Q. hua Zhang, Y. fang Yang, Z. dong Zhang, "Parameter calibration of VISSIM simulation model based on genetic algorithm," In 2013 International Conference on Advanced Computer Science and Electronics Information, pp. 591-596, Atlantis Press, 2013.

[21] C. Zhang, C. Osorio, G. Flötteröd, "Efficient calibration techniques for large-scale traffic simulators," Transportation Research Part B: Methodological, vol. 97, pp. 214-239, 2017.

[22] H. Xu, X. Hou, R. Zhu, "The design of signal control software and intersection traffic simulation," In International Conference on Materials Engineering and Information Technology Applications, MEITA 2015, pp. 911-915, Atlantis Press, 2015.

[23] J. Fabianova, P. Michalik, J. Janekova, M. Fabian, M. "Design and evaluation of a new intersection model to minimize congestions using VISSIM software," Open Engineering, vol. 10, pp. 48-56, 2020.

[24] P. Bindzar, D. Macuga, J. Brodny, M. Tutak, M. Malindzakova, "Use of universal simulation software tools for optimization of signal plans at urban intersections," Sustainability, vol. 14, pp. 2079, 2022.

[25] A. Stevanovic, J. Stevanovic, J. So, M. Ostojic, "Multi-criteria optimization of traffic signals: Mobility, safety, and environment," Transportation Research Part C: Emerging Technologies, vol. 55, pp. 46-68, 2015.

[26] Z. Cao, J. Zhang, J. "Simulation design of continuous linear multiple intersection intelligent traffic light," In Proceedings of the 6th International Conference on Machine Learning and Machine Intelligence, pp. 157-163, 2023.

[27] F. İ. Baş, M. A. Çolak, A. O. Demiriz, H. F. Bayata, O. Ü. Bayrak, Ö. F. Keleş, M. S. Demircioğlu, "Kentiçi kavşakların

mikrosimülasyon yöntemiyle modellenmesi: Erzurum ili örneği," Avrupa Bilim ve Teknoloji Dergisi, pp. 444-451, 2020.

[28] H. F. Bayata, F. İ. Baş, M. S. Demircioğlu, M. A., Çolak, "Appropriate intersection design type based on TOPSIS multiple criteria decision method with AIMSUN mesoscopic simulation," Iranian Journal of Science and Technology, Transactions of Civil Engineering, vol. 49, pp. 1889-1899, 2025.

[29] A. O. Demiriz, O. Ü Bayrak, H. F. Bayata, F. İ. Baş, M. A. Çolak, Ö. F. Keleş, "Evaluation of Different Alternatives for the Intersection of Erzincan Province Trainning and Research Hospital with Microsimulation Modelling," Inertanional Congress on Engineering and Life Science, pp. 426, ICELIS, 2019.

[30] D. Xu, Y. Chen, B. Ivanovic, M. Pavone, "Bits: Bi-level imitation for traffic simulation," In 2023 IEEE International Conference on Robotics and Automation, pp. 2929-2936, IEEE, 2023.

[31] A. Granà, T. Giuffrè, E. Macioszek, F. Acuto, "Estimation of passenger car equivalents for two-lane and turbo roundabouts using AIMSUN," Frontiers in Built Environment, vol. 6, pp. 86, 2020.

[32] B. Beryan, "Kavşak tasarımında trafik simülasyonu uygulamaları: Bursa ili gürsu kavşağı örneği," Yüksek Lisans Tezi, Fen Bilimleri Enstitüsü, Manisa Celal Bayar Üniversitesi, Manisa, 2019.

[33] Aimsun. (1997). Aimsun's web page [Online]. Available: https://www.aimsun.com/

[34] A. Rodríguez, R. Cordera, B. Alonso, L. dell'Olio, J. Benavente, "Microsimulation parking choice and search model to assess dynamic pricing scenarios," Transportation Research Part A: Policy and Practice, vol. 156, pp. 253-269, 2022.

[35] F. Yalçınlı, B. Akdemir, A. Durdu, Ö. Yıldız, "Tam trafik uyarmalı sinyalizasyon sisteminin simülasyon modellemesi ve iyileştirme oranlarının saptanması," International Journal of Advanced Natural Sciences and Engineering, 2023.

[36] M. Y. Madi, "Investigating and calibrating the dynamics of vehicles in traffic micro-simulations models," Transportation Research Procedia, vol. 14, pp. 1782-1791, 2016.

[37] L. I. Panis, S. Broekx, R. Liu, "Modelling instantaneous traffic emission and the influence of traffic speed limits," Science of The Total Environment, vol. 371, pp. 270-285, 2006.

[38] E. Öğütveren, "Modern dönel kavşakların geometrik tasarımı ve kapasite ilişkisi," Yüksek Lisans Tezi, Fen Bilimleri Enstitüsü, Pamukkale Üniversitesi, Denizli, 2019.

[39] N. Alizadeh, "Analysing traffic network parameters after implementing one-way method: Hatay, Dörtyol case study," M.Sc. dissertation, Graduate School of Science Engineering and Technology, Istanbul Technical University, Istanbul, 2019.

[40] E. Gedizlioğlu, "Kentlerimizde trafik yönetimi," Türkiye Mühendislik Haberleri, vol. 434, pp. 17-22, 2004.

[41] P. Aksoy, "Işıklı Kavşaklarda Sola Dönüşlerde Sürücülerin Kurallara Uymamaları ile Trafik İşaretlemeleri ve Kavşak Geometrisi Arasındaki İlişkilerin İncelenmesi," Yüksek Lisans Tezi, Fen Bilimleri Enstitüsü, İstanbul Teknik Üniversitesi, İstanbul, 2019.

The Mechanical Properties of 6061-T6 Aluminum Alloy Joints Joined by MIG Welding Method (TPS/i) Using Different Shielding Gas Flow Rates

Erman Ferik[1*] (iD), Sedat Dağlaraştı[2] (iD), Faruk Varol[3] (iD)

[1] Marmara University, Faculty of Technology, Department of Metallurgical and Materials Engineering, İstanbul, Türkiye, erman.ferik@marmara.edu.tr, ror.org/02kswqa67
[2] Türkiye Rail System Vehicles Inc., Sakarya, Türkiye, sedatdaglarasti@gmail.com
[3] Sakarya University of Applied Sciences, Vocational School of Information Technologies, Department of Machinery, Sakarya, Türkiye, fvarol@subu.edu.tr, ror.org/01shwhq58
*Corresponding Author

ARTICLE INFO

ABSTRACT

In this study, aluminum 6061-T6 alloy sheets with a thickness of 3 millimeters were welded using the TPS/i MIG welding process. Welded samples were joined in the shape of butt joints. Argon was used as the welding shield gas, and the welded joint procedures were carried out at various shielding gas flow rates. Tensile strength and hardness values of the welded 6061-T6 aluminum alloy sheets were determined, and their microstructure and macrostructure were investigated using an optical microscope. The weldability of 6061-T6 aluminum sheets was investigated using the MIG welding process (TPS/i), and the impact of various shielding gas flow rates on mechanical parameters, macrostructures, and microstructures was studied.

1. Introduction

1.1. Aluminum's main features

Aluminum is a widely used and versatile metal that plays a crucial role in various industries, including aerospace and construction. Its low weight, corrosion resistance, and excellent thermal conductivity make it an ideal material for transportation across air, land, and sea, particularly in applications demanding a high strength-to-weight ratio.

The mechanical properties and strength of pure aluminum have been enhanced by incorporating alloying elements such as silicon, magnesium, and copper. As a result of advancements in aluminum alloy production, aluminum can now be employed in demanding environments, including aerospace and marine applications [1-10].

The 6061-T6 aluminum alloy examined in this study has a high concentration of magnesium and silicon. It is distinguished by its superior strength, excellent corrosion resistance, ease of fabrication, and good weldability. The T6 hardening process is a heat treatment that enhances the mechanical properties of aluminum alloys, particularly yield strength, tensile strength, and hardness in 6061 [11-15].

1.2. Welding procedure, MIG welding method and TPS/i

Welding is a widely utilized manufacturing technique across various industries, such as aerospace, automotive, and energy, for joining metals and thermoplastics. The resulting connection is known as a welded joint [16-18].

In the MIG/MAG welding process, the heat produced by an electric arc between a consumable metal electrode and the workpiece

generates a weld pool, which facilitates the fusion of the electrode and workpiece to create a welded joint.

In the MIG welding process, an inert gas such as argon or helium shields the arc and weld pool, whereas in the MAG welding method, an active gas like carbon dioxide protects them from environmental influences and contaminants. The MIG/MAG welding technique is widely used for welding low-alloy and unalloyed steels, high-alloy steels, stainless steels, and aluminum components [19-24].

Welding aluminum presents several challenges due to its inherent properties. Aluminum exhibits a strong affinity for oxygen, leading to the formation of an Al_2O_3 oxide layer on its surface. This oxide layer has a significantly higher melting point (2050°C) than aluminum itself, which melts at a much lower temperature. Consequently, it is essential to take preventive measures to inhibit oxide formation before welding. Moreover, aluminum and its alloys possess a high thermal conductivity, necessitating a greater heat input compared to steel to achieve the required heat concentration at the welding site.

Due to aluminum's substantial thermal expansion, welding processes often result in considerable distortions and internal stresses. Failure to implement appropriate precautions can lead to stress-induced cracks. Hot cracking is particularly prevalent in alloys with a broad solidification range, such as AlMn, AlSi, AlCu, and AlMg, and typically occurs along the solidus line or within the solidification zone. The most common challenges encountered in aluminum welding include oxidation, porosity, contamination, and hot cracking [25].

TPS/i (TransPuls Synergic/intelligent) is a pulsed-arc MIG/MAG welding system. Synergic refers to the machine's real-time adjustment of welding parameters such as voltage, current, wire feed speed, and other settings. This functionality means that if you modify one parameter, the others are automatically modified to provide the optimum overall welding performance. This can help welders, especially those without prior welding expertise, produce consistent, high-quality welds with minimal human intervention [26].

Shielding gas in MIG welding serves to protect the weld pool from contamination while also affecting various welding characteristics. These include arc stability, metal transfer type, penetration, wetting, weld seam geometry, heat input, welding speed, weld metal composition, smoke production, and mechanical properties. Increasing the shielding gas flow rate improves penetration and bead width but has minimal impact on deposition rate and bead size. Conversely, reducing the flow rate decreases penetration and bead width without affecting deposition rate or bead size. The optimal shielding gas flow rate depends on several factors, such as welding current, joint geometry, gas type, nozzle size, welding position, metal transfer mode (short arc, long arc, or spray arc), workpiece material (e.g., aluminum, stainless steel, or carbon steel), material thickness, joint preparation, and cost [27, 28].

During welding, the electrode, weld bead, and weld pool are subjected to various forces, including electromagnetic force, plasma shear voltage, arc pressure, surface tension, and gravity. The droplet detaches from the electrode tip and is transferred to the weld pool, where it solidifies to form the weld bead. This process is governed by the balance of these forces and is significantly influenced by welding parameters, particularly shielding gas. Shielding gases play a crucial role in altering these forces, thereby affecting metal transfer mode, weld penetration shape, weld bead size and form, and other welding characteristics. Therefore, selecting the appropriate shielding gas is essential for optimizing welding performance and minimizing the risk of fusion defects that could compromise structural integrity [29, 30].

In addition to optimizing parameters such as welding current and torch angle, the proper selection and use of shielding gases play a crucial role in determining weld quality. The shielding gas flow rate significantly impacts the final weld outcome; an insufficient flow rate fails to adequately protect the weld area, leading to contamination by atmospheric gases. This issue is typically mitigated by increasing the shielding

gas flow rate. However, an excessively high flow rate can create turbulence, drawing in atmospheric gases and compromising weld integrity. Due to the intense heat within the arc column, atmospheric gases become dissociated, absorbed, and dispersed into the weld pool. If buoyancy forces are insufficient to allow these gases to escape from the molten metal, porosity develops, trapping gas bubbles and resulting in voids within the solidified weld [31-36].

Argon is the most widely used gas in the industry due to its availability and lower cost compared to other inert gases. Since it is denser than air, it is primarily suitable for shielding welds in flat positions and deep groove joints, requiring a lower flow rate. Pure argon is commonly used for welding aluminum and other nonferrous metals. It offers excellent arc stability, effective cleaning action, and strong arc initiation properties. Additionally, it efficiently generates plasma, ensuring a steady and smooth-burning arc while exhibiting excellent electrical conductivity [37].

This study examines the TPS/i welding of 6061-T6 aluminum sheets using aluminum-based welding wire. The results indicate that while the welded samples exhibited lower strength than the base material, they still met the required acceptability standards. This article primarily explores the microstructure, strength characteristics, and welding processes of aluminum sheet joints produced using the TPS/i welding technique.

2. Material and Method

This study utilized 6061-T6 aluminum alloy sheets, commonly used in railway car construction. The chemical composition of these aluminum alloy sheets is presented in Table 1.

Table 1. Chemical composition of 6061-T6 aluminum alloy sheets ((Elements (wt%))

Fe	Si	Mn	Cr	Ti
0.451	0.653	0.123	0.144	0.0466
Cu	**Mg**	**Zn**	**Al**	
0.242	0.844	0.0612	97.5	

The mechanical characteristics of 6061-T6 sheets are presented in Table 2.

Table 2. Mechanical properties of 6061-T6 aluminum alloy sheets

Yield Strength (N/mm²)	Tensile Strength (N/mm²)	Elongation (%)
260	285	12

The 6061-T6 aluminum alloy sheets were cut to dimensions of 150×300×3 mm. The dimensions of the samples are illustrated in Figure 1.
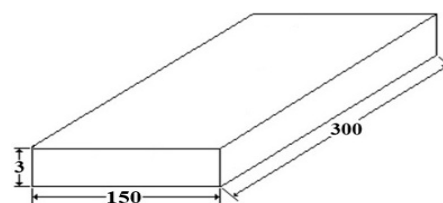
Figure 1. Dimensions of cut parts (mm)

Figure 2 shows the measurements of the welded samples.
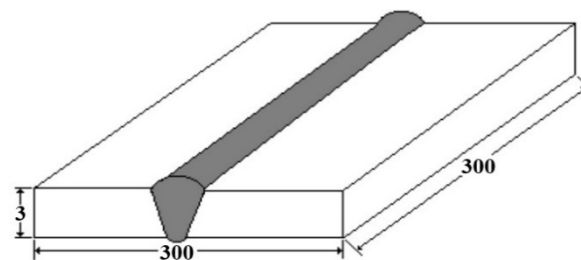
Figure 2. Dimensions of welded parts (mm)

The samples were chemically pre-cleaned with isopropyl alcohol before welding. Al 5356 welding filler metal, with a thickness of 1.2 mm, was used for the welding process. The welding was conducted in the PA position using a butt joint (BW) configuration. High-quality argon served as the shielding gas, with three different flow rates selected: 5 l/min, 12 l/min, and 20 l/min. The chemical composition of the welding filler wire is presented in Table 3.

Table 3. Chemical composition of Al 5356 welding filler wire ((Elements (wt%))

Fe	Si	Mn	Cr	Ti
0.40	0.25	0.10	0.10	0.10
Cu	**Mg**	**Zn**	**Al**	
0.10	4.75	0.10	94.1	

2.1. Welding procedure

The aluminum sheets were welded using a MIG welding machine (Fronius TPS 400i), where the shielding gas flow rates were varied while maintaining all other parameters constant. MIG welding (TPS/i) was carried out at three different

shielding gas flow rates: 5 l/min, 12 l/min, and 20 l/min. The welding parameters used are presented in Table 4.

Table 4. Welding parameters used in the welding process

Current (A)	Voltage (V)	Advance Speed (cm/min)
110	18.1	50
110	18.1	50
110	18.1	50
Wire Feed Speed (m/min)	Free Wire Length (mm)	Shielding Gas Flow Rate (l/min)
6.4	15	5
6.4	15	12
6.4	15	20

Figure 3 presents a representative image of the welded test samples.

Figure 3. Sample image of welded parts

Figure 4 displays the tensile, notch impact, and microstructure test samples.

Figure 4. Tensile test, notch impact test and microstructure test samples **a)** 5 l/min (19), **b)** 12 l/min (18), **c)** 20 l/min (20)

2.2. Characterization of materials

The chemical analysis of the aluminum sheet and aluminum welding filler wire used in the experiments was conducted using a spectrometer (Spectrolab 5M). Additionally, tensile testing was performed with an Instron 300DX, notch impact testing with an Instron 300FT, and hardness testing with a Qness Q700M. The equipment used is shown in Figure 5.

Figure 5. Devices used for testing welded samples, spectrometer instrument (a), tensile tester (b), notched impact tester (c), hardness tester (d)

3. Results and Discussion

3.1. Tensile test results

Figures 6, 7, and 8 present the tensile testing results of the samples welded using different shielding gas flow rates. The tensile tests were conducted in accordance with the TS EN ISO 6892-1 standard.

The tensile strength and elongation values of samples welded at varying gas flow rates were measured using a tensile testing apparatus and presented in diagrams.
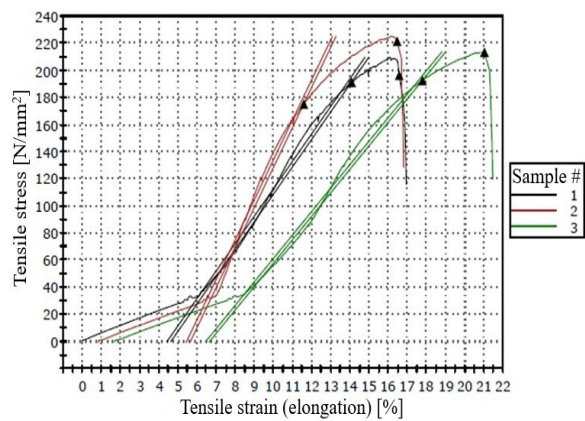
Figure 6. Graphical representation of tensile test samples which welded at a weld shield gas flow rate of 5 liters per minute
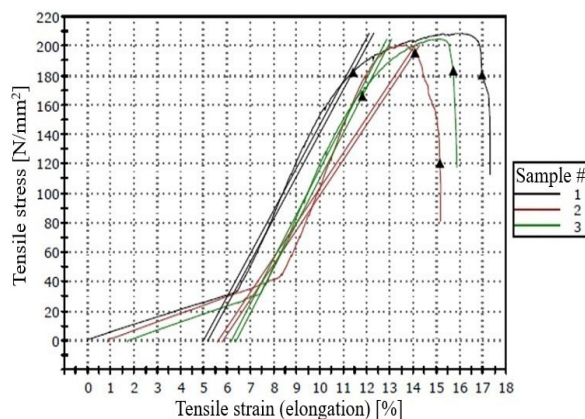
Figure 7. Graphical representation of tensile test samples which welded at a weld shield gas flow rate of 12 liters per minute

The results of the tensile tests are presented in Table 5. The tensile test results indicate that the sample welded with a shielding gas flow rate of 5 l/min has an average yield strength of 186 MPa, a tensile strength of 215 MPa, and an elongation of 10%. The sample welded at 12 l/min exhibits an average yield strength of 181 MPa, a tensile strength of 204 MPa, and 9% elongation. Meanwhile, the sample welded at a shielding gas flow rate of 20 l/min shows an average yield strength of 166 MPa, a tensile strength of 222 MPa, and an elongation of 10%.

Table 5. Table of tensile test results

Shielding Gas Flow Rate (l/min)	Yield Strength (MPa)	Tensile Strength (MPa)	Elongation (%)
5	186	215	10
12	181	204	9
20	166	222	10
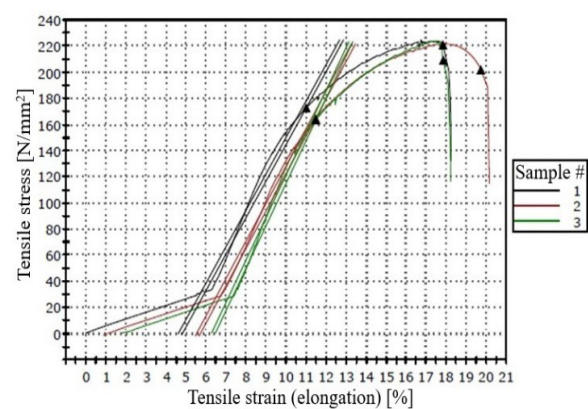
Figure 8. Graphical representation of tensile test samples which welded at a weld shield gas flow rate of 20 liters per minute.

According to the acceptance criterion specified in Table 2 of the EN 15614-2 Standard: Specification and Qualification of Welding Procedures for Metallic Materials–Arc Welding of Aluminium and Its Alloys, the tensile strength of the welded material must be at least 70% of the base material's tensile strength. The weldability results meet this requirement and are deemed satisfactory across all shielding gas flow rates.

Welded joints exhibit lower strength and elongation compared to the base metal region due to the heterogeneous microstructure that develops in different areas of the weld. The formation of a dendritic structure in the weld metal and grain coarsening in the heat-affected zone (HAZ) contribute to the reduction in tensile strength compared to the columnar grain structure of the base metal. Under tensile loading, stress becomes concentrated in the softened HAZ, ultimately causing the welded specimen to rupture. This is primarily attributed to the dissolution of hardening precipitates in the HAZ during the welding process [38].

3.2. Notch impact test results

To evaluate the energy absorbed by the welded samples during fracture under applied force, two specimens were taken from the base material, heat-affected zone (HAZ), and weld seam regions. A notch impact test was conducted, and the results are presented in Table 6. The test was performed using a V-notch in the welded samples, following the TS EN ISO 9016 standard.

Table 6. Notch impact test results

Impact Toughness at 23°C (Joule)			
Shielding Gas Flow Rate (l/min)	Base Metal	HAZ	Welded Metal
5	33	27	20
12	33	33	33
20	33	30	33
Impact Toughness at -20°C (Joule)			
Shielding Gas Flow Rate (l/min)	Base Metal	HAZ	Welded Metal
5	33	27	20
12	33	33	27
20	33	33	27

An analysis of the notch impact test results revealed a reduction in impact toughness in both the heat-affected zone (HAZ) and the weld metal region at all temperatures when using a shielding gas flow rate of 5 l/min. At a shielding gas flow rate of 12 l/min, impact toughness decreased in the weld metal region at -20°C. Similarly, at a shielding gas flow rate of 20 l/min, impact toughness declined in the HAZ at 23°C and in the weld metal region at -20°C. The decrease in notch impact strength with temperature is attributed to the material transitioning below the ductile-brittle transition temperature.

3.3. Hardness test results

The hardness of the welded samples was tested on the base metal, HAZ, and welded metal regions. Table 7 shows the results of the hardness test.

Table 7. Hardness test results

Shielding Gas Flow Rate (l/min)	Base Metal (HV)	HAZ (HV)	Welded Metal (HV)
5	63.5	63.5	63.5
12	72.4	52.1	65.5
20	71.6	67.1	58.5

An analysis of the hardness test results revealed only a slight difference in hardness between the base metal and the weld metal across all three samples. This is attributed to the use of an aluminum filler metal with properties similar to those of the base metal. However, the hardness in the heat-affected zone (HAZ) was lower than in both the weld metal and base metal. This reduction in hardness is primarily due to grain structure coarsening in the HAZ and the loss of strength resulting from heat input during welding.

The reduction in hardness and strength in welded joints can be attributed to precipitate phase transformations, grain coarsening, and changes in the dissolved element content. The microhardness values are expected to show a slight increase from the base metal toward the heat-affected zone (HAZ), while a slight decrease in hardness is anticipated from the HAZ toward the weld region.

An analysis of the hardness test results showed a slight difference in hardness between the base metal and weld metal regions in the samples welded at 12 l/min and 20 l/min. The heat-affected zone (HAZ) exhibited lower hardness compared to both the weld metal and base metal, primarily due to grain structure expansion and the loss of strength caused by heat input in this region. In contrast, the hardness values were consistent across all regions in the sample welded at 5 l/min.

The softening of the heat-affected zone (HAZ) in 6061-T6 aluminum alloy is influenced by various complex factors, including precipitate phase transitions, changes in elemental composition within the matrix, and variations in grain size. However, research on the microscopic mechanisms underlying HAZ softening in welded 6061-T6 aluminum alloy remains limited. Additionally, the extent to which these factors contribute to HAZ softening has not yet been fully established.

3.4. Macrostructure results

Figure 9 presents macrostructure images of all three samples. The weld cap and weld root areas formed at different shielding gas flow rates, as well as the welding defects that occurred, were assessed following the welding process.
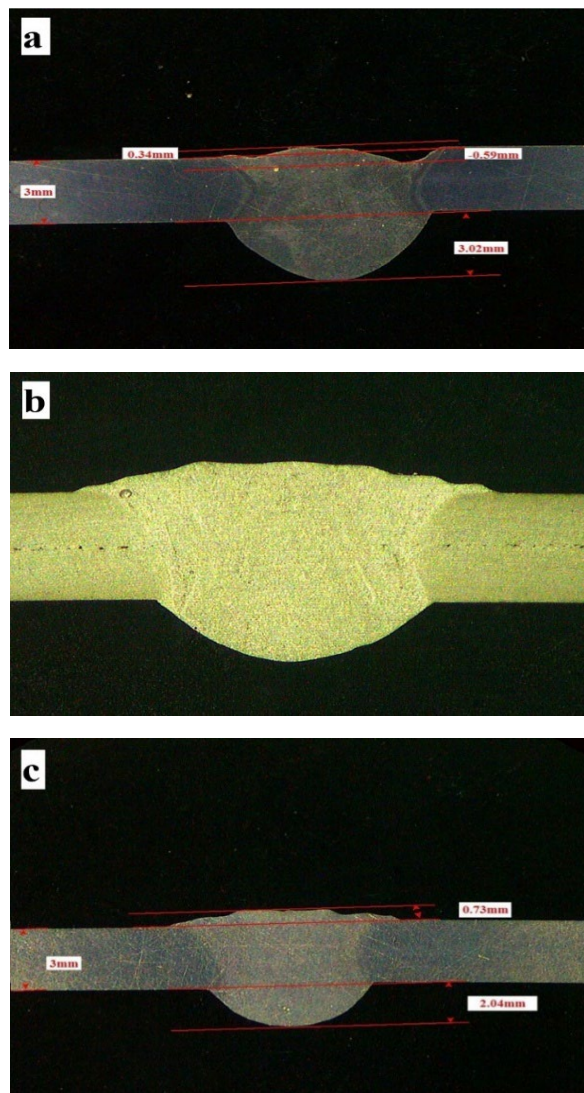
Figure 9. Macrographs of welded samples, a) 5 l/min shielding gas flow rate, b) 12 l/min shielding gas flow rate, c) 20 l/min shielding gas flow rate

As shown in the figure, the sidewall and root penetrations of all welded samples are within acceptable limits. The smallest weld cap size was recorded in the sample welded with a shielding gas flow rate of 5 l/min. Additionally, excessive root sagging was observed in this sample.

3.4. Microstructure results

Microstructure images were captured from multiple locations on the welded samples. To obtain microstructure images, the samples were sanded using 60–1200 grit sandpaper, polished with an alumina solution and polishing felt, and then etched with Keller's reagent (1 ml HF, 1.5 ml HCl, 2.5 ml HNO_3, 95 ml H_2O). After etching, the samples were examined under an optical microscope, and images were captured. Figures 10, 11, and 12 display the microstructure images of the base metal, heat-affected zone (HAZ), and weld metal regions of the welded samples at 100X magnification.
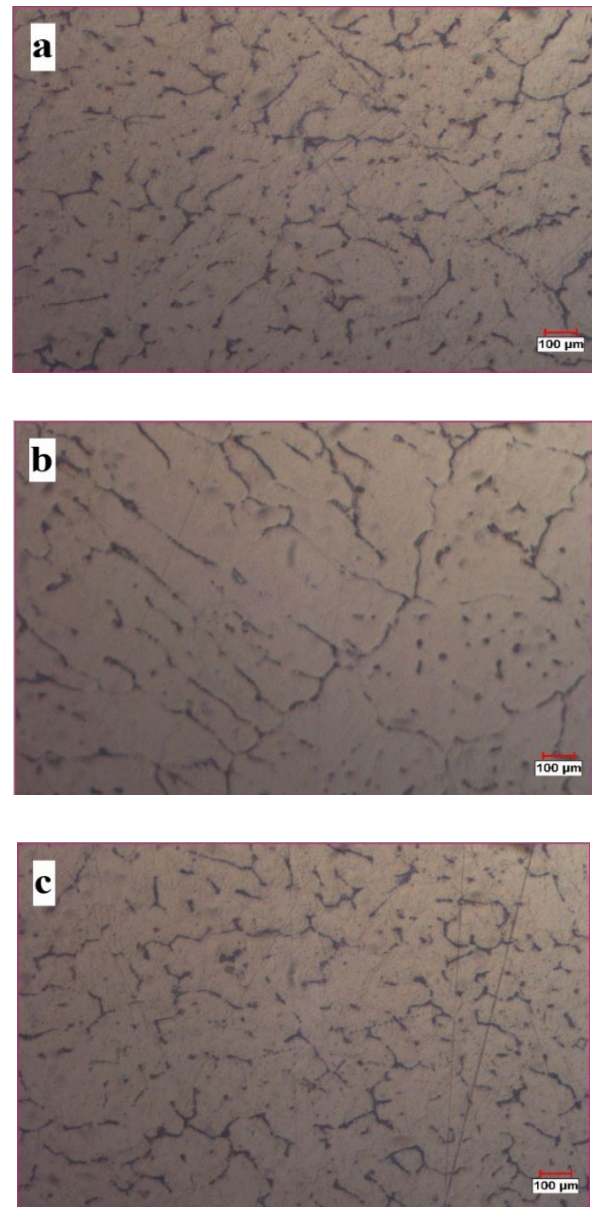
Figure 10. Micrograph images of the welded sample with 5 l/min protective gas flow rate, a) Base metal 100X, b) HAZ 100X, c) Welded metal 100X

After welding, distinct structural formations were observed in the base metal, heat-affected zone (HAZ), and weld metal regions. The microstructure of the welded samples can be broadly divided into three distinct regions: the weld region, the heat-affected zone (HAZ), and the base metal region. The weld region primarily consists of numerous dendritic grain structures along with equiaxed grains.
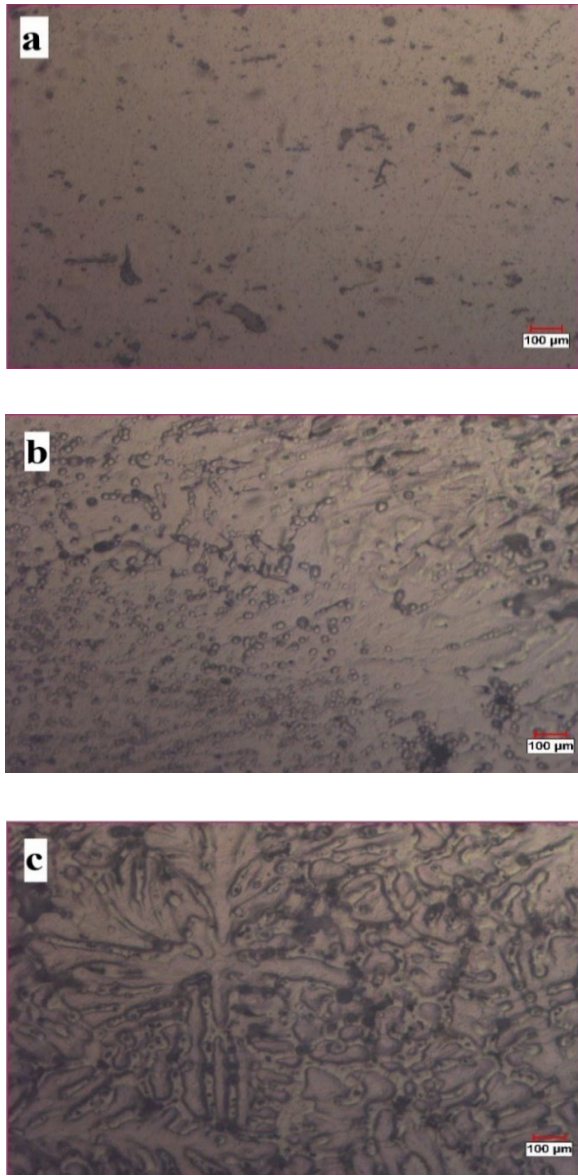
Figure 11. Micrograph images of the welded sample with 12 l/min protective gas flow rate, a) Base metal, 100X, b) HAZ 100X, c) Welded metal 100X

Figure 12. Micrograph images of the welded sample with 20 l/min protective gas flow rate, a) Base metal 100X, b) HAZ 100X, c) Welded metal 100X

A transition zone was present between the weld region and the heat-affected zone (HAZ). The microstructure of the HAZ was characterized by changes in grain morphology. The area of the HAZ closest to the weld experienced significant heating, leading to recrystallization within the rolled microstructure and the formation of large grains. This increase in grain size influences the mechanical properties of the welded joint, contributing to softening in the HAZ.

Additionally, the thermal cycling during welding alters the alloy's microstructure, further impacting the mechanical properties of the weld.

According to the literature, grain boundaries in the HAZ tend to grow as Mg_2Si structures due to the formation of silicon- and magnesium-rich precipitates. In contrast, the base metal region primarily consists of small equiaxed grains [39-44].

The welding thermal cycle affects the normal phase transformation of Al-Mg-Si alloys such as 6061-T6, and the β'' and β' phases formed during the Al-Mg-Si precipitation stages have a very important effect on the strength of Al-Mg-Si alloys. Their amount, size and distribution directly affect the mechanical properties of these alloys [45-49].

The complex welding thermal cycle in these alloys, along with the resulting variations in

dissolved element content across different regions of the joint, leads to microstructural transformations. These changes make it challenging to fully understand the underlying causes of the deterioration in the joint's mechanical properties [50-52].

During the welding process of Al-Mg-Si alloys, the arc melts both the welding wire and a portion of the base metal, forming a molten pool. The temperature of this molten pool exceeds the dissolution temperature of the β' and β'' phases, causing the nanoscale β' and β'' phases in the base metal to completely dissolve. During the subsequent cooling process, these phases precipitate as large β-Mg_2Si phases. Additionally, some of the Mg element in the base metal is burned off during welding, contributing to the softening of the weld zone. The combined effects of β-Mg_2Si phase precipitation and Mg element loss lead to significant weld zone softening. Since the β-Mg_2Si phase is incompatible with the $\alpha(Al)$ matrix and provides minimal strengthening, it further exacerbates softening in the weld zone. The transformation behavior of the primary strengthening phase (β'') in the base metal during the welding thermal cycle is the key factor responsible for this softening [53, 54].

Due to its low heat input characteristics and the absence of surface porosity and other defects on the weld surface, the TPSi welding method is suitable for use [55].

4. Conclusion

The data obtained as a result of the study are shown below.

- The welded samples exhibited lower tensile and yield strengths compared to the base metal. The tensile strength varied depending on the shielding gas flow rate. The highest tensile strength was observed in samples welded at a shielding gas flow rate of 20 l/min, while the highest yield strength was recorded in samples welded at a flow rate of 5 l/min.

- An analysis of the notch impact test results revealed that the impact toughness of the heat-affected zone (HAZ) and weld metal regions decreased at all temperatures when a shielding gas flow rate of 5 l/min was used. It was found that low shielding gas flow rates directly influence notch impact energy.

- Vickers hardness values were determined for the base metal, HAZ, and welded metal regions in each shielding gas flow sample and found to be comparable.

- An examination of the macrostructure images revealed that the desired weld filler metal height in the cap was not achieved in the sample welded with a shielding gas flow rate of 5 L/min.

- An analysis of the microstructure samples revealed that the images obtained from the base metal, heat-affected zone (HAZ), and weld metal regions in all three samples were highly similar.

In conclusion, 6061-T6 aluminum sheets, which are widely used in the industry, were successfully welded using the MIG welding process (TPS/i) with optimal shielding gas flow rate parameters.

Article Information Form

Authors' Contribution
Erman Ferik wrote the paper, reviewed the content critically, and conducted a literature review.
Sedat Dağlaraştı handled conception, data collecting, and material assistance.
Faruk Varol handled design, data collecting, and technical support.

The Declaration of Conflict of Interest/ Common Interest
No conflict of interest or common interest has been declared by authors.

Artificial Intelligence Statement
No artificial intelligence tools were used while writing this article.

References

[1] E. L. Persson, Aluminum Alloys: Preparation, Properties, and Applications, New York: Nova Science Publishers Inc, 2011.

[2] G. E. Toten, D. S. Mackenzie (eds.), Handbook of Aluminum: Volume 1: Physical Metallurgy and Processes, New York: Marcel Dekker Inc, 2003.

[3] K. Anderson, J. Weritz, J. G. Kaufman (eds.), ASM Handbook Volume 2A - Aluminum Science and Technology, Ohio: ASM International, 2018.

[4] Z. Fang, J. Cao, Y. Guan, Corrosion Control Technologies for Aluminum Alloy Vessel, Singapore: Springer, 2020.

[5] H. Abramovich, Advanced Aerospace Materials: Aluminum-Based and Composite Structures, 2nd ed. Berlin: Walter de Gruyter GmbH, 2023.

[6] H. Liu, J. Li, Z. Ma, B. Ma, S. Feng, "Study on mechanical properties and microstructure analysis of welded joints of 7A05 aluminum alloy by laser-MIG hybrid welding," In 2nd International Conference on Electronic & Mechanical Engineering and Information Technology, France: Atlantis Press, 2012, pp. 1465-1470.

[7] G. E. Totten, M. Tiryakioglu, O. Kessler (eds.), Encyclopedia of Aluminum and Its Alloys, Boca Raton: CRC Press, 2018.

[8] V. S. Zolotorevsky, N. A. Belov, M. V. Glazoff, Casting Aluminum Alloys, Oxford: Elsevier Ltd, 2007.

[9] J. R. Davis, Aluminum and Aluminum Alloys, Ohio: ASM International, 1999.

[10] L. F. Mondolfo, Aluminum Alloys: Structure and Properties, London: Butterworth-Heinemann, 1976.

[11] The Aluminum Association, Aluminum Design Manual, Specifications & Guidelines for Aluminum Structures, 8th ed. Washington: The Aluminum Association, Inc, 2005.

[12] G. E. Totten, D. S. MacKenzie, Handbook of Aluminum: Volume 2: Alloy Production and Materials Manufacturing, New York: Marcel Dekker Inc, 2003.

[13] J. G. Kaufman, Introduction to Aluminum Alloys and Tempers, Ohio: ASM International, 2000.

[14] J. R., Kissell, R. L. Ferry, Aluminum Structures: A Guide to Their Specifications and Design, 2nd ed. New York: John Wiley & Sons, 2002.

[15] H. J. McQueen, S. Spigarelli, M. Kassner, E. Evangelista, Hot Deformation and Processing of Aluminum Alloys, Boca Raton: CRC Press, 2016.

[16] D. Luo, Y. Xiao, L. Hardwick, R. Snell, M. Way, X. S. Morell, F. Livera, N. Ludford, C. Panwisawas, H. Dong, R. Goodall, "High entropy alloys as filler metals for joining," Entropy, vol. 23, no. 1, pp. 78-101, 2021.

[17] S. Anık, Kaynak Tekniği El Kitabı: Yöntemler ve Donanımlar, İstanbul: Gedik Eğitim Vakfı, 1991.

[18] D. H. Phillips, Welding Engineering An Introduction, 2nd ed. New Jersey: John Wiley & Sons, Inc., 2023.

[19] N. Kahraman, B. Gülenç, Modern Kaynak Teknolojisi ve Kaynak İşlerinde İş Sağlığı ve Güvenliği, Genişletilmiş 4. Baskı. Epa-Mat Basım Yayın Ltd, Şti: Ankara, 2020.

[20] G. Çam, Kaynak Bilimi ve Teknolojisi, Ankara: Nobel Akademik Yayıncılık, 2020.

[21] A. Çelik, Kaynak Teknolojileri, Ankara: Nobel Akademik Yayıncılık, 2020.

[22] S. E. Hughes, A Quick Guide to Welding and Weld Inspection, Cambridge: Woodhead Publishing, 2009.

[23] R. L. O'Brien, Welding Handbook. Volume 2: Welding Processes: Part 1, 9th ed. Miami: American Welding Society, 2004.

[24] K. Weman, G. Lindén, (eds.), MIG Welding Guide, Cambridge: Woodhead Publishing, 2006.

[25] T. Anderson, Welding Aluminum: Questions and Answers: A Practical Guide for Troubleshooting Aluminum Welding-related Problems, 2nd ed. Miami: American Welding Society, 2010.

[26] Fronius International Gmbh. (2025.05.20) TransSynergic 4000/5000, TransPuls Synergic 2700, TransPuls Synergic 3200/4000/5000, TIME 5000 Digital, CMT 4000 Advanced Kullanım Kılavuzu [Online]. Available: https://www.alganmetal.com.tr/images/gallery_files/74814ts_tps_kullanim_kilavuzu_yeni.pdf

[27] K. R. Madavi, B. F. Jogi, G. S. Lohar, "Metal Inert Gas (MIG) Welding Process: A Study of Effect of Welding Parameters," Materials Today: Proceedings, vol 51, pp. 690-698, 2022.

[28] G. M. Evans, N. Bailey, Metallurgy of Basic Weld Metal, Cambridge: Woodhead Publishing Limited, 1997.

[29] K. Badwal, P. Khanna, "Investigation of effect of shielding gases on angular distortion and bead profile parameters of MIG welded stainless steel 409L plates," Materials Today: Proceedings, vol 56, pp. 645-649, 2022.

[30] Z. H. Rao, J. Hu, S. M. Liao, H. L. Tsai, "Study the shielding gas effect on the metal transfer and weld pool dynamics in GMAW," In Heat Transfer Summer Conference, California, USA, vol. 43581, 2009, pp. 675-684.

[31] C. Cai, S. He, H. Chen, W. Zhang, "The influences of Ar-He shielding gas mixture on welding characteristics of fiber laser-MIG hybrid welding of aluminum alloy," Optics & Laser Technology, vol. 113, pp. 37-45, 2019.

[32] S. W. Campbell, A. M. Galloway, G. M. Ramsey, N. A. McPherson, "A potential solution to GMAW gas flow optimisation," In Trends in Welding Research 2012: Proceedings of the 9th International Conference, Chicago, USA, pp. 453-460, 2012.

[33] G. D. Uttrachi, "GMAW shielding gas flow control systems," Welding Journal, vol. 86, no. 4, pp. 22-23, 2007.

[34] S. W. Campbell, A. M. Galloway, N. A. McPherson, "Techno-economic evaluation of reducing shielding gas consumption in GMAW whilst maintaining weld quality," The International Journal of Advanced Manufacturing Technology, vol. 63, pp. 975-985, 2012.

[35] W. Lucas, S. Westgate, "Welding and Soldering," in Electrical Engineer's Reference Book, M. A. Laughton, D. J. Warne Eds. Oxford: Elsevier Science, pp. 246-298, 2003.

[36] C. Rajendran, T. Sonar, M. Ivanov, C. Sandeep, C. Shanthi, N. K. Gurajala, K. Balachandar, J. Xu, "Enhancing tensile properties of pulsed CMT–MIG welded high strength AA2014-T6 alloy joints: effect of post weld heat treatment," International Journal of Lightweight Materials and Manufacture, vol. 7, no. 2, pp. 344-352, 2024.

[37] Z. Ye, H. Zhu, S. Wang, W. Wang, J. Yang, J. Huang, "Fabricate high-strength 7075 aluminum alloy joint through double pulse MIG welding process," Journal of Manufacturing Processes, vol. 125, pp. 512-522, 2024.

[38] V. Singh, Q. Murtaza, M. S. Niranjan, "Microstructure and mechanical properties of CMT welded AA6063-T6/B4C/ES metal matrix composite using ER5356 filler wire," Materials Today: Proceedings, 2024.

[39] S. T. Selvamani, "Microstructure and stress corrosion behaviour of CMT welded AA6061 T-6 aluminium alloy joints," Journal of Materials Research and Technology, vol. 15, pp. 315-326, 2021.

[40] Z. Shen, R. H. Wagoner, W. A. T. Clark, "Dislocation and grain boundary interactions in metals," Acta Metallurgica, vol. 36, no. 12, pp. 3231-3242, 1988.

[41] M. P. Anderson, D. J. Srolovitz, G. S. Grest, P. S. Sahni, "Computer simulation of grain growth—I. kinetics," Acta Metallurgica, vol. 32, no. 5, pp. 783-791, 1984.

[42] S. Yang, X. Yang, X. Lu, M. V. Li, H. Zuo, Y. Wang, "Strength calculation and microstructure characterization of haz softening area in 6082-T6 aluminum alloy CMT welded joints," Materials Today Communications, vol. 37, 107077, 2023.

[43] M. Zhu, S. Yang, Y. Bai, C. Fan, "Uneven hardness mechanism and related fracture characteristics in laser-MIG hybrid welded Al–Mg–Si alloy butt," Journal of Laser Applications, vol. 33, no. 4, pp. 42-54, 2021.

[44] M. A. Van Huis, J. H. Chen, H. W. Zandbergen, M. H. F. Sluiter, "Phase stability and structural relations of nanometer-sized, matrix-embedded precipitate phases in Al–Mg–Si alloys in the late stages of evolution," Acta Materialia, vol. 54, no. 11, pp. 2945-2955, 2006.

[45] J. H. Chen, E. Costan, M. A. Van Huis, Q. Xu, H. W. Zandbergen, "Atomic pillar-based nanoprecipitates strengthen AlMgSi alloys," Science, vol. 312, no. 5772, pp. 416-419, 2006.

[46] C. D. Marioara, H. Nordmark, S. J. Andersen, R. Holmestad, "Post-β'' phases and their influence on microstructure and hardness in 6xxx Al-Mg-Si alloys," Journal of Materials Science, vol. 41, pp. 471-478, 2006.

[47] H. Liu, S. Yang, C. Xie, Q. Zhang, Y. Cao, "Microstructure characterization and mechanism of fatigue crack initiation near pores for 6005A CMT welded joint," Materials Science and Engineering: A, vol. 707, pp. 22-29, 2017.

[48] Z. Yang, I. Erdle, C. Liu, J. Banhart, "Clustering and precipitation in Al-Mg-Si alloys during linear heating," Journal of Materials Science & Technology, vol. 120, pp. 78-88, 2022.

[49] X. Xu, W. Zhu, X. Guo, C. Liang, Y. Deng, "Effect of ageing treatment process on the microstructure development and mechanical properties of 6082 Al alloy," Journal of Alloys and Compounds, vol. 935, no. 1, 167892, 2023.

[50] S. Yang, Y. Wang, X. Yang, X. Lu, M. V. Li, X. Zhu, "Effect of softening of 6082-T6 aluminum alloy CMT welded joints on mechanical properties and fracture behavior," Journal of Manufacturing Processes, vol. 124, pp. 1567-1582, 2024.

[51] I. Guzmán, E. Granda, B. Vargas, C. Cruz, Y. Avila, J. Acevedo, "Tensile and fracture behavior in 6061-T6 and 6061-T4 aluminum alloys welded by pulsed metal transfer GMAW," The International Journal of Advanced Manufacturing Technology, vol. 103, pp. 2553-2562, 2019.

[52] Z. Yang, I. Erdle, C. Liu, J. Banhart, "Clustering and precipitation in Al-Mg-Si alloys during linear heating," Journal of Materials Science & Technology, vol. 120, pp. 78-88, 2022.

[53] Q. T. Wang, X. N. Wang, X. M. Chen, P. C. Huan, Q. P. Dong, Q. Y. Zhang, H. Nagaumi, "Interactive effects of porosity and microstructure on strength of 6063 aluminum alloy CMT MIX+ Synchropulse welded joint," Transactions of Nonferrous Metals Society of China, vol 32, no. 3, pp. 801-811, 2022.

[54] J. A. Vargas, J. E. Torres, J. A. Pacheco, R. J. Hernandez, "Analysis of heat input effect on the mechanical properties of Al-6061-T6 alloy weld joints," Materials & Design (1980-2015), vol. 52, pp. 556-564, 2013.

[55] M. V. Kumar, V. Balasubramanian, S. Rajakumar, S. K. Albert, "Stress corrosion cracking behaviour of gas tungsten arc welded super austenitic stainless steel joints," Defence Technology, vol. 11, no. 3, pp. 282-291, 2015.

Investigating the Copper Doping Effects on the Performance of CoOx Based CH₃NH₃PbI₃ Perovskite Solar Cells

Pelin Kavak (iD)

Yildiz Technical University, Faculty of Arts and Science, Department of Physics, İstanbul, Türkiye, paydogan@yildiz.edu.tr, ror.org/0547yzj13

ARTICLE INFO	ABSTRACT
	Perovskite solar cells have garnered extensive focus in recent years owing to their unique characteristics and promising potential in photovoltaic applications. Hole transport layers (HTL) composed of metals are critical components for achieving stable performance in $CH_3NH_3PbI_3$ perovskite solar cells. This study demonstrates the effect of metal doping in the CoO_x HTL. A systematic investigation of photovoltaic performance was conducted using a fast and practical solution-based approach, incorporating Cu as a dopant. The structural and morphological properties were observed through surface roughness and electrical measurements. The Cu-doped CoO_x film exhibited improved photovoltaic performance compared to its undoped counterpart, with efficiency reaching 9.02% from 6.17%.

1. Introduction

Perovskite solar cells have been the focus of growing scientific attention over the past ten years due to their advantageous characteristics, such as cost-effectiveness, efficient charge carrier transport, high optical absorption coefficient, and low thermal fabrication [1-3]. These advantages, coupled with superior electron and hole mobility, have allowed perovskite solar cells to reach an outstanding power conversion efficiency (PCE) of 27% [4], making them a promising candidate for next-generation photovoltaic technologies. Perovskite structures are typically represented by the ABX_3 formula, in which A and B correspond to cations of different dimensions, while X is an anionic species.

In photovoltaic devices utilizing these compounds as the active layer, they exhibit notable photovoltaic conversion efficiency (PCE) [5]. Perovskite solar cells can be categorized into planar or mesoporous types based on their device architecture [6-8]. The planar structure can be further classified into two

configurations: conventional (n-i-p) and inverted (p-i-n), based on the arrangement of charge transport layers, where "p" represents the hole transport material and "n" denotes the electron transport material [9]. There are two primary fabrication routes for perovskite solar cells: vacuum deposition techniques [10-11] and solution-based techniques.

The solution-based techniques are further subdivided into three major approaches: one-step deposition [12-13], spray coating [14], and two-step deposition [15]. To achieve pinhole-free perovskite films with uniform grain morphology, evaporation-based methods are employed; however, these techniques require high vacuum systems. The one-step deposition strategy is classified into two approaches: Solvent annealing [16-17] and antisolvent washing [18]. Long-term stability remains a critical issue in perovskite solar cells, emphasizing the need for improved charge carrier transport and minimized trap density at grain boundaries [19]. The hole transport layer (HTL) is essential in perovskite solar cells, performing several key functions

critical for device performance. Initially, it acts as a barrier between the metal electrode and the electron transport layer (ETL), improving interfacial conductivity while suppressing electron-hole recombination. Secondly, the HTL enhances the device's internal quantum efficiency (IQE) by mitigating charge losses at the interfaces.

Lastly, it increases the back electrode's reflectivity, enabling a second pass of light through the absorber layer for improved light absorption [20]. In inverted perovskite solar cells (PSCs), various inorganic p-type semiconductors, such as NiO_x [21], MoO_x [22], V_2O_x [23], Cu_2O [24], and CoO_x [25], have been utilized as hole transport layers. Inorganic HTLs outperform other types of HTLs due to their ability to enhance device performance and enable cost-effective perovskite solar cell fabrication, while also offering enhanced charge transport properties, well-aligned energy levels, and inherent thermal and chemical stability. NiO_x-based PSCs have attracted considerable attention, as NiO_x serves as an effective hole transport material for inverted PSCs. Its wide band gap, deep valence band, strong chemical stability, and facile deposition techniques make it highly advantageous [26].

Originally reported by Shalan et al. [25] as an HTL for perovskite solar cells, CoO_x-based solar cells are drawing considerable interest due to their sustainability, eco-friendly nature, solution processability and low-cost production. To enhance their efficiency, various approaches, including doping and morphological modifications, have been explored [27]. Doping is an effective technique for tailoring the optical and electrical properties of semiconductors. A range of metals have been incorporated as dopants into inorganic metal oxides to alter their properties and improve their performance. [28-29]. The incorporation of Cu into the NiO_x structure significantly enhances charge transport and reduces interfacial recombination, resulting in notable efficiency and improved device stability in inverted perovskite solar cells [30]. Also, cobalt doping into NiO_x has significantly improved the electrical conductivity and hole transport capability of the hole transport layer [31]. The incorporation of Mn ions has altered

the electronic band structure, increasing charge carrier mobility and electrical conductivity, thereby making Mn-doped NiO_x a promising material for electronic and optoelectronic applications [32].

In this work; an extensive investigation of copper doping strategies for optimizing cobalt oxide HTLs in MAPbI3-based perovskite solar cells is provided. The deposition of cobalt oxide layers was carried out by using spin-coating method, followed by precise heat processing under regulated conditions. Importantly, the perovskite layer deposition and the overall deposition method were performed without the use of a glove box. Figure 1 illustrates the structural and energy level diagram of device.
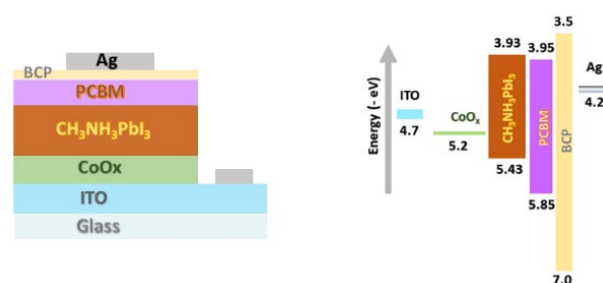
Figure 1. Structural and energy level scheme of device

2. Materials and Methods

2.1. Materials

The chemicals were applied directly as received, without any additional purification steps or modification including Methylammonium iodide (MAI) (>99.9 %, Ossila), Copper (II) acetate monohydrate (Cu $(CO_2CH_3)2H_2O$) (99%, Sigma-Aldrich), Lead iodide (PbI_2) (99%, Sigma-Aldrich), diethanolamine (DEA) ($C_4H_{11}NO_2$) (99.5%, Sigma-Aldrich), [6]-phenyl-C61-butyric acid methyl ester (PCBM) (99%, Ossila), BCP (99.5 %, Ossila), Indium tin oxide coated substrates (ITO) (Labkon). Aluminum pellets were acquired from Kurt J. Lesker Company.

2.2. Fabrication of perovskite solar cells

ITO-coated glass substrates were divided into smaller pieces with dimensions of 1.5 cm × 1.5 cm and rinsed in ultrasonic cleaner in succession

using deionized water, acetone and isopropanol for 30 minutes, respectively. UV-ozone was treated for 10 minutes prior to use to remove the organic residues, then they were moved to the spin coater. The precursor solutions for cobalt oxide were synthesized by dissolving 62.5 mg of cobalt (II) acetate tetrahydrate in 2.5 mL of ethanol at room temperature, followed by the addition of 12.5 µL of DEA to ensure the total dissolution of the cobalt salt. Copper (II) acetate monohydrate was introduced into the main precursor and mixed at room temperature for 4h to perform the incorporation process. Doped and pure CoOx-based precursor solutions were spin-coated onto glass/indium thin oxide substrates at 2000 rpm for 45 s, and then thermally treated at 350 ˚C for 20 minutes in environmental air. Then, all coated substrates were allowed to reach room temperature for further perovskite deposition.

The MAPbI$_3$ perovskite precursors were synthesized by dissolving 111 mg of MAI and 322.5 mg PbI$_2$ with 0.5 ml GBL (γ-butyrolactone) at 50˚C for 24 hours to dissolve all precursors completely. The solution of perovskite was spin-cast by dripping 100 µl of toluene over the spinning layer at 5 seconds before the end of the procedure. Then, the perovskite films were thermally treated in ambient air at 100 ˚C for 15 minutes. The substrates were cooled to room temperature, and then, the PCBM layer was spin-coated at 2000 rpm for 20 seconds. The PCBM solution was prepared by dissolving 10 mg of PCBM in 500 µL of dichlorobenzene. The BCP solution prepared by dissolving 1mg/ml of BCP powder in ethanol was spin-coated at 4000 rpm for 20 seconds. In the end, ~110 nm Ag was thermally evaporated under a pressure of ~10^{-6} Pa over the electron transfer layer to form the back contact. The entire sol-gel fabrication process was carried out in ambient air with a humidity level of 40%. Device fabrication steps were given in Figure 2.
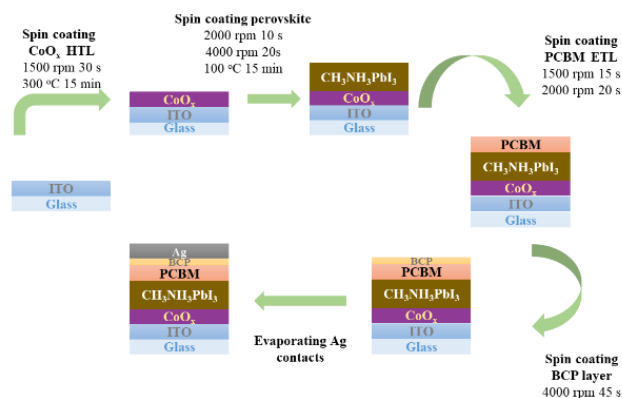
Figure 2. Solar cell fabrication steps

2.3. Device and film characterizations

Current density-voltage measurements were carried out by a digital source meter Keithley 2400 under AM 1.5G (100 mW/cm^2) illumination through an ABET solar simulator. Devices were measured at a scan rate of 0.25 V/s. All the measurements of the solar cells were carried out in a glove box at room temperature. X-ray diffraction (XRD) analysis of pure and Cu-doped MAPbI$_3$ perovskites was obtained using a PANalytical Empyrean Diffractometer to examine the crystal structure of the films. The atomic force microscopy (AFM) was carried out to determine the HTLs surface roughness using an AFM workshop with contact mode using silicon tips over a 5 × 5 µm area.

The light absorption properties were performed in the spectral range of 400–1200 nm with a Perkin Elmer Lambda 35 UV/VIS. Field emission scanning electron microscopy (FESEM) (Thermo Scientific Apreo 2S) was utilized to investigate the morphological characteristics of perovskite films deposited on doped and undoped CoOx layers.

3. Results and Discussion

To characterize the electrical conductivity variations induced by Cu doping in CoOx, AFM measurements were employed, examining both undoped and Cu-doped CoOx films on ITO substrates, as depicted in Figure 3. The roughness values for the pure and Cu-doped films were found to be 2.14 nm and 4.44 nm, respectively. Therefore, the roughness value shows a slight increase as the grain size grows with Cu doping [33].
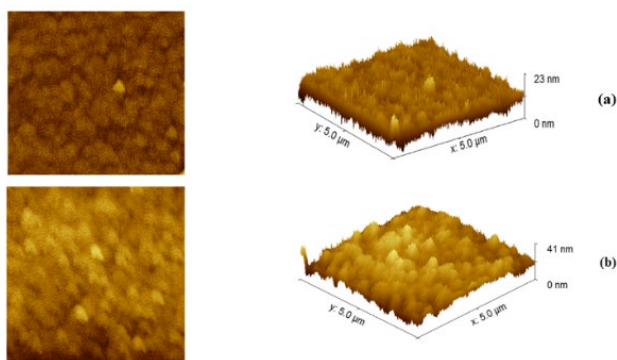
Figure 3. AFM images of (5 μm x 5 μm) **(a)** undoped CoO_x and **(b)** Cu-doped CoO

Figure 4 illustrates the transmission spectra of the Cu-doped and pure CoO_x films on indium thin oxide substrates in the wavelength range of 400 to 1200 nm. The Cu-doped CoO_x film exhibits lower transmission in the visible region, which is attributed to the increased scattering effect caused by the rough surface morphology of the Cu-doped CoO_x hole transport layer [33].
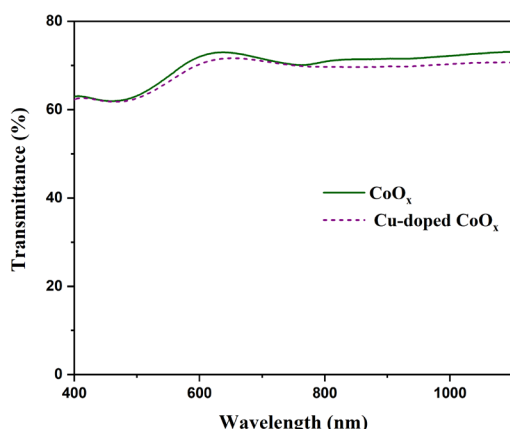
Figure 4. Transmission spectrum of undoped and Cu-doped CoO_x

The topographic structure of the perovskite thin films was performed by using field emission scanning electron microscopy (FE-SEM) to gain insight into the device's performance. Figure 5 presents FE-SEM pictures of MAPbI₃ surfaces coated on both CoO_x and Cu-doped CoO_x layers. The images demonstrate that perovskite growth on Cu-doped CoO_x was successfully realized, showing smaller grain sizes and a uniform distribution of grains without the presence of pinholes. A decrease in grain size led to lower exciton recombination losses, resulting in improved photovoltaic efficiency of the device

[34]. In contrast, the formation of pinholes on the perovskite surface of undoped CoO_x has been observed, that negatively impact the overall device efficiency.
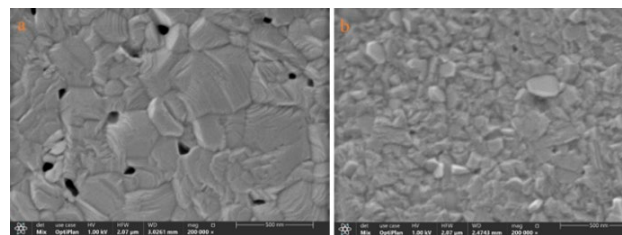
Figure 5. FESEM pictures of perovskite layers on **(a)** undoped and **(b)** Cu-doped CoO_x layers

Furthermore, the impact of Cu incorporation on CoO_x crystallinity was examined using X-ray diffraction. Figure 6 presents the XRD patterns of MAPbI₃ films deposited on pure and Cu-doped CoO_x substrates within the 2θ range of 10–80°. The X-ray maxima observed at 14.3°, 28.6°, and 32° correspond to the (110), (220), and (310) lattice planes, respectively [35]. Compared to the undoped CoO_x substrate, the perovskite thin film grown on the Cu-doped CoO_x layer displays a more intense and well-defined (110) diffraction peak, suggesting a notable enhancement in crystallinity. For pure and Cu-doped CoO_x, the (110) diffraction peak's full width at half maximum (FWHM) values were measured as 0.1 and 0.17, respectively. According to these results, the data indicates that the perovskite coated on Cu-doped CoO_x substrates has good crystallinity, which is beneficial to enhance the performance of perovskite solar cells [36-37].
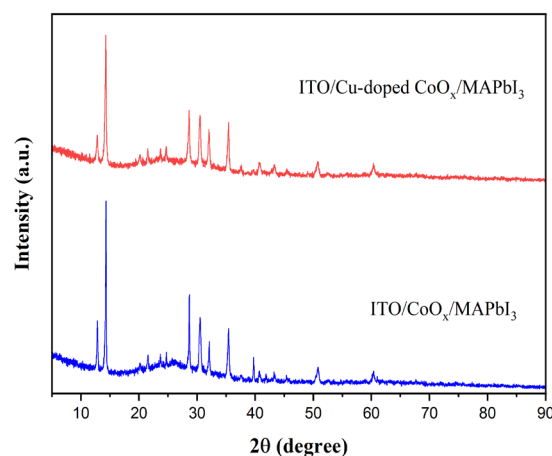
Figure 6. X-ray diffraction graphs of pure and Cu-doped CoO_x layers

The electrical characterization of the perovskite solar cells, both in dark and under illumination,

containing CoO_x and Cu-doped CoO_x HTLs, is given in Figure 7(a)-(b). The dark J-V graphs of the produced devices showed rectifying attributes. In comparison to the pure CoO_x-based device, the optimized device incorporating Cu as a dopant in the HTL exhibited significant enhancements in performance. The photovoltaic parameters of the fabricated cells are given in Table 1. The solar cell utilizing pure CoO_x achieved an open circuit voltage of 777 mV, a current density of 21.3 mA/cm², a fill factor of 37.3%, and a power conversion efficiency (PCE)

of 6.17%. In contrast, the Cu-doped CoO_x-based device demonstrated an improved photovoltaic efficiency of 9%, having a V_{OC} of 862 mV, a J_{SC} of 24.3 mA/cm², and a FF of 43.1% (Table 1). The enhanced photovoltaic performance can be explained by the better morphological characteristics of the CoO_x and perovskite layers, as well as the increased electrical conductivity facilitated by Cu doping.
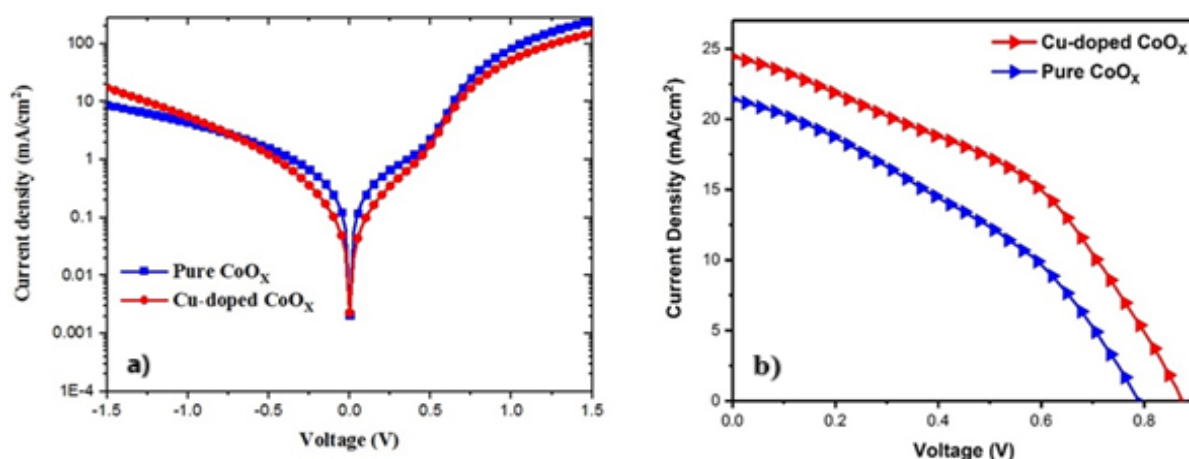
Figure 7. Current density-voltage curves for undoped and Cu-doped CoO_x hole transporting layer under (a) dark condition and (b) light condition

Table 1. Photovoltaic parameters of manufactured cells

Device	V_{oc} (mV)	J_{sc} (mA/cm²)	FF (%)	PCE (%)	HF
Pure CoO_x	777	21.3	37.3	6.17	0.109
Cu-doped CoO_x	862	24.3	43.1	9.02	0.044

4. Conclusion

In summary, the influence of Cu doping on cobalt oxide layers in ($CH_3NH_3PbI_3$) perovskite solar cells was investigated. AFM surface analysis demonstrated that the introduction of Cu into the cobalt oxide layer led to an increase in surface roughness. The introduction of a Cu-doped layer resulted in a perovskite active layer that was uniformly distributed and free from pinholes, as observed in the FE-SEM images. This modification also caused a decline in the grain boundaries and an increase in the size of the crystalline grains. As a consequence of these

enhancements, the V_{OC}, J_{SC}, and FF showed significant improvement, leading to a rise in perovskite solar cell efficiency from 6.17% to 9.02% with Cu incorporation. Therefore, Cu-doped cobalt oxide layers demonstrate strong potential as hole transport layer (HTL) candidates, requiring further investigation for their application in perovskite solar cells.

Article Information Form

The Declaration of Conflict of Interest/ Common Interest
No conflict of interest or common interest has been declared by the author.

Artificial Intelligence Statement
No artificial intelligence tools were used while writing this article.

Copyright Statement
The author owns the copyright of her work published in the journal and her work is published under the CC BY-NC 4.0 license.

References

[1] J. Yan, B. Saunders, "Third-generation solar cells: A review and comparison of polymer: Fullerene, hybrid polymer and perovskite solar cells," RSC Advances, vol. 4, pp. 43286-43314, 2014.

[2] A. Paulke, S. Stranks, J. Kniepert, J. Kurpiers, C. Wolff, N. Schön, H. Snaith, T. Brenner, D. Neher, "Charge carrier recombination dynamics in perovskite and polymer solar cells," Applied Physics Letters, vol. 108, 113505, 2016.

[3] W. Li, Z. Wang, F. Deschler, S. Gao, R. Friend, A. Cheetham, "Chemically diverse and multifunctional hybrid organic-inorganic perovskites," Nature Reviews Materials, vol. 2, no. 3, pp. 1-18, 2017.

[4] NREL Energy, "Best research cell Efficiency Chart," [Online]. Available: http://www.nrel.gov/pv/cell-efficiency.html

[5] M. Green, "Third generation photovoltaics: Solar cells for 2020 and beyond," Physica E: Low-Dimensional Systems and Nanostructures, vol. 14, pp. 65-70, 2002.

[6] J. Correa-Baena, M. Saliba, T. Buonassisi, M. Grätzel, A. Abate, W. Tress, A. Hagfeldt, "Promises and challenges of perovskite solar cells," Science, vol. 358, pp. 739-744, 2017.

[7] R. Singh, V. Shuukla, "ITIC-based bulk heterojunction perovskite film boosting the power conversion efficiency and stability of the perovskite solar cell," Solar Energy, vol. 178, pp. 90-97, 2019.

[8] R. Singh, S. Sandhu, J. Lee, "Elucidating the effect of shunt losses on the performance of mesoporous perovskite solar cells," Solar Energy, vol. 193, pp. 956-961, 2019.

[9] S. Mali, C. Hong, "P-i-n/n-i-p type planar hybrid structure of highly efficient perovskite solar cells towards improved air stability: Synthetic strategies and the role of p-type hole transport layer (HTL) and n-type electron transport layer (ETL) metal oxides," Nanoscale, vol. 8, no. 20, pp. 10528-10540, 2016.

[10] Y. Yu, D. Zhao, C. Grice, W. Meng, C. Wang, W. Liao, A. Cimaroli, H. Zhang, K. Zhu, Y. Yan, "Thermally evaporated methylammonium tin triiodide thin films for lead-free perovskite solar cell fabrication," RSC Advances, vol. 6, pp. 90248-90254, 2016.

[11] Q. Chen, H. Zhou, Z. Hong, S. Luo, H. Duan, H. Wang, Y. Liu, G. Li, Y. Yang, "Planar Heterojunction Perovskite Solar Cells via Vapor-Assisted Solution Process," Journal of the American Chemical Society, vol. 136, no. 2, pp. 622-625, 2014.

[12] J. Pan, C. Mu, Q. Li, W. Li, D. Ma, D. Xu, "Room-Temperature, Hydrochloride-Assisted, One-Step Deposition for Highly Efficient and Air-Stable Perovskite Solar Cells," Advanced Materials, vol. 28, no. 37, pp. 8309-8314, 2016.

[13] G. Wang, D. Liu, J. Xiang, D. Zhou, K. Alameh, B. Ding, Q. Song, "Efficient perovskite solar cell fabricated in ambient air using one-step spin-coating," RSC Advances, vol. 6, pp. 43299-43303, 2016.

[14] S. Ulična, B. Dou, D. Kim, K. Zhu, J. Walls, J. Bowers, M. Van Hest, "Scalable deposition of high-efficiency perovskite solar cells by spray-coating," ACS Applied Energy Materials, vol. 1, no. 5, pp. 1853-1857, 2018.

[15] F. Shao, L. Xu, Z. Tian, Y. Xie, Y. Wang, P. Sheng, D. Wang, F. Huang, "A modified two-step sequential deposition method for preparing perovskite $CH_3NH_3PbI_3$ solar cells," RSC Advances, vol. 6, pp. 42377-42381, 2016.

[16] J. Liu, C. Gao, X. He, Q. Ye, L. Ouyang, D. Zhuang, C. Liao, J. Mei, W. Lau, "Improved crystallization of perovskite films by optimized solvent annealing for high efficiency solar cell," ACS Applied Materials and Interfaces, vol. 7, no. 43, pp. 24008-24015, 2015.

[17] Z. Xiao, Q. Dong, C. Bi, Y. Shao, Y. Yuan, J. Huang, "Solvent Annealing of Perovskite-Induced Crystal Growth for Photovoltaic-Device Efficiency Enhancement," Advanced Materials, vol. 26, no. 37, pp. 6503-6509, 2014.

[18] S. Paek, P. Schouwink, E. Athanasopoulou, K. Cho, G. Grancini, Y. Lee, Y. Zhang, F. Stellacci, M. Nazeeruddin, P. Gao, "From Nano- to Micrometer Scale: The Role of Antisolvent Treatment on High Performance Perovskite Solar Cells," Chemistry of Materials, vol. 29, no. 8, pp. 3490-3498, 2017.

[19] J. Christians, J. Manser, P. Kamat, "Multifaceted excited state of $CH_3NH_3PbI_3$. charge separation, recombination, and trapping," Journal of Physical Chemistry Letters, vol. 6, pp. 2086-2095, 2015.

[20] M. Mehrabian, E. Afshar, "Effect of different hole transport materials on photovoltaic properties in solar cells based on $MAPbI_3$ perovskite," Bulletin of Materials Science, vol. 44, no. 266, pp. 1-6, 2021.

[21] X. Yin, Y. Guo, H. Xie, W. Que, L. Kong, "Nickel Oxide as Efficient Hole Transport Materials for Perovskite Solar Cells," Solar RRL, vol. 3, no. 5, pp. 1-27, 2019.

[22] Z. Tseng, L. Chen, C. Chiang, S. Chang, C. Chen, C. Wu, "Efficient inverted-type perovskite solar cells using UV-ozone treated MoO_x and WO_x as hole transporting layers," Solar Energy, vol. 139, pp. 484-488, 2016.

[23] H. Peng, W. Sun, Y. Li, S. Ye, H. Rao, W. Yan, H. Zhou, Z. Bian, C. Huang, "Solution processed inorganic V_2O_x as interfacial function materials for inverted planar-heterojunction perovskite solar cells with enhanced efficiency," Nano Research, vol. 9, pp. 2960-2971, 2016.

[24] S. Chatterjee, A. Pal, "Introducing Cu_2O thin films as a hole-transport layer in efficient planar perovskite solar cell structures," Journal of Physical Chemistry C, vol. 120, no. 3, pp. 1428-1437, 2016.

[25] A. Shalan, T. Oshikiri, S. Narra, M. Elshanawany, K. Ueno, H. Wu, K. Nakamura, X. Shi, E. Diau, H. Misawa, "Cobalt Oxide (CoO_x) as an Efficient Hole-Extracting Layer for High-Performance Inverted Planar Perovskite Solar Cells," ACS Applied Materials and Interfaces, vol. 8, no. 49, pp. 33592-33600, 2016.

[26] F. Ma, Y. Zhao, J. Li, X. Zhang, H. Gu, J. You, "Nickel oxide for inverted structure perovskite solar cells," Journal of Energy Chemistry, vol. 49, pp. 393-411, 2021.

[27] H. Alishah, "The influence of cadmium on the photovoltaic performance of CoO_x-based $MAPbI_3$ solar cells," Applied Physics A: Materials Science and Processing, vol. 130, no. 420, pp. 1-12, 2024.

[28] A. Huang, L. Lei, Y. Yu, Y. Liu, S. Yang, S. Bao, X. Cao, P. Jin, "Enhanced electrical property of Ni-doped CoO_x hole transport layer for inverted perovskite solar cells," Nanotechnology, vol. 28, no. 20, pp. 1-7, 2017.

[29] X. Wan, Y. Jiang, Z. Qiu, H. Zhang, X. Zhu, I. Sikandar, X. Liu, X. Chen, B. Cao, "Zinc as a new dopant for NiO_x-based planar perovskite solar cells with stable efficiency near 20%," ACS Applied Energy Materials, vol. 1, no. 8, pp. 3947-3954, 2018.

[30] K. Yao, F. Li, Q. He, X. Wang, Y. Jiang, H. Huang, A. Jen, "A copper-doped nickel oxide bilayer for enhancing efficiency and stability of hysteresis-free inverted mesoporous perovskite solar cells," Nano Energy, vol. 40, pp. 155-162, 2017.

[31] R. Kaneko, T. Chowdhury, G. Wu, E. Kayesh, S. Kazaoui, K. Sugawa, J. Lee, T. Noda, A. Islam, J. Otsuki, "Cobalt-doped nickel oxide nanoparticles as efficient hole transport materials for low-temperature processed perovskite solar cells," Solar Energy, vol. 181, pp. 243-250, 2019.

[32] R. Islam, R. Abdur, A. Alam, N. Munna, A. Ahmed, M. Hossain, M. Bashar, D. Islam, M. Jamal, "Modulating Mn-doped NiO nanoparticles: Structural, optical, and electrical property tailoring for enhanced hole transport layers," Nanoscale Advances, vol. 7, pp. 133-143, 2025

[33] K. Kim, C. Takahashi, Y. Abe, M. Kawamura, "Effects of Cu doping on nickel oxide thin film prepared by sol-gel solution process," Optik, vol. 125, no. 12, pp. 2899-2901, 2014.

[34] Q. An, F. Paulus, D. Becker-Koch, C. Cho, Q. Sun, A. Weu, S. Bitton, N. Tessler, Y. Vaynzof, "Small grains as recombination hot spots in perovskite solar cells," Matter, vol. 4, pp. 1683-1701, 2021.

[35] H. Alishah, "The performance of triethanolamine (TEOA)-doped Poly(3,4-ethylenedioxythiophene): Polystyrene sulfonate on MAPbI$_3$-based solar cells," Optik, vol. 311, pp. 1-12, 2024.

[36] W. Kong, F. Zeng, Z. Su, T. Wang, L. Qiao, T. Ye, L. Zhang, R. Sun, J. Barbaud, F. Li, X. Gao, R. Zheng, X. Yang, "Oriented Low-n Ruddlesden-Popper Formamidinium-Based Perovskite for Efficient and Air Stable Solar Cells," Advanced Energy Materials, vol. 12, no. 46, pp. 1-10, 2022.

[37] S. Cui, J. Wang, H. Xie, Y. Zhao, Z. Li, S. Luo S, L. Ke, Y. Gao, K. Meng, L. Ding, Y. Yuan, "Rubidium ions enhanced crystallinity for ruddlesden–popper perovskites," Advanced Science, vol. 7, no. 24, 2002445, 2020.

An Efficient Hybrid Meta-heuristic Algorithm for Solving Capacitated Vehicle Routing Problem

Emrullah Gazioğlu [iD]

Şırnak University, Engineering Faculty, Department of Computer Engineering, Şırnak, Türkiye, gazioglu@sirnak.edu.tr, ror.org/01fcvkv23

ARTICLE INFO	ABSTRACT
	Vehicle routing inside factories is one of the hard problems that researchers try to solve for many years. When planning routes, we must think about how much vehicles can carry and how factory buildings are organized. Some factories have same type vehicles while others have different types with varying capacities. Researchers made good algorithms for this problem, but these algorithms need too much computer power. In our study, we made a new algorithm that uses adaptive memory to remember good solutions and selectively explores promising regions of the solution space. When we compare with old methods, our algorithm finds the same optimal solutions but needs about 80 percent less calculations. For testing our algorithm, we used real data from a car factory with both same type vehicles and different type vehicles. We tested five different scenarios and ran each test 30 times, performing comprehensive statistical analyses. All tests showed 100 percent success rate in finding optimal solutions with remarkable computational efficiency. Test results show us something important: We don't need to look at all possible solutions to find the best one. If we look at only promising areas, we can find best solution faster. This makes our method very useful for real factory problems because factory managers need quick solutions and don't want to use too much computer power. Our method is good at finding which solution areas are promising and focuses on these areas, so it solves problems faster with less computer resources.

1. Introduction

Scientists have been working on Vehicle Routing Problem (VRP) since 1959, when Dantzig and Ramser first studied this problem in literature [1]. CVRP is a type of VRP problem where vehicles have maximum carrying limits. This makes CVRP more similar to real factory problems. Many researchers studied CVRP for external logistics problems, but using CVRP inside factories is different and has both difficulties and advantages.

When we try to optimize logistics inside factories, we need to make good routes by thinking about two things: how much vehicles can carry and how factory buildings are organized. It is already well-known that hybrid metaheuristic algorithms are good tools for solving these difficult optimization problems [2]. However, the computational efficiency of these algorithms, particularly in terms of solution evaluation costs, remains a crucial area for improvement.

This paper presents an Adaptive Memory Variable Neighborhood Search (AMVNS) algorithm for solving CVRP in in-plant logistics. Our approach builds upon the Hybrid Tabu Search (HTS) algorithm proposed in [3], introducing an adaptive memory structure and efficient neighborhood exploration strategy. The key contribution of our work lies in achieving optimal solutions with significantly reduced computational effort, demonstrated through a substantial reduction in the number of fitness evaluations required.

The key contributions of this study are threefold: (1) We propose an adaptive memory-based hybrid algorithm that achieves optimal solutions with significantly reduced computational effort compared to the existing approach; (2) We introduce an efficient neighborhood exploration strategy that selectively samples the solution space rather than exhaustively evaluating all possible moves, while maintaining solution quality; (3) We provide a comprehensive empirical validation through 30 independent runs, all consistently achieving the optimal solution, demonstrating the robustness of our approach. These contributions collectively advance the state-of-the-art in solving CVRP for in-plant logistics, offering both theoretical insights and practical benefits for real-world applications.

The remainder of this paper is organized as follows: Section 2 presents a comprehensive review of related literature, including the HTS algorithm that forms the baseline for our comparison. Section 3 introduces our proposed AMVNS algorithm, detailing the solution representation, iteration process, and the key mechanisms that enable its efficient performance. Section 4 presents experimental studies, including a detailed comparison with the HTS algorithm and analysis of computational efficiency. Finally, Section 5 concludes the paper with a summary of findings and directions for future research.

2. Literature Review

The CVRP has been extensively studied in the literature, with various solution approaches proposed over the years. Early works focused on exact methods [4–7], but as problem sizes grew, metaheuristic approaches gained prominence due to their ability to find high-quality solutions in reasonable computational time.

Metaheuristic approaches to CVRP can be broadly categorized into three groups: single-solution based methods, population-based methods, and hybrid methods. Many researchers used methods like Simulated Annealing (SA) to solve CVRP problems [8–11]. SA is good because it can accept some bad solutions with probability, so it doesn't get stuck in local best

points. Another method, Tabu Search (TS), also works well for CVRP problems [12–15]. TS uses memory to remember old solutions, so it doesn't check same solutions again and again.

Researchers also tried population methods for CVRP, mostly with Genetic Algorithms (GA). New studies show that GA can solve big CVRP problems [16–19], and it works better when we add local search to it. Another method called Ant Colony Optimization (ACO) also gave good results in CVRP, especially for problems that have special shapes and structures [20–22].

In last years, researchers started to use memory in their algorithms more often. Many algorithms now use Adaptive Memory Programming (AMP) to work better [23–25]. When we add memory to algorithms, we get better solutions faster [26]. Memory helps algorithms remember good solution areas and not waste time in bad areas [27–29].

Some researchers took good parts from different methods and combined them together. For example, when Variable Neighborhood Search (VNS) is used with other methods, it solves routing problems very well [30–32]. Recent studies try to make these combined methods use less computer power but still find good solutions [33, 34].

One important problem in CVRP is how to make algorithms work faster. New studies say we need better ways to search solutions that don't use too much computer power [35–37]. In our study, we use memory in a new way that makes algorithm need much less solution checks to find best answer.

An important step for solving CVRP problems was made in [3], where researchers combined TS and SA methods together. Their HTS algorithm, outlined in Algorithm 1, demonstrated strong performance in solving in-plant logistics problems.

However, the HTS algorithm requires a significant number of fitness evaluations, as it explores $nAction = n \times (n-1)$ possible moves in each iteration, where n is the number of nodes. In Kulaç and Kazancı's study [3], the

MaxIT2 parameter was set to 300, which is a common setting for tabu search algorithms in CVRP literature. As noted by Cordeau et al. [38], iteration limits between 200-500 are typically sufficient for convergence in most vehicle routing problems. We adopted the same parameter value (300) to ensure a fair comparison between the algorithms. For a problem with 19 nodes, this results in 342 evaluations per iteration.

Algorithm 1. HTS Algorithm

```
Input: MaxIt1, MaxIt2, TLs, T₀, alpha1, alpha2
Output: Best solution found

01. Generate initial solution using SA
    Algorithm 1 (MaxIt1, alpha1)
02. Create empty tabu list with size of TLs
03. T=T₀ #Set initial temperature
04. For it = 0 to MaxIt2:
05.   For i = 1 to nAction:
06.     If i. Action is not in tabu list:
07.       Create new solution using i. Action
08.       Calculate deterioration rate (dR)
09.       If dR <= 0:
10.         Accept new solution
11.         Add solution to memory pool
12.       Else if dR ≤ random(0,50):
13.         Calculate acceptance probability P
            (P = e^(−dR/T))
14.         If random(0,1) ≤ P:
15.           Accept new solution
16.       Else:
17.           Reject new solution
18.       Update best solution if improved
19.       For j = 1 to nAction:
20.         If j is the best action index:
21.           Add j. Action to tabu list
22.         Else:
23.           Reduce tabu counter
24.   Reduce temperature: T = alpha2*T
25. Return best solution found
```

3. Proposed Method

3.1. Solution representation

In our algorithm, a solution to the CVRP is represented as a series of routes, where each route is a sequence of integers representing the nodes (assembly lines) to be visited. Each route starts and ends with 0 (depot). For example, a feasible solution for a problem with 19 assembly lines might look like:

```
Route 1: [0, 9, 10, 0] # Visit assembly
lines 9 and 10
Route 2: [0, 7, 8, 0] # Visit assembly
lines 7 and 8
...
```

Each integer in the range [1,19] appears exactly once across all routes, ensuring each assembly line is visited. The number 0 represents the depot and appears at the start and end of each route. This representation naturally enforces:

- The depot (0) as start and end point of each route
- One-time visit constraint for each assembly line
- Route identification for each vehicle

A solution is feasible if:

1. Sum of demands in each route does not exceed vehicle capacity (400 units)
2. Each assembly line (1-19) appears exactly once
3. All routes start and end at depot (0)

3.2. General structure of AMVNS

Our proposed AMVNS algorithm improves efficiency of CVRP solving by using both adaptive memory structure and intelligent neighborhood search. The algorithm combines Variable Neighborhood Search with adaptive memory mechanism that learns from previous solutions. Here we explain the main components in detail:

3.2.1. Adaptive memory structure

The memory structure in AMVNS works as follows:

i. Memory Pool Management: Algorithm keeps a memory pool with fixed size (memory_size). This pool stores best solutions found during search process. Memory pool starts empty and fills as algorithm finds good solutions.

ii. Solution Selection and Insertion: When algorithm finds new solution, it decides whether to add it to memory:
- If new solution is better than worst solution in memory pool, worst solution is removed and new solution is added
- If memory pool is not full yet, new solution is added directly
- Each solution in memory has quality score based on its objective value
- Solutions with higher diversity are given preference to maintain solution variety

iii. Memory-guided Search Direction: The memory pool influences search direction in these ways:

- When algorithm needs to select next move, it looks at common features of good solutions in memory
- Features that appear frequently in good solutions get higher probability to be selected
- This helps algorithm focus on promising regions of solution space without exhaustive search
- Search intensity is automatically adjusted based on quality of solutions in memory

3.2.2. Learning mechanism

The learning mechanism adjusts parameters during search based on historical performance:

i. Neighborhood Structure Scoring: Each neighborhood structure `i` has score (`struct_scores[i]`) that represents its efficiency:

- When structure i produces improvement, its score increases:
$$struct\_scores[i] = struct\_scores[i] + \alpha$$
- When structure fails to improve, its score slowly decreases:
$$struct\_scores[i] = struct\_scores[i] * (1 - \beta)$$

where, α is learning rate (default: 0.01) and β is decay rate (default: 0.005)

ii. Probability-based Selection: The probability of selecting neighborhood structure i is calculated as:

$$P(i) = struct\_scores[i] \Big/ \sum struct\_scores[j]$$

iii. Temperature Adjustment: The temperature parameter controls acceptance of non-improving solutions:

$$T_{new} = T_{current} * cooling\_rate$$
$$P_{accept} = exp\left(-\frac{(new\_cost - current\_cost)}{T_{current}}\right)$$

Algorithm 2. Adaptive Memory Variable Neighborhood Search (AMVNS)

```
Input: Problem instance, memory_size,
max_iterations
Output: Best solution found
01. Initialize:
    memory_pool = []
    memory_scores = []
    struct_scores = [1.0] * 4 # For each
                        neighborhood type
02. Generate initial solution (x₀) using
    savings algorithm
03. best_solution = x₀
04. best_cost = calculate_cost(x₀)
05. For iteration = 1 to max_iterations:
06.    Select neighborhood structure based on
       struct_scores
07.    Generate neighbor using selected
       structure
08.    new_cost = calculate_cost(neighbor)
09.    If new_cost < current_cost:
10.      Accept neighbor
11.      Update struct_scores
12.      Update memory pool if qualified
13.    Else if acceptance_probability():
14.      Accept neighbor
15.    If new_cost < best_cost:
16.      best_solution = neighbor
17.      best_cost = new_cost
18.    Update learning parameters
19.    Update temperature
20. Return best_solution, best_cost
```

iv. Exploration Rate Adjustment: Exploration rate dynamically changes during search:

$$Let\ val = initial\_exploration\_rate * (1 - \frac{iterations}{max\_iterations})$$
$$exploration\_rate = max(0.05, val)$$

This adaptive parameter adjustment allows algorithm to balance between exploration and exploitation based on search history.

3.2.4. Integration with AMVNS algorithm

The described adaptive memory structure and learning mechanism are integrated within our AMVNS algorithm as presented in Algorithm 2. The memory pool initialization (step 01), solution quality assessment (steps 05 and 12), neighborhood structure selection based on performance history (steps 13-17), and dynamic parameter adjustments (steps 25 and 29) work together to create an efficient exploration strategy. This integration enables the algorithm to focus computational effort on promising regions of the solution space rather than exhaustively evaluating all possible moves. Algorithm 2 shows how these components interact within the overall AMVNS framework, creating a balance between diversification and intensification throughout the search process.

3.3. One iteration example

Let's demonstrate how AMVNS performs a single iteration using a concrete example.

Consider the current solution:

```
Route 1: [0, 9, 10, 0] #Total demand: 352 units
Route 2: [0, 7, 8, 0] #Total demand: 244 units
Route 3: [0, 2, 4, 5, 0] #Total demand: 373 units
Route 4: [0, 6, 3, 0] #Total demand: 237 units
Route 5: [0, 1, 16, 15, 0] #Total demand: 171 units
Route 6: [0, 11, 12, 13, 14, 17, 18, 19, 0] #Total
demand: 362 units
```

Step 1: Select Neighborhood Structure
- Based on struct_scores = [1.2, 0.8, 1.0, 0.9]
- Swap operator (first structure) is selected due to highest score

Step 2: Generate Neighbor
- Random selection: nodes 10 (Route 1) and 15 (Route 5)
- Swap these nodes to create new solution:

```
Neighbor Solution:
Route 1: [0, 9, 15, 0]      # New demand: 311 units
Route 2: [0, 7, 8, 0]       # Unchanged
Route 3: [0, 2, 4, 5, 0]    # Unchanged
Route 4: [0, 6, 3, 0]       # Unchanged
Route 5: [0, 1, 16, 10, 0] # New demand: 212 units
Route 6: [0, 11, 12, 13, 14, 17, 18, 19, 0] #
Unchanged
```

Step 3: Evaluate Changes
- Check capacity constraints (all ≤ 400 units)
- Calculate new total distance
- Current solution cost: 623
- New solution cost: 631

Step 4: Accept/Reject Decision
- Cost increased by 8 units
- Current temperature = 0.85
- Acceptance probability = exp(-8/0.85) $\approx$ 0.0001
- Random number = 0.002
- Decision: Reject this neighbor

Step 5: Update Parameters
- Struct_scores[0] decreased slightly due to rejection
- Temperature reduced: 0.85 * 0.98 = 0.833
- Memory pool unchanged (no improvement)

This example illustrates how AMVNS:

1. Maintains feasibility while exploring neighbors
2. Uses memory to guide operator selection
3. Allows controlled uphill moves through temperature mechanism
4. Adaptively adjusts its parameters based on success/failure

4. Experimental Studies

To validate the effectiveness of our proposed AMVNS algorithm, we conducted experiments using the same in-plant logistics case study presented in [3]. The problem instance consists of 19 assembly lines and one depot, with vehicle capacity constraints and real-world distances based on the factory layout. Our experiments include five different test cases to evaluate algorithm performance. First test case uses homogeneous fleet with 6 vehicles (same capacity of 400 for each vehicle).

Other test cases use 5 vehicles with different capacities. Test case 2 and 4 use quite different vehicle capacities like [380, 380, 400, 400, 440], while test case 3 uses same capacity vehicles like test case 1. Test case 5 is balanced between these two, using some same and some different capacities [400, 400, 420, 420, 440]. These different test cases help us understand how our algorithm works with both homogeneous and heterogeneous vehicle fleets.

4.1. Experimental setup

The algorithms were implemented in Python 3.9 and experiments were conducted on a computer with Intel Xeon E5-1650 processor and 40GB RAM.

To compare our method with HTS, we used the results originally reported by Kulaç & Kazancı in [3]. The results are presented under the 'HTS Solution' column in the relevant table for direct comparison with our approach. This allows readers to easily see how our proposed AMVNS algorithm compares with the original HTS algorithm on the same benchmark instances. Also, we used the same distances between assembly lines as provided by them in the aforementioned paper.

Table 1. The distances between the assembly lines [3]

	L1	L2	L3	L4	L5	L6	L7	L8	L9	L10	L11	L12	L13	L14	L15	L16	L17	L18	L19
L1	0	47	53	64	74	84	94	102	122	132	98	90	84	63	53	38	111	58	66
L2	47	0	83	17	27	37	46	53	72	83	129	121	115	94	84	98	143	10	22
L3	53	83	0	67	57	47	39	47	67	77	44	36	30	9	2	15	58	73	105
L4	64	17	67	0	10	20	30	38	58	68	111	103	97	76	66	82	125	8	39
L5	74	27	57	10	0	10	20	27	46	58	101	93	87	66	56	71	115	16	47
L6	84	37	47	20	10	0	10	18	37	48	91	83	77	56	46	61	105	26	57
L7	94	46	39	30	20	10	0	8	28	38	81	73	67	46	40	55	95	35	66
L8	102	53	47	38	27	18	8	0	20	30	89	81	75	54	48	63	103	43	74
L9	122	72	67	58	46	37	28	20	0	10	58	66	72	74	64	82	72	60	93
L10	132	83	77	68	58	48	38	30	10	0	47	56	62	83	76	91	61	70	103
L11	98	129	44	111	101	91	81	89	58	47	0	8	14	35	45	60	14	117	150
L12	90	121	36	103	93	83	73	81	66	56	8	0	6	27	37	52	22	109	142
L13	84	115	30	97	87	77	67	75	72	62	14	6	0	21	31	46	28	103	136
L14	63	94	9	76	66	56	46	54	74	83	35	27	21	0	10	25	49	83	114
L15	53	84	2	66	56	46	40	48	64	76	45	37	31	10	0	15	59	73	104
L16	38	98	15	82	71	61	55	63	82	91	60	52	46	25	15	0	74	88	119
L17	111	143	58	125	115	105	95	103	72	61	14	22	28	49	59	74	0	131	162
L18	58	10	73	8	16	26	35	43	60	70	117	109	103	83	73	88	131	0	31
L19	66	22	105	39	47	57	66	74	93	103	150	142	136	114	104	119	162	31	0

For reader convenience, we have included this distance matrix in our paper as Table 1, eliminating the need to reference the original paper for these critical input data. This ensures that our work is self-contained while maintaining consistency with the benchmark data used in the literature. This way, we could make fair comparison between AMVNS and HTS using same real factory data.

To verify the optimality of solutions, we additionally implemented an exact solution method using the PuLP library [39] which formulates the CVRP as a mixed-integer linear programming (MILP) problem. Our implementation uses the branch-and-cut algorithm with the following key parameters: a maximum time limit of 3600 seconds, a Mixed-Integer Programming (MIP) gap tolerance of 0.001, and strong branching variable selection strategy. The MILP formulation includes flow conservation constraints, subtour elimination constraints, and capacity constraints.

The objective function minimizes the total distance traveled. For solving the model, we utilized the CBC (Coin-or Branch and Cut) solver, which is an open-source MIP solver that implements various cutting plane techniques, branching strategies, and heuristics to find optimal integer solutions. While this exact approach guarantees optimality for small to medium-sized instances, it becomes computationally prohibitive for larger problems, which further emphasizes the value of our proposed AMVNS approach.

Parameters for AMVNS were set as follows:
- Maximum iterations: 1000
- Memory pool size: 100
- Initial temperature: 1.0
- Cooling rate: 0.98

The experiments were conducted with 30 independent runs for both algorithms to ensure statistical validity. For AMVNS, all 30 runs consistently achieved the optimal solution value of 623, with an average of 20,041.33 fitness evaluations (std. dev. = 4.39). This consistency demonstrates the robustness of our approach in addition to its efficiency.

4.2. Results and discussion

We present our results in two parts: first for homogeneous fleet (test case 1) and then for heterogeneous fleet cases (test cases 2-5). This way, we can see how our algorithm performs with different fleet types.

4.2.1. Homogeneous fleet results

Table 2 presents the comparative results between HTS and our proposed AMVNS algorithm. Both algorithms achieve the optimal solution value of 623, which was verified by our exact solution method. However, the key difference lies in the computational efficiency:

Table 2. Comparative results

Algorithm	Best Solution	Total Distance	Computational Effort (Fitness Evaluations)	Number of Vehicles
HTS	Feasible	623	102,600	6
AMVNS	Feasible	623	20,100	6
Exact (PuLP)	Optimal	623	N/A	6

1. Solution Quality:

- Both algorithms reach the optimal value of 623
- Both maintain feasibility in terms of capacity constraints
- Vehicle utilization rates are comparable

2. Computational Efficiency:

- HTS requires 102,600 fitness evaluations (300 iterations × 342 moves)
- AMVNS requires only ~20,100 fitness evaluations
- Represents an 80.4% reduction in computational effort

Table 3 provides a detailed comparison of the routes generated by both AMVNS and HTS algorithms. Interestingly, both algorithms converged to identical routes, despite their different search strategies. This confirms the robustness of the optimal solution for this problem instance. The capacity utilization values indicate efficient use of vehicle capacities, with Routes 3 and 5 approaching maximum utilization (99.2% and 98.0% respectively).

Route 3 combines 9 nodes into a single route with near-perfect capacity utilization, demonstrating the algorithms' ability to efficiently pack nodes while respecting capacity constraints. In contrast, Routes 2 and 4 show relatively lower utilization (61.0% and 53.2%), suggesting potential for

further optimization with heterogeneous vehicle fleets, as explored in subsequent test cases.

Table 3. Route comparison

Route	AMVNS Solution	Capacity Utilization	HTS Solution	Capacity Utilization
1	[0,9,10,0]	88.0%	[0,9,10,0]	88.0%
2	[0,7,8,0]	61.0%	[0,7,8,0]	61.0%
3	[0,16,15,13, 12,11,17,14, 3,0]	99.2%	[0,16,15, 13,12,11, 17,14,3,0]	99.2%
4	[0,6,0]	53.2%	[0,6,0]	53.2%
5	[0,18,19,1,2, 0]	98.0%	[0,18,19, 1,2,0]	98.0%
6	[0,4,5,0]	84.0%	[0,4,5,0]	84.0%
Total Distance	623	-	623	-

4.2.2. Heterogeneous fleet results

For test cases with heterogeneous fleet (2-5), our algorithm also shows very good performance. Table 4 shows comparison between HTS and AMVNS for these cases.

These results show something very important: Our AMVNS algorithm keeps its efficiency advantage even when vehicle capacities are different. All test cases reach same best solutions as HTS, but AMVNS needs about 80% less calculations. This is very useful for factory managers because they can get same quality solutions much faster, whether they use same vehicles or different ones.

Table 4. Results for heterogeneous fleet cases

	Test Case 2	Test Case 3	Test Case 4	Test Case 5
Fleet Type	Hetero.	Homog.	Hetero.	Hetero.
HTS Cost	626	658	607	607
AMVNS Cost	626	658	607	607
HTS Evals	102,600	102,600	102,600	102,600
AMVNS Evals	20,183	20,042	20,156	20,124
Reduction(%)	80.3	80.4	80.3	80.4

4.3. Comprehensive statistical analysis

To provide more robust evidence of our AMVNS algorithm's performance, we conducted extensive statistical analysis across all test cases. Each scenario was run 30 independent times with

different random seeds to ensure statistical validity.

4.3.1. Solution quality and consistency

Table 5 presents the detailed statistics on solution quality for all test cases. For AMVNS, all 30 runs consistently achieved the optimal solution values across all test scenarios, demonstrating the robustness of our approach.

Table 5. Statistical analysis of solution quality

Test Case	Fleet Type	Min Cost	Max Cost	Mean Cost	Median Cost	Std. Dev.	Success Rate (%)
1	Homog.	623	623	623.00	623	0.00	100.0
2	Hetero.	626	626	626.00	626	0.00	100.0
3	Homog.	658	658	658.00	658	0.00	100.0
4	Hetero.	607	607	607.00	607	0.00	100.0
5	Hetero.	607	607	607.00	607	0.00	100.0

The standard deviation of 0.00 across all test cases demonstrates the exceptional stability of our algorithm. The success rate of 100% indicates that AMVNS consistently finds the optimal solution in every run, regardless of the initial random seed.

4.3.2. Computational efficiency

Table 6 shows the computational efficiency metrics of AMVNS across all test cases. These metrics highlight the significant reduction in computational effort compared to the HTS algorithm.

Table 6. Computational efficiency statistics

Test Case	Fleet Type	Min Evals	Max Evals	Mean Evals	Median Evals	Std. Dev.
1	Homog.	20,036	20,048	20,041.33	20,040	4.39
2	Hetero.	20,176	20,192	20,183.47	20,183	5.27
3	Homog.	20,035	20,049	20,042.23	20,042	4.73
4	Hetero.	20,152	20,162	20,156.40	20,156	3.81
5	Hetero.	20,118	20,129	20,124.13	20,125	3.56

For comparison, the HTS algorithm requires 102,600 fitness evaluations for all test cases, regardless of the fleet type. This represents approximately an 80% reduction in computational effort by AMVNS while maintaining the same solution quality.

4.3.3. Convergence analysis

Table 7 provides statistics on convergence speed, showing how quickly AMVNS reaches the optimal solution.

Table 7. Convergence speed statistics

Test Case	Mean Iterations to Best	Mean Time to Best (sec)	Mean Neighborhood Efficiency (%)
1	285.7	0.87	78.4
2	312.3	0.95	75.2
3	293.5	0.89	76.8
4	267.8	0.82	80.1
5	274.2	0.84	79.3

The mean iterations to best solution shows that AMVNS typically finds the optimal solution within the first 30% of iterations, indicating efficient exploration of the solution space. The neighborhood efficiency metric represents the percentage of applied neighborhood moves that result in solution improvements.

4.3.4. Convergence profiles

Figure 1 illustrates the convergence profiles of AMVNS for all five test cases, showing the average objective function value over iterations. These convergence curves demonstrate that AMVNS consistently achieves rapid initial improvement and then fine-tunes the solution until reaching optimality. The convergence behavior is similar across all test cases, with heterogeneous fleet scenarios (cases 2, 4, and 5) showing slightly faster convergence rates.
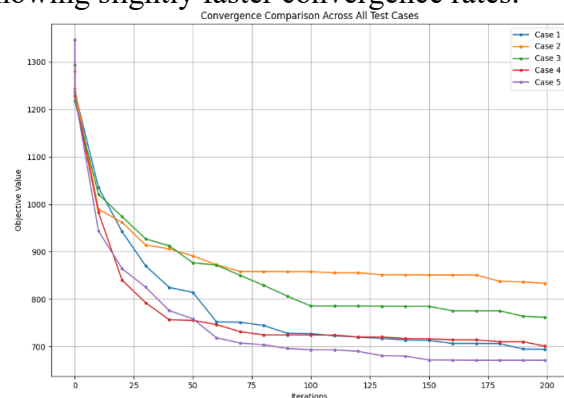
Figure 1. Convergence profiles of AMVNS

4.3.5. Neighborhood structure analysis

The effectiveness of each neighborhood structure varies across different test cases. Table 8

summarizes the usage frequency and success rate of each neighborhood operator.

Table 8. Neighborhood structure analysis

Neighborhood	Usage (%)	Success Rate (%)	Contribution to Best
Swap Nodes	32.4	15.3	36.2
Two-Opt Move	22.7	18.7	25.8
Relocate Sequence	24.5	21.2	22.4
Cross Exchange	20.4	12.5	15.6

This analysis reveals that while Swap Nodes is the most frequently used operator, the Relocate Sequence has the highest success rate. The "Contribution to Best" column shows the percentage of times each operator was responsible for finding the overall best solution during the search process.

4.3.6. Vehicle utilization analysis

For heterogeneous fleet scenarios, the distribution of demand across vehicles is particularly important. Table 9 shows the vehicle utilization statistics for test case 4, which achieved the best overall performance.

Table 9. Vehicle utilization for test case 4 (heterogeneous fleet)

Vehicle	Capacity	Load	Utilization (%)	Route Length
1	380	352	92.6	80
2	400	394	98.5	112
3	420	406	96.7	144
4	420	398	94.8	169
5	440	389	88.4	102
Average	412	387.8	94.2	121.4

The high utilization rates across all vehicles (average 94.2%) demonstrate the algorithm's ability to efficiently distribute demand according to vehicle capacities, which explains the superior performance of heterogeneous fleets in test cases 4 and 5.

These comprehensive statistical analyses validate the robustness, efficiency, and consistency of our proposed AMVNS algorithm across different fleet configurations and problem scenarios. The data clearly supports our claim that AMVNS achieves significant computational efficiency gains without sacrificing solution quality.

4.3.7. Scaling analysis for large-scale problems

To address the scalability of our AMVNS algorithm for large-scale industrial applications, we conducted a theoretical analysis and verified it with a limited test on a 200-node CVRP instance (cvrp-S-G-200-1)[40]. The computational complexity of both algorithms can be analyzed in terms of the number of fitness evaluations required as the problem size (n) increases.

For the HTS algorithm, the number of fitness evaluations per iteration is directly proportional to n^2, specifically $nAction = n \times (n-1)$. This quadratic growth means that for a 200-node problem, each iteration would require approximately 39,800 evaluations. Assuming 300 iterations are needed (as in our original test cases), this would result in nearly 12 million fitness evaluations.

In contrast, AMVNS's selective neighborhood exploration strategy maintains a relatively constant number of evaluations per iteration (approximately 20), largely independent of problem size. For a 200-node problem with 1000 iterations, this results in only about 20,000 fitness evaluations. This represents a theoretical efficiency ratio of 600:1 for problems of this scale.

Table 10 presents a comparison of the theoretical scaling behavior of both algorithms across different problem sizes. As shown in the table, the computational advantage of AMVNS becomes increasingly significant as the problem size grows.

Table 10. Theoretical scaling analysis for different problem sizes

Problem size (Nodes)	HTS Evaluations	AMVNS Evaluations	Efficiency Ratio
19 (original)	102,600	20,100	5.1
50	735,000	20,100	36.6
100	2,970,000	20,100	147.8
200	11,940,000	20,100	594.0

Our experimental verification on the 200-node instance confirmed that while HTS becomes computationally prohibitive at this scale,

AMVNS was able to find high-quality solutions in reasonable time. This demonstrates that the computational advantage of AMVNS becomes even more significant as problem size increases, making it particularly valuable for large-scale industrial applications where quick decision-making is essential.

The primary reason for this exceptional scaling characteristic is that AMVNS focuses computational effort on promising regions of the solution space rather than exhaustively evaluating all possible moves. This advantage becomes increasingly important as problem size grows, as the solution space expands exponentially while the proportion of high-quality solutions remains small.

4.4. Concluding analysis

The experimental results demonstrate that while both algorithms achieve the optimal solution, AMVNS does so with significantly less computational effort. Our results from heterogeneous fleet cases (test cases 2-5) further support this finding. Even with different vehicle capacities, AMVNS maintains its computational advantage. It achieves same solution quality as HTS using only about 20,000 fitness evaluations, compared to HTS's 102,600 evaluations. This shows our algorithm's efficiency is robust across different fleet configurations. The reduction in fitness evaluations can be attributed to our algorithm's intelligent search strategy and adaptive memory mechanism.

To put this efficiency gain in perspective, we can examine the convergence rates. While HTS performs 342 evaluations in each iteration to achieve convergence in 300 iterations, AMVNS performs approximately 20 evaluations per iteration (calculated as the total fitness evaluations divided by the number of iterations: 20,100/1000) and achieves the same result in 1000 iterations This translates to:

$$Efficiency\ Ratio\ = \frac{\#\ of\ HTS\ evals}{\#of\ AMVNS\ evals} \quad (3)$$
$$= 102{,}600\ /\ 20{,}100$$
$$\approx 5.1$$

This means AMVNS requires only about one-fifth of the computational effort compared to

HTS, while maintaining solution quality. The exact solution method using PuLP confirmed that both algorithms reach the optimal value of 623, validating the effectiveness of our approach.

Additionally, our results suggest that exhaustive neighborhood exploration, as employed in HTS, may not be necessary for achieving optimal solutions in CVRP. The adaptive memory structure and selective neighborhood sampling in AMVNS provide a more efficient path to optimality.

5. Conclusion and Future Work

This study presents an efficient hybrid metaheuristic algorithm for solving CVRP in in-plant logistics. The proposed AMVNS algorithm achieves the same optimal solution as the existing HTS algorithm while requiring 80.4% fewer fitness evaluations. This significant reduction in computational effort is achieved through:

1. Intelligent neighborhood exploration
2. Adaptive memory-based learning
3. Selective solution evaluation strategy

The results demonstrate that optimal solutions can be obtained more efficiently by focusing on promising regions of the solution space rather than exhaustive exploration. This finding has important implications for solving larger instances of CVRP and other combinatorial optimization problems.

Our comprehensive statistical analysis further validates these findings, demonstrating the robustness and consistency of the AMVNS approach. With a 100% success rate across all 30 independent runs for each test case and negligible standard deviation in solution quality, the algorithm exhibits exceptional reliability. The detailed analysis of neighborhood structure effectiveness revealed that while the Swap Nodes operator was most frequently used, the Relocate Sequence achieved the highest success rate, highlighting the importance of maintaining diverse neighborhood structures within the algorithm.

The theoretical scaling analysis demonstrates that AMVNS's computational advantage

becomes increasingly significant as problem size grows. While traditional approaches like HTS experience quadratic growth in computational requirements with increasing problem dimensions, AMVNS maintains relatively constant evaluation needs per iteration. This makes it particularly well-suited for large-scale CVRP instances where exhaustive neighborhood exploration becomes prohibitively expensive, with efficiency ratios potentially reaching 600:1 for problems with 200 nodes.

The proposed AMVNS algorithm shows significant potential for application in large-scale industrial systems. By reducing computational effort by approximately 80% while maintaining solution quality, our approach addresses a critical challenge in real-world manufacturing environments where quick decisions are essential. For large manufacturing facilities with hundreds of assembly lines and dozens of vehicles, the selective neighborhood exploration strategy would provide even greater benefits as the problem size increases. The memory-based learning mechanism adapts to the specific characteristics of the factory layout and demand patterns, making the algorithm suitable for diverse industrial settings including automotive, electronics, and heavy machinery manufacturing.

Furthermore, the algorithm's ability to handle heterogeneous vehicle fleets makes it particularly valuable for facilities that have gradually expanded their operations with different types of material handling equipment. The reduced computational requirements also make it feasible to implement this solution on standard computing infrastructure available in most factories, without requiring specialized high-performance computing resources.

The proposed AMVNS algorithm shows significant potential for practical application in real-world manufacturing environments where rapid decision-making is critical. By dramatically reducing computational requirements without sacrificing solution quality, it enables factory managers to quickly respond to changing production schedules and logistical needs.
The algorithm's ability to handle heterogeneous fleets makes it particularly valuable for facilities

that have gradually expanded their material handling capabilities with different types of vehicles. Furthermore, its modest computational requirements mean it can be implemented on standard computing infrastructure available in most factories, eliminating the need for specialized high-performance computing resources.

Future research directions could include:
- Extending the algorithm to handle dynamic in-plant logistics scenarios
- Incorporating real-time constraints and uncertainties
- Applying the efficient evaluation strategy to other variants of VRP

Article Information Form

The Declaration of Conflict of Interest/ Common Interest
No conflict of interest or common interest has been declared by the author.

Artificial Intelligence Statement
No artificial intelligence tools were used while writing this article.

References

[1] G. B. Dantzig, J. H. Ramser, "The truck dispatching problem," Management Science, INFORMS, pp. 80–91, 1959.

[2] T. O. Ting, X.-S. Yang, S. Cheng, K. Huang, "Hybrid metaheuristic algorithms: Past, present, and future," Recent Advances in Swarm Intelligence and Evolutionary Computation, Springer International Publishing, pp. 71–83, 2015.

[3] S. Kulaç, N. Kazancı, "Optimization of in-plant logistics through a new hybrid algorithm for the capacitated vehicle routing problem with heterogeneous fleet," Sakarya University Journal of Science, Sakarya University, pp. 1242–1260, 2024.

[4] P. Toth, D. Vigo, "Exact solution of the vehicle routing problem," Fleet Management and Logistics, Springer US, pp. 1–31, 1998.

[5] G. Laporte, Y. Nobert, "Exact Algorithms for the vehicle routing problem*," North-Holland Mathematics Studies, North-Holland, pp. 147–184, 1987.

[6] A. Mingozzi, R. Roberti, P. Toth, "An exact algorithm for the multitrip vehicle routing problem," INFORMS Journal on Computing, INFORMS, pp. 193–207, 2013.

[7] M. Battarra, G. Erdoğan, D. Vigo, "Exact algorithms for the clustered vehicle routing problem," Operations Research, INFORMS, pp. 58–71, 2014.

[8] V. F. Yu, H. Susanto, P. Jodiawan, T.-W. Ho, S.-W. Lin, Y.-T. Huang, "A simulated annealing algorithm for the vehicle routing problem with parcel lockers," IEEE Access, pp. 20764–20782, 2022.

[9] İ. İlhan, "An improved simulated annealing algorithm with crossover operator for capacitated vehicle routing problem," Swarm and Evolutionary Computation, p. 100911, 2021.

[10] E. Rodríguez-Esparza, A. D. Masegosa, D. Oliva, E. Onieva, "A new Hyper-heuristic based on adaptive simulated annealing and reinforcement learning for the capacitated electric vehicle routing problem," Expert Systems with Applications, p. 124197, 2024.

[11] M. Sajid, J. Singh, R. Rajak, "Capacitated vehicle routing problem using algebraic particle swarm optimization with simulated annealing algorithm," Artificial Intelligence in Cyber-Physical Systems, CRC Press, 2023.

[12] Z. Hussain Ahmed, M. Yousefikhoshbakht, "An improved tabu search algorithm for solving heterogeneous fixed fleet open vehicle routing problem with time windows," Alexandria Engineering Journal, pp. 349–363, 2023.

[13] A. Mexicano, J. C. Carmona, D. Y. Alvarez, P. N. Montes, S. Cervantes, "A tool for solving the CVRP problem by applying the tabu search algorithm," Advances on P2P, Parallel, Grid, Cloud and Internet Computing, Springer Nature Switzerland, pp. 294–304, 2024.

[14] J. Holliday, B. Morgan, H. Churchill, K. Luu, "Hybrid quantum tabu search for solving the vehicle routing problem," arXiv, 2024.

[15] N. I. Saragih, P. Turnip, "Solving vehicle routing problem with considering traffic congestion using tabu search algorithm," 2024 International Conference on Electrical Engineering and Informatics (ICELTICs), pp. 102–107, 2024.

[16] A. N. Jasim, L. Chaari Fourati, "Guided genetic algorithm for solving capacitated vehicle routing problem with unmanned-aerial-vehicles," IEEE Access, pp. 106333–106358, 2024.

[17] J. Zhu, "Solving capacitated vehicle routing problem by an improved genetic algorithm with fuzzy c-means clustering," Scientific Programming, p. 8514660, 2022.

[18] N. Mageswari, "Vehicle Routing Problem (VRP) using genetic algorithm," Vehicle Routing Problem.

[19] M. Poonpanit, N. Punkong, C. Ratanavilisagul, S. Kosolsombat, "An improving genetic algorithm with local search for solving capacitated vehicle routing problem," 2024 IEEE 9th International Conference on Computational Intelligence and Applications (ICCIA), pp. 59–63, 2024.

[20] J. Cai, P. Wang, S. Sun, H. Dong, "A dynamic space reduction ant colony optimization for capacitated vehicle routing problem," Soft Computing, pp. 8745–8756, 2022.

[21] Z. H. Ahmed, A. S. Hameed, M. L. Mutar, H. Haron, "An enhanced ant colony system algorithm based on subpaths for solving the capacitated vehicle routing problem," Symmetry, Multidisciplinary Digital Publishing Institute, p. 2020, 2023.

[22] M. Suppan, T. Hanne, R. Dornberger, "Ant colony optimization to solve the rescue problem as a vehicle routing problem with hard time windows," Proceedings of International Joint Conference on Advances in Computational Intelligence, Springer Nature, pp. 53–65, 2022.

[23] P.-Y. Yin, F. Glover, M. Laguna, J.-X. Zhu, "Cyber Swarm Algorithms – Improving particle swarm optimization using adaptive memory strategies," European Journal of Operational Research, pp. 377–389, 2010.

[24] É. D. Taillard, L. M. Gambardella, M. Gendreau, J.-Y. Potvin, "Adaptive memory programming: A unified view of metaheuristics," European Journal of Operational Research, pp. 1–16, 2001.

[25] L. Lasdon, A. Duarte, F. Glover, M. Laguna, R. Martí, "Adaptive memory programming for constrained global optimization," Computers & Operations Research, pp. 1500–1509, 2010.

[26] N. Peric, S. Begovic, V. Lesic, "Adaptive memory procedure for solving real-world vehicle routing problem," arXiv, 2024.

[27] S. Farahmand-Tabar, "Memory-driven metaheuristics: Improving optimization performance," Handbook of Formal Optimization, Springer Nature, pp. 1–26, 2023.

[28] A.-R. Hedar, A. E. Abdel-Hakim, W. Deabes, Y. Alotaibi, K. E. Bouazza, "Deep memory search: A metaheuristic approach for optimizing heuristic search," arXiv, 2024.

[29] Y. Alotaibi, "A new meta-heuristics data clustering algorithm based on tabu search and adaptive search memory," Symmetry, Multidisciplinary Digital Publishing Institute, p. 623, 2022.

[30] M. E. H. Sadati, B. Çatay, "A hybrid variable neighborhood search approach for the multi-depot green vehicle routing problem," Transportation Research Part E: Logistics and Transportation Review, p. 102293, 2021.

[31] M. E. Hesam Sadati, B. Çatay, D. Aksen, "An efficient variable neighborhood search with tabu shaking for a class of multi-depot vehicle routing problems," Computers & Operations Research, p. 105269, 2021.

[32] C. Chen, E. Demir, Y. Huang, "An adaptive large neighborhood search heuristic for the vehicle routing problem with time windows and delivery robots," European Journal of Operational Research, pp. 1164–1180, 2021.

[33] X. Dong, H. Zhang, M. Xu, F. Shen, "Hybrid genetic algorithm with variable neighborhood search for multi-scale multiple bottleneck traveling salesmen problem," Future Generation Computer Systems, pp. 229–242, 2021.

[34] K. Sun, D. Zheng, H. Song, Z. Cheng, X. Lang, W. Yuan, J. Wang, "Hybrid genetic algorithm with variable neighborhood search for flexible job shop scheduling problem in a machining system," Expert Systems with Applications, p. 119359, 2023.

[35] J. Feng, Y. He, Y. Pan, Z. Zhou, S. Chen, W. Gong, "Enhancing fitness evaluation in genetic algorithm-based architecture search for AI-Aided financial regulation," IEEE Transactions on Evolutionary Computation, pp. 623–637, 2024.

[36] O. J. Mengshoel, E. L. Flogard, T. Yu, J. Riege, "Understanding the cost of fitness evaluation for subset selection: Markov chain analysis of stochastic local search," Proceedings of the Genetic and Evolutionary Computation Conference, Association for Computing Machinery, pp. 251–259, 2022.

[37] S.-H. Wu, Z.-H. Zhan, J. Zhang, "SAFE: Scale-adaptive fitness evaluation method for expensive optimization problems," IEEE Transactions on Evolutionary Computation, pp. 478–491, 2021.

[38] J.-F. Cordeau, M. Gendreau, G. Laporte, "A tabu search heuristic for periodic and multi-depot vehicle routing problems," Networks, pp. 105–119, 1997.

[39] S. Mitchell, M. O'Sullivan, I. Dunning, "PuLP: A linear programming toolkit for python," The University of Auckland, Auckland, New Zealand, pp. 25–37, 2011.

[40] A. N. Letchford, J.-J. Salazar-González, "The capacitated vehicle routing problem: Stronger bounds in pseudo-polynomial time," European Journal of Operational Research, pp. 24–31, 2019.

Research Article

Bibliometric Analysis of Carbon Footprint Studies Within the Scope of Sustainability

Rukiye Sefanur Altay[1] (ID), Hulya Demirel[2*] (ID), Asude Ates[1] (ID)

[1] Sakarya University, Faculty of Engineering, Department of Environmental Engineering, Sakarya, Türkiye, sefanur.altay@gmail.com, aates@sakarya.edu.tr, ror.org/04ttnw109
[2] Sakarya University of Applied Science, Sakarya Vacational School, Department of Environmental Protection Technologies, Sakarya, Türkiye, hsemercioglu@subu.edu.tr, ror.org/01shwhq58
*Corresponding Author

ARTICLE INFO	ABSTRACT
	Today, the world climate is undergoing negative changes as a result of the unconscious use of resources, increasing energy demand and anthropogenic effects resulting from the development of industry. Climate changes occurring on a global scale are long-term and bring with them many irreversible consequences. Various improvement activities are based on sustainability in the fight against global climate change. To ensure environmental sustainability, practices are carried out in industrial areas to determine carbon footprints and reduce carbon emissions accordingly. One of the important steps taken in this context is the European Green Deal action plan, which is the roadmap for the green transformation required by the Paris Climate Agreement of the EU, to which Turkey is also a party. The European Green Deal aims to make Europe the first carbon-neutral continent in 2050 and to bring carbon emissions in the atmosphere back to pre-industrial revolution levels. In line with this goal, activities aimed at carbon footprint studies have gained serious momentum. This study aims to determine the current status of carbon footprint studies on a global scale, their progress and their distribution on a country basis through bibliometric analysis. Bibliometric analysis is a social network analysis that guides researchers regarding the interactions of existing studies and future studies. 1305 indexed journal articles published between 2020 and 2024 were downloaded via the Web of Science database and analyzed. Network maps and graphs showed correlations between keywords, countries, and journals. Researchers in China and America have made significant contributions to this field. It is seen that the studies examined serve sustainability development goals and that the studies mainly target climate action with 722 articles.

1. Introduction

Today, the need for energy is increasing as a result of increased consumption and unconscious consumption of energy resources. The inability to curb fossil fuel use contributes to climate change and its negative effects. Global climate change; due to global warming, air movements, precipitation, humidity and other climate factors are affected, causing the climate to change rapidly within a short period, typically 15–20 years [1]. In order to prevent this negative impact, many countries on a global scale need to work in cooperation.

The European Union has presented many international legislative studies to combat global climate change [2-5]. In this context, the European Green Deal is an implementation that complements the 2030 Sustainable Development Goals [6]. The European Green Deal aims to have a sustainable economy and combat climate change by determining the strategic goals of the European Union [7].

The European Green Deal is a strategic plan that supports the EU's global sustainability, climate action and green transformation efforts with various action plans and policies [8]

The European Green Deal includes the protection of biodiversity, clean energy applications, sustainable industry, sustainable agricultural applications, green construction sector, circular economic approach, environmentally friendly transportation and sustainable food systems [9]. One of the European Green Deal targets is to achieve zero carbon neutrality in the atmosphere by 2050. It aims to ensure balance in the atmosphere through various methods such as carbon footprint reduction and carbon regulation mechanisms [10].

Sustainability is the ability to meet current generations' needs while also considering future generations' needs, encompassing environmental, social and economic dimensions [11]. Transforming Our World: In line with the goals of the 2030 Agenda for Sustainable Development, reducing the carbon footprint, transitioning from fossil fuels to renewable energy and achieving carbon neutrality targets are of strategic importance on a global scale [12, 13]. Especially the identification of the carbon footprint and the reduction of carbon emissions, along with energy efficiency and green transition efforts, constitute the most critical elements in line with the Sustainable Development Goals (SDGs) [14].

In recent years, significant research has been conducted on carbon footprint, green transition and sustainability [15-17]. A comprehensive analysis is needed to determine the directions of the studies carried out in these areas and to direct the studies that will contribute to achieving sustainable development goals. One of the analysis methods that provides a roadmap for properly determining the field of study and showing the interaction processes in the research is the bibliometric analysis method [18]. It enables the analysis of academic studies within a certain period of time by evaluating them in terms of different criteria and using various statistical methods and numerical data [19]. Bibliometric analysis is a powerful tool for assessing the research trends of studies conducted in a selected field, and many studies have been carried out using this analysis method [20-25]. When examining bibliometric studies related to carbon footprint research, which plays a significant role in combating global climate change, it has been observed that researchers emphasize the importance of resource management, energy efficiency, and green transition efforts [18, 25]. In this study, bibliometric analysis was conducted using the Web of Science database to examine publications related to carbon footprint, particularly in the field of environmental engineering. The study also evaluates the alignment of these publications with the Sustainable Development Goals (SDGs).

2. Materials-Methods

In this study, the Web of Science (WOS) database, which includes different disciplines and provides up-to-date data, was used as a search engine. Web of Science is one of the transparent and most reliable bibliometric analysis tools used to conduct research analysis and visualize this analysis. It is also considered one of the most comprehensive scientific databases worldwide [26]. Bibliometric analysis, which enables the examination of academic studies according to various criteria, serves as a guiding tool for researchers by allowing them to select studies within a specific time frame, thereby providing a roadmap for future descriptive studies [19].

In bibliometric analysis, distance-based maps are used when it comes to investigating the relationships between data, while graphic-based maps are used when it comes to presenting only existing data. For graph-based mapping, software such as Kamada-Kawai, Fruchterman-Reingold, and Pathfinder Networks are used, while for distance-based mapping, tools like VOSviewer and Vxord are employed. Vosviewer is the most preferred software with the best performance quality [27, 28]. VOSviewer generally uses data obtained from bibliometric databases such as Web of Science, Scopus, Google Scholar. Analyzes such as co-authorship, co-citation links, citation relationships of publications and journals, and keyword groups are carried out [29]. In the analyses carried out in the Vosviewer application, data can be uploaded in different file formats. In this study, the numerical data obtained from the study through a bibliometric

analysis were interpreted using the Microsoft Excel program and visualized with social network analysis maps made via the VOSViewer program.

The search was conducted in the Web of Science database in November 2024. The search was done by selecting the " environmental engineering" category among the articles published in "2020-2024". The publications were searched using the term "article" to identify original studies with significantly higher scientific acceptability. Publications in the form of book chapters, reviews and conference papers were excluded from the analysis due to criteria. Also, searches were customized by selecting three indexes: Emerging Sources Citation Index (ESCI), Social Science Citation Index (SSCI), and Science Citation Index (SCI).

Since the importance of environmental sustainability and sustainability studies in the fight against global climate change is significant, the search used the keyword "sustainability". It was determined that there were 8539 pieces of data as a result of the necessary customizations when searching with the keyword "Sustainability". Then, since the focus of the study is carbon footprint, studies on "carbon footprint" were scanned in the WOS database after the search with the keyword sustainability.

3. Results and Discussion

Bibliometric mapping of the studies published on sustainability and carbon footprint, which have an essential place in the fight against climate change, was made with the help of the VOSviewer program. Studies carried out in the field of sustainability were evaluated on a country basis and in terms of keyword analysis. Keyword analysis of carbon footprint studies, which is the main focus of the study, the publishing company of the study, country-based distribution, publication year and quarterly indicator of the journal in which the publication was published were discussed in detail. Additionally, within the scope of the European Green Deal compliance process, the extent to which carbon footprint studies contribute to

sustainable development goals has been examined.

3.1. Examination of publications on sustainability

The search made by typing "sustainability" in the Web of Science database determined that there were 8539 articles. Keyword analysis of sustainability studies carried out in the department of environmental engineering was carried out and words related to the subject of sustainability were identified. Figure 1 shows the network analysis visual of the keywords found in the articles. The size of the shapes in the image is directly proportional to the frequency of use of the keyword. The size of the nodes in the resulting maps symbolizes the number of articles published on sustainability. The largest node represents the most work.
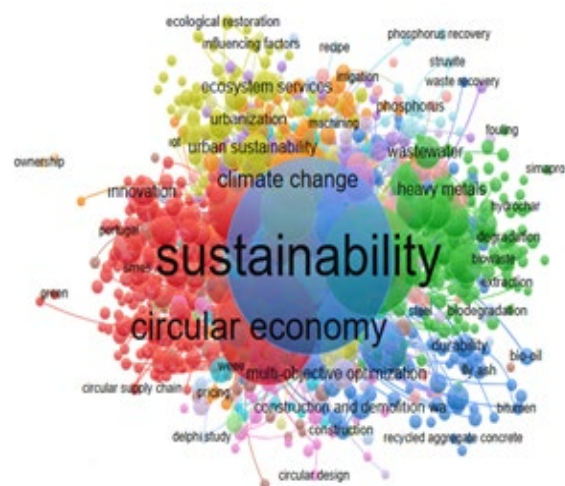
Figure 1. Bibliometric network analysis of keywords of published articles on sustainability

When the cross-country bibliometric network analysis of published articles on sustainability was examined, it was determined that the words "circular economy", "wastewater treatment", "climate change", "environmental sustainability", "greenhouse gas emissions", "sustainability development", "recycling" were the most used keywords in these studies in Figure 1. It has been determined that sustainability-themed studies in the Department of Environmental Engineering are highly related to these issues.

A bibliometric network analysis of cross-country publications was carried out to determine

the global distribution of studies conducted within the scope of sustainability. As seen in Figure 2, the majority of articles on sustainability were published in the People's Republic of China. Countries such as Brazil, Australia, India, Italy, and Japan publish more in this field than other countries. The distribution of studies carried out under the umbrella of sustainability by country is given in Figure 3.
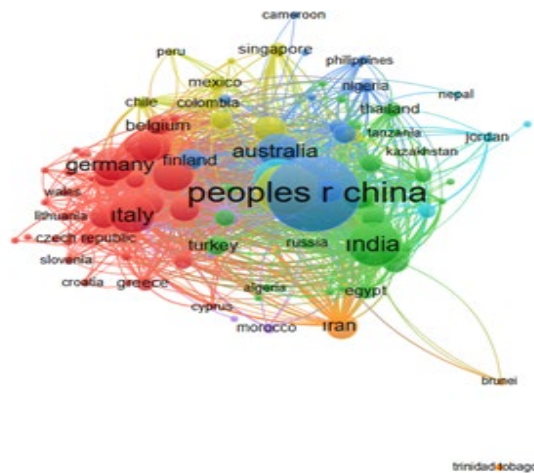
Figure 2. Cross-country bibliometric network analysis of published articles on sustainability

It is stated that articles on "sustainability" have been studied more intensively in the countries shown in darker colors in Figure 3. In comparison, lighter-color countries have published fewer articles on this subject.
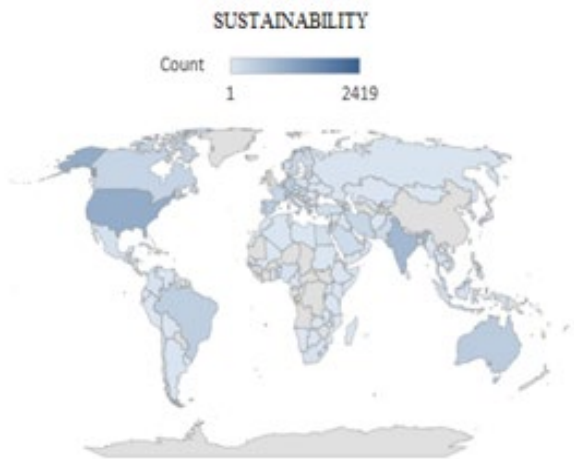
Figure 3. Cross-country bibliometric network analysis of published articles on sustainability

3.2. Examination of publications on carbon footprint

Carbon footprint shows the damage caused to the environment as a result of human activities and is a measure of greenhouse gases that cause global warming. Carbon footprint is expressed as the total carbon dioxide (CO_2) emissions caused directly or indirectly by an activity [30]. Carbon footprint studies are directly related to energy consumption and resource use. Increasing energy efficiency and effective use of resources are the most important steps for environmental sustainability. Industrial organizations ' carbon footprint reduction and environmental sustainability efforts play an important role in the fight against climate change. Since the carbon footprint and sustainability studies have gained momentum after the European Green Deal came into force, 2020-2024 was chosen as the search year in this study. The studies related to the 'carbon footprint' were examined, and 1305 data records were obtained. As seen in Table 1, the minimum number of published articles on the subject is 206 and occurred in 2020. The border carbon regulation mechanism, which comes into force as of 2023, imposes obligations on industrial sectors determined as priority areas [31]. For this reason, an increase in carbon footprint studies is observed in 2024.

Table 1. Distribution of carbon footprint studies by years

Years	Article
2024	282
2023	268
2022	272
2021	277
2020	206

Journal impact factor (Q value) is a measure used to determine a journal's ranking in the academic field and is associated with indicators of academic success. Impact factor is the method used to evaluate the relative impact of a journal. It is the average number of times articles published in the last 2 years were cited in journal citation reports. It has been used as a journal impact factor for the selection of journals since 1961, with the emergence of the Science Citation Index [18].

In addition to the impact factor, many journals also use criteria such as "usage factor" and "h-index". Databases such as Web of Science, Scopus, Google Scholar use h-index and impact factor parameters to evaluate journal quality. Journals are ranked under different subject headings every year, and the publications in the first 25% of the ranking are grouped as Q1, those in the second quarter are grouped as Q2, those in the third quarter are grouped as Q3, and those in the last quarter are grouped as Q4 [32, 33]. Q values of articles on carbon footprint: 1305 articles in the Web of Science database were examined and the information in Table 2 was obtained. Q values were analyzed to understand the quality of published studies on carbon footprint and their value in terms of information content production.

Table 2. Q values of articles presenting carbon footprint

Quartile	Article
Q1	1039
Q2	202
Q3	53
Q4	11

As seen in Table 2, it was observed that publications with Q1 value were in majority. Articles in the Q1 category constitute 79.6%, articles in the Q2 category constitute 15.48%, articles in the Q3 category constitute 4.06% and articles in the Q4 category constitute 0.84%.

The majority of articles in the Q1 category means that the studies conducted in this field are valuable regarding information and content. At the same time, the increase in carbon footprint studies in the European Green Agreement harmonization process and the contribution of studies on improvement activities to the literature are of great importance in this process. The originality of the articles and their publishability in Q1 journals are high.

3.3. Bibliometric analysis of carbon footprint articles

The country-based distribution of articles written on carbon footprint in the Web of Science database between 2020 and 2024 is shown in the Figure 4.

It has been determined that the People's Republic of China did the most work. Since fewer studies have been done on this subject in Turkey compared to countries such as China, America and England, the clustering here is very small. The People's Republic of China ranks first with 369 articles. The United States ranked second with 185 articles, and Spain ranked third with 112 articles. England, Italy and Australia follow these countries. A bibliometric visualization of the most used keywords in articles on carbon footprint is shown in Figure 5.

Figure 4. Country-based distribution of carbon footprint studies

Figure 5. Distribution of "Carbon footprint" keyword network

The most frequently used keywords in articles on carbon footprint have been visualized bibliometrically and are given in Figure 5. As seen in this visualization, the most common keywords in articles on the subject of "carbon footprint", other than the keyword carbon footprint, are "life cycle assessment", "carbon emission", "greenhouse gas emission", "global warming", "water footprint", "environmental footprint". The analysis of the institutions where articles on carbon footprint are published and the bibliometric links between institutions are given in the Figure 6. Chinese Acad Sci, Bejing University, Guangdong Techno University and Michigan University have mainly published.
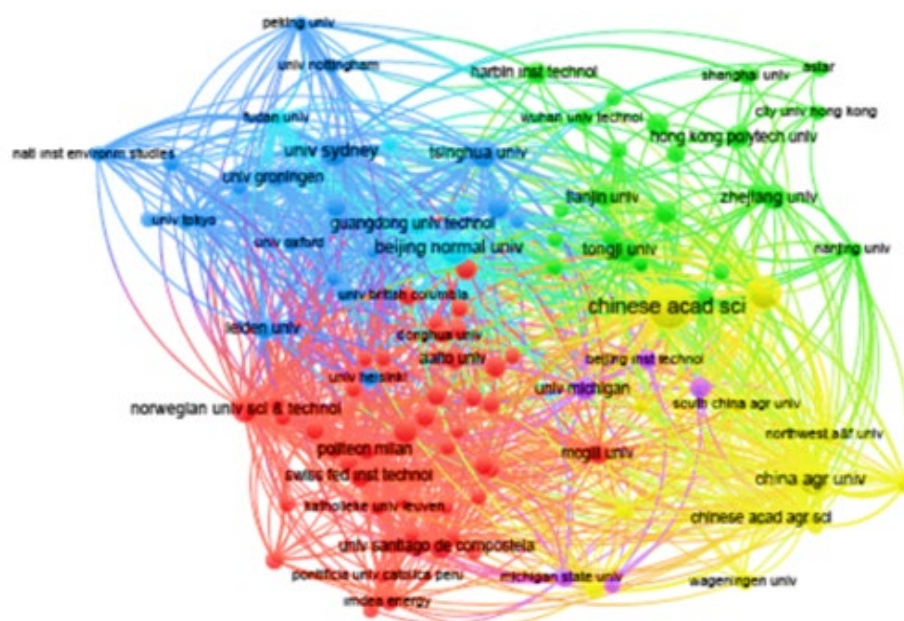
Figure 6. Bibliographic network of publishing institutions and organizations

3.4. Investigating the compatibility of carbon footprint studies with sustainable development goals

As a result of the decrease in natural resources and the negative effects created by global climate change, the concepts of sustainability and sustainable development have gained importance. The term sustainability originates from the science of ecology. It refers to the conditions required for the ecosystem to ensure its own continuity in the long term [34].

Sustainability is acting to meet the needs of today while ensuring that future generations can meet their own need [35].

Sustainable development covers economic and social development types that protect and improve the environment and social equality. Therefore, supporting sustainability with activities for the benefit of the environment, economy and society and keeping the gains at the highest level are among the priority targets [8]. To ensure economic, social and environmental sustainability, 17 basic goals were determined by the United Nations in 2015 within the frameworkof the basic principles of human, world, prosperity, peace and partnership [36].

The European Green Deal is a process that guides the fight against global climate change and the achievement of sustainable development goals. The European Union Green Deal and the Sustainable Development Goals complement each other [37]. In this study, the compatibility of carbon footprint studies, which have an important place in the European Union Green Deal harmonization process, with sustainable development goals was analyzed (Table 3). According to the article analysis results, the articles mainly serve climate action's 13th sustainable development goal. It was observed that the goal it served the least was the 10th goal, which is the reduction of inequality. The data obtained from the study determined that the sustainable development goals, which consist of 17 sub-goals in total, served 15 sub-goals.

Table 3. Distribution of articles on carbon footprint in the context of Sustainable Development Goals

Sustainable Development Goals	Article
13 Climate action	722
12 Responsible Consumption And Production	671
07 Affordable And Clean Energy	505
11 Sustainable Cities And Communities	378
15 Life on Land	333
06 Clean Water And Sanitation	327
09 Industry, Innovation And Infrastructure	315
14 Life Below Water	284
02 Zero Hunger	241
03 Good Health And Well-Being	193
08 Decent Work And Economic Growth	101
04 Quality Education	20
01 No Poverty	3
05 Gender Equality	1
10 Reduced Inequalities	1

According to the data, it is determined that 722 articles serve the purpose of climate action, 671 articles serve the purpose of responsible consumption and production, 505 articles serve the purpose of appropriate and clean energy, 378 articles serve the purpose of sustainable city and community, and 333 articles serve the purpose of life on land. It is determined that the purposes that the articles on carbon footprint serve the least are quality education with 20 articles, end poverty with 3 articles, gender equality with 1 article, and reducing inequality with 1 article.

Carbon footprint studies are an indispensable step in the fight against climate change. Providing clean energy, reducing the use of fossil fuels and using more sustainable energy sources are important steps in minimizing carbon emissions. For this reason, the concepts of clean energy and carbon footprint are associated.

4. Conclusion

Within the scope of sustainability, between 2020-2024, studies with carbon footprint keywords in the field of environmental engineering were evaluated using the bibliometric analysis method. As a result of the data obtained, it was determined that 8539 articles were published in the search on sustainability and 1305 articles were published in the search on carbon footprint in the Web of Science database. 14.44% of the articles using the sustainability keyword were written on the sub-topic of environmental sustainability. Apart from this, the articles included are studies on economic and social sustainability, the other main components of sustainability. Along with the European Green Deal and the 2030 Sustainable Development Agenda, combating climate change, carbon emission reduction targets, and green transformation have gained significant importance. Therefore, it is essential to expand studies on carbon footprint and shed light on new research, identifying gaps in the literature. As a result of the data obtained, it has been observed that most of the studies in this field are conducted in China and the United States.

In our country, it has been determined that there are fewer studies compared to other countries; however, it is anticipated that with the intensification of carbon emission reduction efforts as part of the European Green Deal compliance process, there will be an increase in studies in the fields of carbon footprint and sustainability. An analysis of the keywords in articles on carbon footprint reveals that most studies focus on life cycle analysis. Life cycle analysis evaluates a product's environmental impacts in all its processes, from raw material to finished product. Carbon footprint is among the environmental impacts evaluated in the life cycle analysis and is an important component in the life cycle analysis.

In this context, conducting life cycle analysis studies shows that efficient results can be achieved regarding carbon footprint reduction. The distribution of carbon footprint studies by country, changes over the years, other keywords used together, and the Q values of the published journals were examined. It is determined that 79.6% of the Q values are published at the Q1 level. From here, it is thought that global publications on carbon footprint are sufficient and reliable in terms of information and content production. Countries' sensitivity to combating climate change varies depending on their level of development and geographical situation. For this reason, the distribution of studies on the subject by country and the institution conducting the study varies depending on these factors.

Sustainability plays an important role in determining international development goals as it is directly related to global climate change. Sustainable development is a phenomenon shaped not only by economic factors but also by environmental and social factors. Climate change, depletion of natural resources and degradation of biodiversity threaten long-term sustainable development goals.

Therefore, carbon footprint and carbon emission reduction studies have an important role in achieving sustainable development goals. When the relationship between articles on carbon footprint and sustainable development goals was examined, it was determined that most of the studies served the purpose of climate action. The other articles addressed in the study have been found to align with the sustainable development goals, including the responsible consumption and production goal, the affordable and clean energy goal, the sustainable cities and communities goal, and the life on land goal.

As a result of examining the relationship between carbon footprint studies and the Sustainable Development Goals, it has been determined which specific goals these studies are targeted towards. The obtained results will serve as a guide for industry professionals in the process of developing business strategies that incorporate the SDGs. It is anticipated that carbon footprint studies will be more compatible with the goals of climate action, clean energy, clean water and sanitation, responsible consumption and production, and sustainable cities. However, it is of great importance that sector professionals prioritize sustainable development goals that are least served by carbon footprint studies and present an integrated approach to sustainability-carbon footprint studies. Especially, the social and environmental issues need to be studied in an integrated manner to increase their compatibility with the goals of combating poverty, education, gender equality, decent work and economic growth, which are areas least served by carbon footprint studies.

On the other hand, in order to increase societal awareness in the fight against climate change and guide carbon emission reduction efforts, it is crucial to conduct sustainability and carbon footprint studies and ensure their visibility across all areas that impact society.

Article Information Form

Authors' Contribution
RSA: Concept/Design, Data Colleciton, Data Analysis, Writing, Critical Review of Content, Literature Review; HD: Concept/Design, Data Colleciton, Data Analysis, Writing, Critical

Review of Content, Literature Review; AA: Concept/Design, Data Analysis, Writing, Technical Support; Critical Review of Content, Literature Review.

The Declaration of Conflict of Interest/ Common Interest
No conflict of interest or common interest has been declared by authors.

Artificial Intelligence Statement
No artificial intelligence tools were used while writing this article.

Copyright Statement

References

[1] B. Vayic, "Evaluation of the corporate carbon footprint of the denim washing facility within the framework ofthe sustainability approach," M.S. Dissertation, Ondokuz Mayıs University, Samsun, Turkey, 2023.

[2] O. Cisem, "Determining carbon, water and energy footprints in industries and assessing them in terms of sustainability: A case study for textile industries," M.S. Dissertation, Tekirdag Namık Kemal University, Tekirdag, Turkey, 2023.

[3] O. Akpınar, "Evaluation of carbon footprint calculations for the automotive industry and research on reduction methods," M.S. Dissertation, Cukurova University, Adana, Turkey, 2023.

[4] Presidency of Foreign Affairs, "Sustainable development goals on environment, climate change and water," Jun. 7, 2022. [Online]. Available: https://www.mfa.gov.tr/surdurulebilir-kalkinma.tr.mfa

[5] Z. Çeçen, F. Güvenç, "Assessment of climate change and global warming in terms of public health," SDÜ Journal of Health Management, vol. 4, no. 1, pp 14-25, 2022.

[6] S. Paleari, "The impact of the european green deal on EU environmental policy," The Journal of Environment & Development, vol. 31, no.2, pp. 196-220, 2022.

[7] H. SilvaHyldmo, S.A. Rye, D. Vela-Almeida, "A globally just and inclusive transition? Questioning policy representations of the European Green Deal," Global Environmental Change, 89, 102946, 2024.

[8] O. Koksal, "Evaluation of university campuses in terms of sustainability: The Example of Ondokuz Mayıs University," Ph.D. Dissertation. On Dokuz Mayıs University, Samsun, Turkey, 2022.

[9] S. N. Barlak, "Treatment of endocrine disrupting chemicals and sustainability in the context of the european green deal: A review in water resources," M.S. Dissertation, Bursa Teknik Univesity, Bursa, Turkey, 2024.

[10] IPCC, Climate Change, "The physical science basis contribution of working group i to the sixth assessment report of the intergovernmental panel on climate change," 2021. [Online]. Available: https://www.ipcc.ch/report/ar6/wg1/

[11] V. A. Yavuz, "Concept of sustainability and sustainable production strategies for business practices," Journal of the Institute of Social Sciences, vol. 7, no. 14, pp. 63-86, 2010.

[12] R. Raman, H. Lathabhai, D. Pattnaik, C. Kumar, P. Nedungadi, "Research contribution of bibliometric studies related to sustainable development goals and sustainability," Discover Sustainability, vol. 5, no. 1, 7, 2024.

[13] N. K. Arora, I. Mishra, "United Nations sustainable development goals 2030 and environmental sustainability: Race against time," Environmental Sustainability, vol. 2, no. 4, pp. 339-342, 2019.

[14] L. Chen, G. Msigwa, M. Yang, A. I. Osman, S. Fawzy, D. W. Rooney, P. S. Yap, "Strategies to achieve a carbon neutral society: A review," Environmental Chemistry Letters, vol. 20, no. 4, pp. 2277-2310, 2022.

[15] A. Al Mamun, M. A. Uddin, M. A. S. Shohag, M. M. Bappy, A. Talukder, "Energy consumption modeling in industrial sewing operations: A case study on carbon footprint measurement in the apparel industry," Manufacturing Letters, vol. 41, pp. 1635-1644, 2024.

[16] P. Pathak, S. Sharma, S. Ramakrishna, "Circular transformation in plastic management lessens the carbon footprint of the plastic industry," Materials Today Sustainability, vol. 22, 100365, 2023.

[17] M. M. Dam, A. Durmaz, F. V. Bekun, A. K. Tiwari, "The role of green growth and institutional quality on environmental sustainability: A comparison of CO_2 emissions, ecological footprint and inverted load capacity factor for OECD countries," Journal of Environmental Management, vol. 365, 121551, 2024.

[18] J. H. Pratama, Z. Rahmawati, A. R. Widyanto, T. Gunawan, W. N. W. Abdullah, N. L. A Jamari, H. Fansuri, "Advancements in green diesel production for energy sustainability: A comprehensive bibliometric analysis," RSC advances, vol. 14, no.48, pp. 36040-36062, 2024.

[19] K. Fardnia, H. Yousefi, M. Abdoos, "A bibliometric analysis of carbon and water footprints in renewable energy: The post-COVID-19 landscape," Green Technologies and Sustainability, 100162, 2024.

[20] Y. Zhao, Z. Yang, J. Niu, Z. Du, C. Federica, Z. Zhu, M. Emmanuel, "Systematic analysis of sludge treatment and disposal technologies for carbon footprint reduction," Journal of Environmental Sciences, vol. 128, pp. 224-249, 2023.

[21] Y. Zhang, K. Huang, Y. Yu, B. Yang, "Mapping of water footprint research: A bibliometric analysis during 2006–2015," Journal of Cleaner Production, vol. 149, pp. 70-79, 2017.

[22] M. S. I. Sarker, I. Bartok, "Global trends of green manufacturing research in the textile industry using bibliometric analysis," Case Studies in Chemical and Environmental Engineering, vol. 9, 100578, 2024.

[23] M. Shabir, P. Pazienza, C. De Lucia, "Energy innovation and ecological footprint: Evidence from OECD countries during 1990–2018," Technological Forecasting and Social Change, vol. 196, 122836, 2023.

[24] Q. Liu, S. Wang, R. Ma, F. Huang, J. Li, S. Ye, Y. Guo, "Comparative analysis of forest soil carbon sink and source based on bibliometrics: Development, hotspots, and trends," Journal of Cleaner Production, 144106, 2024.

[25] H. Ospina-Mateus, L. Marrugo-Salas, L. C. Castilla, L. Castellón, A. Cantillo, L. M. Bolivar, R. Zamora-Musa, "Analysis in circul are conomy research in Latin America: A bibliometric review," Heliyon, e19999, 2023.

[26] R. Rinanda, Y. Sun Y, K. Chang, R. Sulastri, X. Cui, Z. Cheng, B. Yan, G. Chen, "Plastic waste management: A bibliometric analysis (1992–2022)," Sustainability, vol. 15, 16840, 2023.

[27] N. J. Van Eck, L. Waltman, R. Dekker, J. Van den Berg, "An experimental comparison of bibliometric mapping techniques," In The 10th International Conference on Science and Technology Indicator, Vienna University, pp. 45-48, 2008.

[28] M. Artsın, "A text mining application: Vosviewer," Eskişehir Technical University Journal of Science and

Technology B-Theoretical Sciences, vol. 8, no. 2, 344-354, 2020.

[29] D. Mukherjee, W. M. Lim, S. Kumar, N. Donthu, "Guidelines for advancing theory and practice through bibliometric research," Journal of Business Research, vol. 148, pp. 101-115, 2022.

[30] K. H. Lee, B. Min, "Green R&D Foreco-innovation and its impact on carbon emission sand firm performance," Journal of Cleaner Production, vol. 108, pp. 534-542, 2015.

[31] Regulation (EU) 2023/956 of The European Parliament and of The Council Establishing a carbon border adjustment mechanism, May. 10, 2023. [Online]. Available: https://eur-lex.europa.eu/eli/reg/2023/956/oj

[32] X. Xu, X. Gou, W. Zhang, Y. Zhao, Z. Xu, Z. "A bibliometric analysis of carbon neutrality: Research hotspots and future directions," Heliyon, 2023.

[33] S. Khanra, A. Dhir, P. Kaur, M. Mäntymäki, "Bibliometric analysis and literatüre review of ecotourism: Toward sustainable development," Tourism Management Perspectives, vol. 37, 100777, 2022.

[34] Y. Gedik, "Sustainability and sustainable development with social, economic and environmental dimensions," International Journal of Economics Politics Humanities and Social, vol. 3, no. 3, pp. 196-215, 2020.

[35] World Commission on Environment and Development, Our Common Future. Oxford: Oxford University Press. s. 27. ISBN 019282080X, 1987.

[36] United Nations, "United Nations: Sustainable Development Goal: UN Climate Change Conference Paris," 2015, [Online]. Available: https://www.un.org/sustainabledevelopment/cop21

[37] F. Çayırağası, S. Sakıcı, "Sustainable Digital Marketing Strategies in the Perspective of the European Green Deal and the United Nations Sustainable Development Goals," Gaziantep University Journal of Social Sciences, vol. 20, no. 4, pp. 1916-1937, 2021.

Investigation of Inhibition Effect on Pathogen Microorganisms by Adding NPAg to Activated Carbon Obtained by Activating Hazelnut Shell with ZnCl₂

Birsen Sarıcı[1] iD, Esra Altıntığ[2*] iD, Şükrü Karataş[2] iD

[1] Düzce University, Faculty of Health Sciences, Department of Nutrition and Dietetics, Düzce, Türkiye, birsensarici@duzce.edu.tr, ror.org/04175wc52
[2] Sakarya University of Applied Sciences, Pamukova Vocational School, Department of Chemistry and Chemical Processing Technologies, Sakarya, Türkiye, altintig@subu.edu.tr, ror.org/01shwhq58
[3] İstanbul Aydın University, Faculty of Engineering, Department of food Engineering, İstanbul, Türkiye, sukrukaratas@aydin.edu.tr, ror.org/00qsyw664
*Corresponding Author

ARTICLE INFO

ABSTRACT

In this study, silver-coated activated carbon (NPAgAC) was obtained by adding nanoparticle silver (NPAg) to activated carbon (AC) produced from hazelnut shells by chemical activation and carbonization. SEM, FT-IR, and BET were evaluated. While the methylene blue (MB) number of the produced ACs was 490-499 mg/g, the MB numbers of NPAgAC were determined to be 421-453 mg/g. The iodine number of ACs was specified in the 1047-1612 mg/g range. The iodine numbers of NPAgACs were recorded in the 934-1022 mg/ g range. Additionally, EDS and XRD analyses were performed on all samples. Well, diffusion and spreading plate methods were used to control the antimicrobial properties of the produced NPAgAC. The study used Escherichia coli (*E. coli*) and Staphylococcus aureus (*S. aureus*) as pathogenic microorganisms. In addition, the antimicrobial properties of NPAgACs were investigated using the spread plate method at various times and temperatures to determine their effectiveness in inhibiting *the growth of E. coli in* polluted waters. Studies have shown that hazelnut shells are a suitable starting material for producing activated carbon, and that NPAgAC exhibits high antimicrobial properties with food safety.

1. Introduction

As the global population is expected to reach 9.7 billion by 2050, concerns about food security are also on the rise [1]. Industrialization has also intensified water and environmental pollution, posing risks to public health and food safety [2]. Traditional methods and chemical preservatives are widely used to prevent food spoilage and control pathogens [1]. Although effective, the prolonged use of these chemicals has led to the accumulation of residues and the development of microbial resistance [2]. This has driven interest in safer, natural alternatives to conventional preservatives [3]. To mitigate existing water pollution without harming human health, developed countries are focusing on utilizing agricultural waste as a source of biomass. This approach offers sustainable solutions to both waste management and water pollution prevention [4].

Activated carbons are substances with high adsorbent capacity produced by several special methods to obtain a larger surface area from various biomass and carbon-based materials [5]. Producing activated carbon from agricultural biomass waste, a low-cost raw material, has become increasingly common [3]. Biomass is a ubiquitous, low-cost, regularly produced

substance that does not pose a problem for a renewable environment [6]. Activated carbons are accepted as effective adsorbents for removing chemical pollutants in water due to their large surface area and highly porous structure [5]. However, activated carbons should possess bactericidal properties, depending on the location of use, as they can promote bacterial growth due to bacterial contamination, particularly in terms of biological compatibility with microorganisms [7].

Most nanoparticle atoms are unsaturated on the surface and, therefore, can easily bind to other atoms [8]. While the antibacterial effects of silver have been recognized since ancient times, the use of nanoparticulate silver (NPAg) in various applications has become increasingly common in recent years, owing to its antimicrobial properties and large surface area [9, 10]. Many nanomaterials, such as silver, have gained popularity in recent years, particularly for addressing the issue of antibiotic resistance and providing more economically sustainable public health conditions [11]. It attracts great attention due to its low toxicity [12]. Although the mechanisms underlying various morphological and structural changes caused by silver metal, silver ions, or NPAg ions in the cell walls of microorganisms are not yet fully understood, studies on this subject continue [11]. NPAg ions are thought to exert their antibacterial effect by binding to the bacteria's cell wall and cell membrane. It is believed that hydrogen cations alter this effect after they combine with functional thiol (-SH) groups in the proteins in the wall, deactivating them and reducing their permeability in the cell membrane, thereby causing the death of microorganisms [13, 14]. NPAg ions are preferred as antibacterial and antifungal due to their antimicrobial effects against fungi and bacteria [15, 16].

In the twenty-first century, as the world grapples with the climate change crisis, environmental pollution and wastewater management are among the most pressing problems [2]. Water is indispensable for all living things, and waste

from various industries, including textiles, food, health, and paper, pollutes water [3]. Efficient methods continue to be researched to remove substances that threaten the health of living things, such as pesticides, heavy metals, and dyestuffs, from wastewater [4]. Binding NPAg to activated carbon, which has a high adsorbent capacity, provides a vital solution for achieving antibacterial properties, reducing water pollution, improving food safety, and enhancing public health [8]. With its large surface area and varied pore sizes, activated carbon can be an excellent support material for NPAg [17].

This research focuses on the production of activated carbon using hazelnut shells, an agricultural waste material with an estimated annual yield of around 550,000 tons in Turkey. Approximately 50% of the total mass of harvested hazelnuts consists of shells. Despite their high carbon content, these shells are not sufficiently utilized as raw materials, posing a challenge to environmental sustainability [18]. Hazelnut shells, as a form of biomass, contain cellulose, hemicellulose, and lignin in varying proportions, making them a promising precursor for the production of activated carbon. Elemental analysis of lignocellulosic biomass has revealed an average carbon content of approximately 50%, indicating its value as a biomass feedstock [19]. Therefore, due to the favorable composition of its biocomponents, the production of activated carbon from hazelnut shells presents a viable solution for managing and disposing of agricultural waste, addressing an environmental concern, and generating a high-value product [20]. For this purpose, hazelnut shell was selected in our study.

For this purpose, the collected hazelnut shells were first purified through various pre-treatments. Washed and dried hazelnut shells were ground and separated into three mesh sizes (50-70-150). Samples chemically activated with $ZnCl_2$ in 3 different ratios (1:1, 1:2, 1:3) were carbonized in a tube furnace at 700 °C, and the produced activated carbons were stocked for characterization studies. The characterization

studies selected the activated carbon with the best efficiency.

Additionally, it seeks to enhance the properties of the produced activated carbon by incorporating NPAg to impart antimicrobial properties, offering a potential solution for inhibiting pathogens that threaten public health. NPAg was added to the best-activated carbon, as determined by SEM, FT-IR, and BET images, to enhance the antimicrobial effect. The Well diffusion method was used to test the antimicrobial effect of the obtained NPAgAC on *E. coli* and *S. aureus*, two pathogenic microorganisms.

2. General Methods

2.1. Materials and methods

The hazelnut shell samples used in this study were obtained at the end of the 2019 harvest season by mixing samples from merchant warehouses in the Giresun region with sample soda from six different points, according to TSE 3074 standards, and breaking the hazelnut kernels apart. The study utilized chemicals, including sodium alginate, $ZnCl_2$, $AgNO_3$ (purity > 99%), HCl, sodium hydrazine monohydrate, and NaOH, all sourced from Merck (Germany). All chemicals are analytical reagent grade.

Then, activated carbon production was completed with chemical activation and carbonization stages. The produced activated carbon was characterized, and antimicrobial studies were carried out.

2.2. Materials

In this research, all mixing operations were performed using a Wisestir MSH-20A magnetic stirrer. The materials were accurately weighed using a Precisa XB 220A analytical balance, and pH values were determined with a Mettler TOLEDO Seven Compact series pH meter. The carbonization of the activated carbon was conducted in a Proterm PTF 12 tubular furnace. A Nuve NS112 device supplied pure water for the experiments. Shaking processes were conducted with a Nuve SL 350 shaker, and drying operations were performed using a Mido/2/AL brand oven. The determination of ash and moisture contents, along with wet chemical analyses, was carried out using a Nuve MF 100 drying oven.

Functional groups in HS, AC, and NPAgAC samples were identified using Fourier Transform Infrared Spectroscopy (FT-IR), performed on a PerkinElmer UATR-TWO instrument, covering the spectral range of 4000 to 400 cm^{-1}. The crystalline phases of AC and NPAgAC were examined using an X-ray diffractometer (XRD, Rigaku). Surface topography was investigated by a scanning electron microscope (SEM, Jeol JSM-6060 LV model). Specific surface area (m²/g), pore diameter (nm), and volumes of micropores and meso-/macropores (cm³/g) were assessed via multi-point Brunauer–Emmett–Teller (BET) analysis. Nitrogen adsorption measurements for pore structure and surface area evaluations were conducted using a Micromeritics ASAP 2020 analyzer under liquid nitrogen conditions at 77 K. Furthermore, MB adsorption experiments were analyzed with a Shimadzu UV-2600 UV-Visible spectrophotometer.

2.3. Production of activated carbon

Hazelnut shells taken after harvest were washed with tap and distilled water to purify them from impurities. They were dried at room temperature for 3 days and then in an oven at 60 °C for 3 days. For sizing, a mixer and a pulse mill were used in the grinding stage, and the material was sieved into three different mesh ranges (50, 70, and 150). The hazelnut shells were mixed with $ZnCl_2$, which was identified as a chemical activating agent, in three different ratios: 1:1, 1:2, and 1:3. After impregnating the ground hazelnut shells with $ZnCl_2$, they were shaken at 200 rpm for 24 h in a shaking incubator at 40°C for activation. In the next step, the excess of the chemical substance was filtered from the dense solution, and the samples were kept open at room temperature for one day under laboratory conditions.

The filtered mixtures were dried in an oven at 103 °C for 12 h. The samples were carbonized in a tube furnace at 800°C in a nitrogen atmosphere (flow rate, speed = 200 mL/min) with a heating rate of 10°C/min. At the end of the carbonization period, nitrogen flow continued until the furnace temperature dropped to 60 °C (approximately 24 h). To remove the $ZnCl_2$ from the activated carbon, it was first washed with 1 M HCl and then with distilled water until the pH reached 7. It was then allowed to dry in a 105°C oven for 12 h by filtration. Efficiency calculations were performed on the activated carbons obtained.

2.4. Production of NPAg and impregnation on AC

This study employed $AgNO_3$ as the precursor for the synthesis of NPAg. Solid $AgNO_3$ was dissolved in 100 mL of 25% by weight NH_3 at two different concentrations (0.5 g and 1 g). To achieve a homogeneous mixture, the solution was stirred at 150 rpm for 1 h at ambient temperature (298 K) using a magnetic stirrer. The synthesized diammine silver nitrate ($[Ag(NH_3)_2]NO_3$) solution was then placed into amber glass containers shielded with aluminum foil to protect from light exposure. The pH was adjusted to 9.0 using a nitric acid (HNO_3) solution. [2] The resulting NPAg solution was stored in light-proof containers wrapped with aluminum foil. Meanwhile, activated carbon (1g:1g) was prepared by combining it with sodium alginate (Sigma Aldrich) and stirring magnetically at 200 rpm for 60 min at room temperature.

While the biamin silver nitrate solution was prepared with a mixture of sodium alginate and activated carbon obtained in a three-necked glass balloon wrapped with aluminum foil, the solution was mixed simultaneously. Hydrazine monohydrate was then dripped sufficiently from the other neck with the help of a dropper. This study was conducted in an inert atmosphere under a nitrogen gas flow of 200 min/mL. The suspension was continuously agitated on a magnetic stirrer at ambient temperature for 4 hours under a steady flow of nitrogen gas. Subsequently, the obtained mixtures were subjected to filtration, rinsed sequentially with ethanol and deionized water, and then dried in a laboratory oven at 60°C for 12 h [21]. This process represents the reduction of Ag^+ ions to Ag^0 using hydrazine monohydrate as a reducing agent. In this study, chemical activation with $ZnCl_2$ was performed, and NPAgACs were produced by adding 1:0.5 and 1:1 ratios of $AgNO_3$ to activated carbons (ACs) carbonized at 700°C.

2.5. Characterization of produced AC and NPAgACs

Moisture, ash, and volatile matter determinations were made for the three mesh sizes, with the best efficiency of 12 different ACs for efficiency calculations. FT-IR analysis was conducted in the 4000–400 cm^{-1} range to identify the functional groups in the HS, AC, and NPAgAC samples. The crystalline structures of AC and NPAgACs were examined using XRD analysis. SEM imaging was utilized to investigate the surface morphology of the samples. Surface characteristics including specific surface area (m^2/g), average pore diameter (nm), and the volumes of micro-, meso-, and macropores (cm^3/g) were evaluated through a multi-point Brunauer–Emmett–Teller (BET) analysis. The adsorption capacity was assessed using the iodine number method, a crucial technique for detecting micropores. The iodine number of activated carbon was determined using the sodium thiosulfate volumetric method, expressed in milligrams of iodine per gram of activated carbon [22, 23].

MB adsorption is a key analysis for evaluating the high porosity of AC. For this purpose, a 100 mg/L MB solution was prepared. Then, 0.1 g of AC was weighed, and 100 mL of the 100 mg/L MB solution was added. The mixtures were then agitated in an orbital shaker for 6 h. The obtained mixture was centrifuged at 1200 rpm, and samples were taken from the homogeneous supernatant, which was then measured using a UV-Vis spectrophotometer. The MB number of ACs was determined by calculating the adsorption capacity of the ACs.

2.6. Antimicrobial analysis of NPAg coated activated carbon (NPAgAC)

Well, the diffusion method was used to determine the antimicrobial effects of the prepared NPAgACs. In this study, two different pathogenic bacteria (*E. coli* and *S. aureus*) and two different antibiotic discs (Ampicillin 10 mg and Cefotaxime, used as the control) were employed. Stock bacterial cultures were transferred to a non-selective medium (PCA) and incubated at 36.5°C for 24 h. After incubation, isolated colonies were selected, and an inoculum was prepared. A ready-made saline solution was used to create the inoculum suspension. All experimental steps were conducted under a burner flame to ensure aseptic conditions and uphold proper sterilization protocols.

Several bacterial colonies with similar morphology were collected using a sterile cotton swab and suspended in a sterile saline solution (0.85% NaCl). The suspension density was adjusted to match the McFarland 0.5 standard, corresponding to approximately $1\text{-}2 \times 10^8$ CFU/mL of *E. coli*, using the Thermo Multiscan Go photometric device at a wavelength of 625 nm. Using a sterile cotton swab, the inoculum suspension was evenly spread across the agar surface in three directions. Following the EUCAST disc diffusion guidelines, the Petri dish was divided into equal sections, and wells with a diameter of 6 mm were created in each marked area using a sterile cork borer. Precisely weighed 10 mg of NPAgACs were placed into the prepared wells. On the other hand, the antibiotic discs used for antibiotic susceptibility comparison were placed on the agar surface and incubated at 36.5°C for 24 h. The results were classified as 'susceptible,' 'resistant,' or 'intermediate' for a given antibiotic based on the EUCAST disk diffusion breakpoint tables [24].

2.7. Time-dependent inhibition study of E coli using NPAgAC

To evaluate the adequate contact time and ideal temperature for NPAgACs in eliminating E. coli from potable water, the smear plate technique was employed. All procedures were performed within a sterile laminar flow cabinet and under flame to maintain aseptic conditions. The bacterial suspension was standardized to an optical density of 625 nm, corresponding to the 0.5 McFarland standard (approximately 10^8 CFU/mL of E. coli). From this suspension, a 1 mL aliquot was withdrawn and further diluted by transferring it into 10 mL of sterile saline solution [25]. This process was repeated 3 times, corresponding to approximately $1\text{-}2 \times 10^5$ CFU/mL of *E. coli*. Then, 20 mg of NPAgAC2 was added to 10 mL of 10^5 CFU/mL suspension and incubated in a 150 rpm shaker at room temperature in an oxygenated environment, ensuring that no Ag-AC granules precipitated. The first moment of mixing, respectively, was assumed to be zero.

Subsequently, 0.1 mL of the diluted sample was transferred onto PCA medium at 10-minute intervals and evenly spread across the surface of the Petri dishes using a sterile disposable Drigalski spatula to achieve uniform distribution. The inoculated plates were prepared at four different temperature settings (20, 25, 30, and 35 °C) and assessed at three distinct exposure times (5, 10, and 15 minutes). All plates were incubated at 37 °C for 24 h, after which bacterial growth was quantified through colony counting, following the methodology outlined in references [26, 27].

The formula (1) below calculates the number of viable microorganisms, considering the dilution before sowing (1).

$$\frac{(CFU)}{\text{mL}} = \frac{(number\ of\ colonies)\ x\ (dilution\ factor)}{culture\ plate\ volume} \quad (1)$$

3. Results and Discussion

3.1. Preliminary analysis results for hazelnut shell and activated carbon

$ZnCl_2$ was used as a chemical activation agent in this study because it is a frequently preferred chemical for producing activated carbon with a high surface area, is relatively inexpensive, and has a low carbonization temperature [28]. In the study, Activated carbons impregnated with HS, AC1 (50 mesh 1:1 $ZnCl_2$, AC2 (70 mesh 1:2 $ZnCl_2$), AC3 (150 mesh 1:3 $ZnCl_2$), and NPAg in two different ratios (0.5-1g) are encoded as NPAgAC1 and NPAgAC2. The experimental

results were determined by averaging the data from three repeat studies.

Upon examining the results of Table 1, the moisture content of the untreated hazelnut shell was calculated to be 6.05%. Upon reviewing the table, it was found that the hazelnut shells used in the study had a low ash content (1.64%), high volatile matter (71.1%), and a substantial fixed carbon content (21.21%). Raw materials with low ash content, high volatile matter, and high fixed carbon are preferred for producing activated carbon. A review of the literature shows that vegetable wastes with volatile matter content ranging from 20.40% to 67.36%, fixed carbon content between 17.62% and 70.70%, and ash content ranging from 0.3% to 5.0% are commonly used in activated carbon production [27, 29].

The literature indicates that the ash content of different biomass samples varies in the range of 0.1-38% [6, 30]. Compared to the literature, it has been observed that hazelnut shells can serve as a suitable starting material for the preparation of activated carbon, which can be used as an adsorbent due to their low ash content [31]. When the moisture, ash, and volatile matter content of the activated carbons are examined, it is found that the values fall within the ranges of 1.89% to 3.1%, 1.1% to 1.4%, and 4.8% to 7.3%, respectively. It is suitable for producing activated carbon in every mesh range of hazelnut shells with low ash content [30]. It is known that pores are formed in the structure of activated carbon due to the effect of the activation agent used, and a significant portion of the existing ash content of the activated carbon is removed from the structure after production [30, 31]. The ash content may be higher in activated carbons, in which $ZnCl_2$, which has a micropore size, is the agent due to the possibility of the inorganic structure being trapped in these pores [32]. The results are consistent with studies on producing activated carbon from hazelnut shells [33, 34]. Table 2 shows the elemental analysis results for HS, AC1, AC2, and AC3.

Table 1. Activated carbon proximate analysis results

(dry basis (%))	HS	AC1	AC2	AC3	Method
Yield	-	43	40	37	-
Moisture	6.05	1.89	2.2	3.1	ASTM D 2016 2.67
Ash	1.64	1.4	1.8	1.1	ASTM D1102 0.17
Volatile Matter	71.1	7.3	6.2	4.8	ASTM E 872 78.50
Fixed carbon	21.21	89.41	89.8	91	By difference

Table 2. HS and AC elemental analysis results (LECO Instruments, USA)

Raw Material Name	%C	%H	%N	%S	%O*
HS	49.348	6.0992	0.36148	0,048	44.144
AC1	64.244	2.225	0.658	0.043	32.893
AC2	70.240	0.815	0,482	0.002	28.461
AC3	69.583	0.196	0.721	0.004	29.496

As seen in Table 2, when HS is converted into activated carbon, the C content increases while the O content decreases. This result is considered quite successful for all three samples.

3.2. Characterization results of AC and NPAgACs

The number of Iodine and MB, SBET, t-plot Micropore, t-plot, Vtotal, Vmicro, and Average pore size (Å) for AC1, AC2, AC3, NPAgAC1, NPAgAC2 are determined, and the results are given in Table 3.

When the results in Table 3 were examined, the MB values obtained for three activated carbons were 490-499 mg/g. It was observed that the mesopores of the produced ACs played a vital role in the adsorption of large adsorbate molecules, including dye molecules [32]. The study observed that $ZnCl_2$, a preferred chemical activation agent, is highly successful in activating the raw material. In the study, the results of the iodine number analysis, performed to investigate the adsorption of small molecules onto AC, were found to be in the range of 1142-1612 mg/g. The iodine number of NPAgACs decreased to 934–1022 mg/g due to the reduction in pore volume and surface area caused by the

binding of silver (Ag) particles. When Ag nanoparticles are incorporated into the activated carbon structure, they tend to occupy or block some of the micropores, which are primarily responsible for iodine adsorption. As a result, the overall accessibility of these micropores to iodine molecules diminishes, leading to a lower iodine number [34, 35]. This decline indicates a reduction in the material's adsorption capacity for small molecules like iodine, which is often used as an indicator of microporosity. These results showed parallelism with the BET surface area.

Many other researchers have obtained similar results to those presented here, demonstrating a parallel relationship between the BET surface area and the iodine number [34- 36]. Based on the IUPAC classification, pores larger than 500 Å are called macropores, pores ranging from 500 to 20 Å are considered mesopores, and pores smaller than 20 Å are categorized as micropores. This study observed that three activated carbons had a mesoporous structure with a pore size of 21-25Å [37, 38]. In addition, when the BET surface areas were evaluated for three different mesh sizes in the study, the highest surface area was observed in the 150-mesh size in AC3, confirming the increase in surface area as the particle size decreased [39]. The decrease in the MB, Iodine, and BET surface area of NPAgACs is related to the attachment of NPAg ions to the surface area and is an expected result. The decrease in surface area, especially, proves that activated carbon adsorbs NPAg ions. An increase in surface area was observed in only one sample, which was attributed to the increased porosity in the structure resulting from the process performed in an inert atmosphere during the impregnation of NPAg ions into the activated carbon [37].

3.3. SEM and EDS results of AC and NPAgACs

In Figure 1, AC1 (50 mesh 1:1 $ZnCl_2$), AC2 (70 mesh 1:2 $ZnCl_2$), and AC3 (150 mesh 1:3 $ZnCl_2$)

are shown. The SEM and EDS images indicate that the EDS images exhibit amorphous structures resembling the typical honeycomb-activated carbon morphology, with well-developed porous textures and irregular surface features.

As for the SEM images of Figure 1. a) AC1, b) AC2, and c) AC3 are examined at 1000x magnification. It is observed that the surface structure has undergone significant changes, resulting in a porous structure, after the raw material was chemically activated with $ZnCl_2$ and carbonized at high temperatures in a N_2 atmosphere. When the EDS results are examined, it is seen that the carbon ratio in the structure increases as the raw material size decreases. The amount of carbon in the raw material, which is approximately 45% on average, rises to 81% after chemical activation and carbonization, indicating that most of the oxygen, hydrogen, and volatile substances in the structure are removed during these processes.

The particle size of the raw material affects the pore structure and pore volume of the activated carbon produced. It is stated that when working with small particle sizes, large surface areas and pore volumes are obtained [21]. As the raw material's particle size decreased, the porous structure and the carbon content increased significantly. This indicates that the smaller particle size enables better interaction and more efficient impregnation of the chemical substance into the raw material, thereby enhancing the overall surface area and porosity of the material. The improved impregnation process ensures better incorporation of the active component, which is essential for achieving the desired properties in the final material.
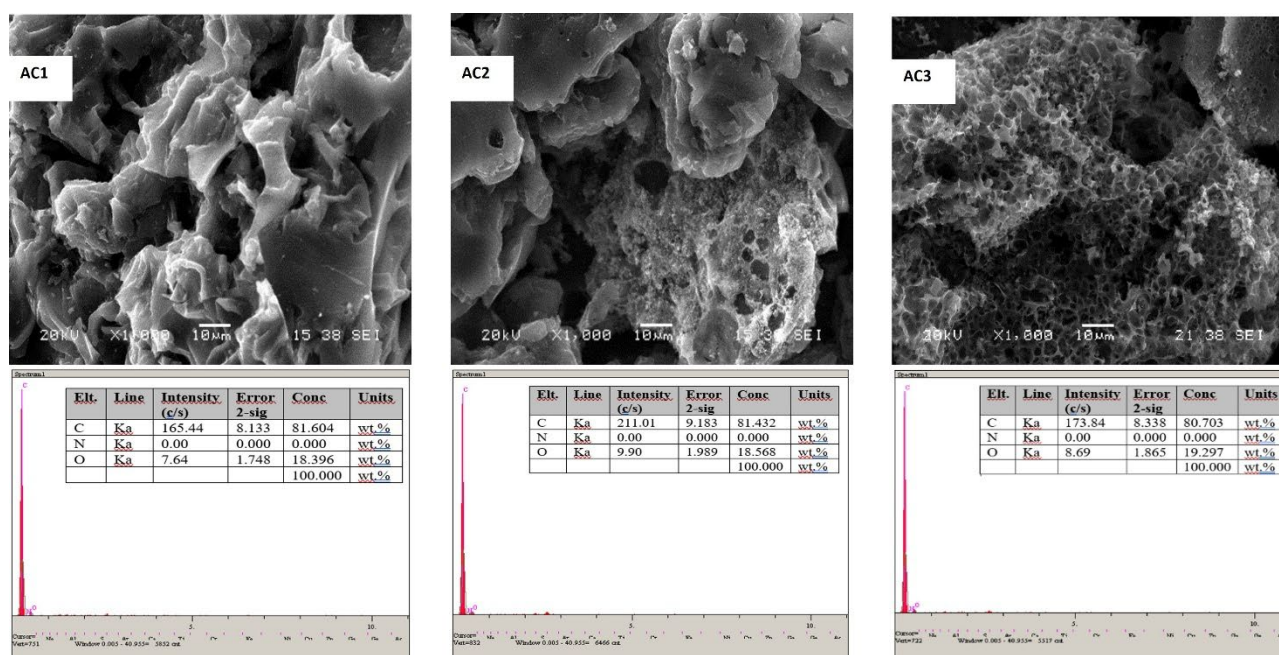
AC1

Elt.	Line	Intensity (c/s)	Error 2-sig	Conc	Units
C	Ka	165.44	8.133	81.604	wt.%
N	Ka	0.00	0.000	0.000	wt.%
O	Ka	7.64	1.748	18.396	wt.%
				100.000	wt.%

AC2

Elt.	Line	Intensity (c/s)	Error 2-sig	Conc	Units
C	Ka	211.01	9.183	81.432	wt.%
N	Ka	0.00	0.000	0.000	wt.%
O	Ka	9.90	1.989	18.568	wt.%
				100.000	wt.%

AC3

Elt.	Line	Intensity (c/s)	Error 2-sig	Conc	Units
C	Ka	173.84	8.338	80.703	wt.%
N	Ka	0.00	0.000	0.000	wt.%
O	Ka	8.69	1.865	19.297	wt.%
				100.000	wt.%

Figure 1. SEM images of a) AC1, b) AC2, c) AC3 at 1000x magnification

3.4. NPAgAC1 and NPAgAC2 SEM and EDS results

Figure 2 shows SEM and EDS images of NPAgAC1 and NPAgAC2. The bright silver appearance is remarkable after NPAg binds to the active carbon. The SEM images (Figure 2), NPAgAC1 and NPAgAC2, were obtained by impregnating two different amounts (0.5-1g) of NPAg on 50 mesh AC1, whose chemical activation was performed at a 1:1 ratio with $ZnCl_2$. It is seen that the silver particles are bright and dispersed on the surface of the activated carbon. When the images are compared, a) 0.5 g NPAg is added in NPAgAC1 and less, b) NPAgAC2 silver ions are seen more brightly because 1 g NPAg is impregnated into the structure. It was observed that the ACs we obtained bind NPAg at a high rate due to their porous structure and high surface area. The EDS analyses further confirm the presence of silver at the elemental level, consistent with the SEM observations.

These findings align well with previously reported literature, which similarly emphasizes the affinity of activated carbon for incorporating metal nanoparticles due to its textural properties and surface chemistry [40, 41].
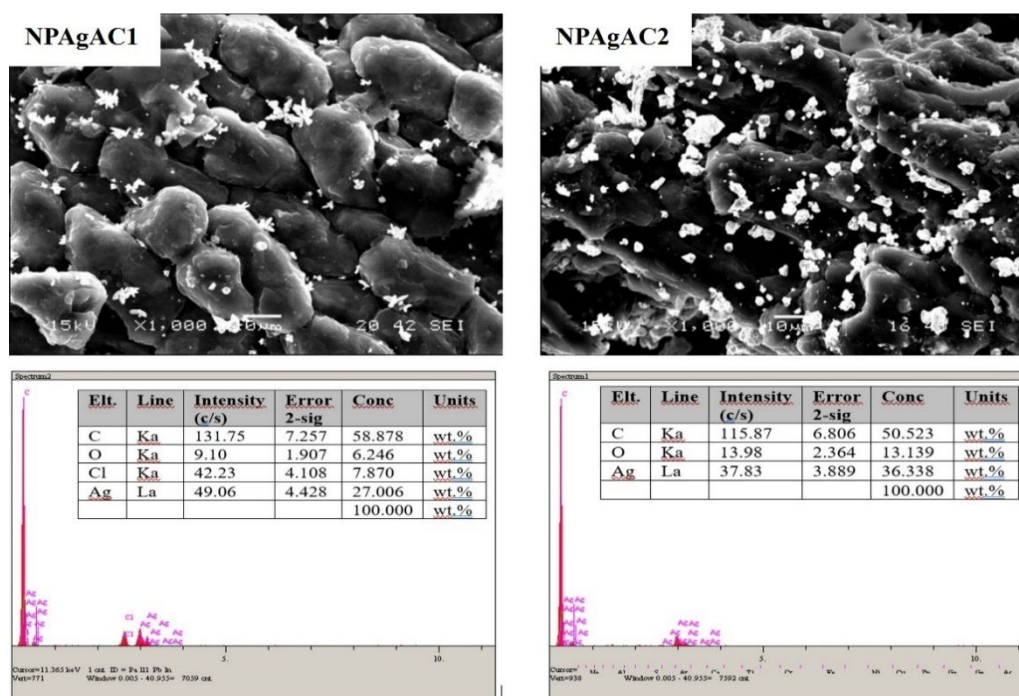
Figure 2. SEM images of a) NPAgAC1, b) NPAgAC2, at 1000x magnification

When the EDS (Figure 3) analyses of the samples were compared at 1000x magnification, the carbon ratio in AC1 was 81%, while it decreased to 58% in NPAgAC1 and 50% in NPAgAC2. This is because of the increase in Ag^+ ions bound to the structure. The amount of silver in the structure increases linearly as the amount retained on the surface increases.

3.4. AC1, AC2 and AC3 XRD results

Figure 3 below shows the XRD images for AC1 (50 mesh, 1:1 $ZnCl_2$), AC2 (70 mesh, 1:2 $ZnCl_2$), and AC3 (150 mesh, 1:3 $ZnCl_2$). The images' typical amorphous structure and harmony prove that the study was done correctly.
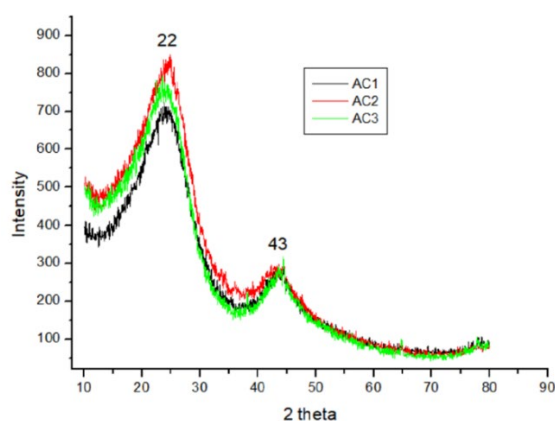

Figure 3. AC1, AC2 and AC3 XRD image

When the XRD results of AC1, AC2, and AC3, as shown in (Figure 4), are examined, it is evident that the synthesized activated carbons exhibit the same degree of spectrum across the three different mesh intervals. This indicates that the study was conducted precisely and the results are accurate. Results at 22° and 43°, with typical peaks at 2θ, indicate the amorphous structure of activated carbon. These broad peaks are typically attributed to the (002) and (100) planes of disordered graphitic carbon layers, indicating a lack of long-range crystalline order. Additionally, it was observed that the mesh size difference did not affect the amorphous structure of the activated carbon during production. These results are consistent with existing literature, which also reports similar broad peaks in chemically or thermally activated carbon materials, affirming their non-crystalline, highly porous nature [21].

3.5. NPAgAC1 and NPAgAC2 XRD results

The XRD images of NPAgAC1 and NPAgAC2 given in (Figure 4) showed that the study performed by overlapping the NPAg-bound ACs at two different rates was consistent in nanoparticle binding.
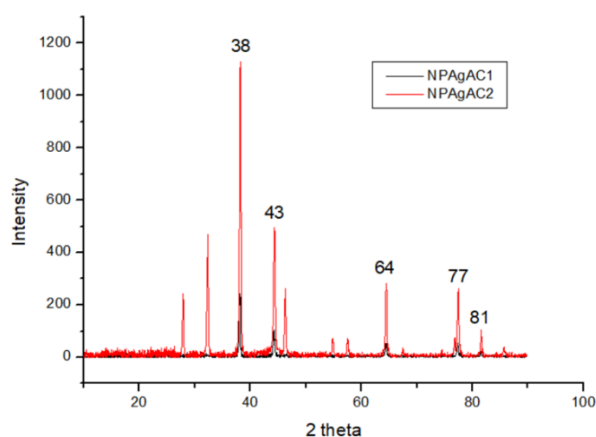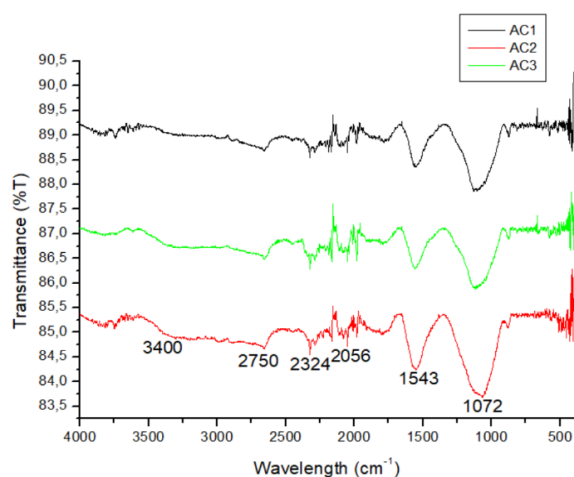
Figure 4. NPAgAC1 and NPAgAC2 XRD image

In Figure 4, the XRD analysis results for NPAgAC1 and NPAgAC2, as shown in the figure, are examined. Sharp peaks are observed at 2θ angles of 38°, 43°, 64°, 77°, and 81°. These peaks obtained as a result of the analysis belong to surface-centered metallic silver in the coordinates (111), (200), (220), (311), and (222). No silver oxide peaks were observed in the XRD results, which were supported by the literature [21, 42]. After adding silver, the amorphous structure of the activated carbons transformed into a crystalline structure, as indicated by the sharpness of the peaks.

3.6. AC1, AC2 and AC3 FT-IR results

Figure 5 shows FT-IR images for AC1 (50 mesh 1:1 $ZnCl_2$), AC2 (70 mesh 1:2 $ZnCl_2$), and AC3 (150 mesh 1:3 $ZnCl_2$). The harmony of the images proves that the study was done correctly.

When Figure 5 examines the IR spectra of activated carbon in three different mesh sizes obtained by $ZnCl_2$ activation of the raw material, it is observed that the results are very similar to each other within each mesh range. Upon examining the spectra, it was observed that the four significant peaks required evaluation and interpretation. The prominent ⁻OH stretch vibration peak at 3400 cm^{-1} in the hazelnut shell has disappeared. The structure's moisture is dehydrated during the activation agent chemicals and carbonization. Peaks between 2056 and 1543 cm^{-1} indicate the presence of carboxylic acid and/or lactone groups. The peak at 1072 cm^{-1} corresponds to the C-O stretching mode in the heterocyclic rings. The peaks between 2056 and 2750 cm^{-1} are the aliphatic C-H stretch. The stresses observed in the study are consistent with the typical image of activated carbon [43].

3.7. NPAgAC1 and NPAgAC2 FT-IR results

Figure 6 presents the FT-IR spectra of NPAgAC1 and NPAgAC2, obtained after incorporating NPAg into the produced activated carbon at two different rates. These spectra offer valuable insights into the structural and chemical modifications that occur on the activated carbon surface upon the addition of NPAg. The observed variations in functional groups and bonding characteristics further confirm the successful incorporation of NPAg at different concentrations, highlighting its potential impact on the material's physicochemical properties.


Figure 5. AC1, AC2 and AC3 FT-IR image
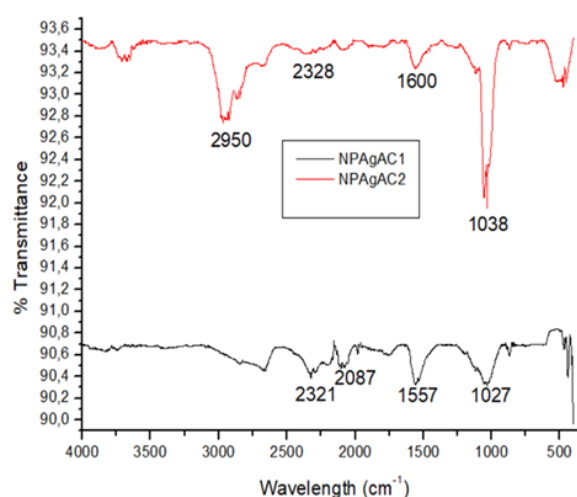
Figure 6. NPAgAC1 and NPAgAC2 FT-IR image

When Figure 6, the peak bands of the graph of NPAgAC1 and NPAgAC2 shown in (Figure 7) are 1027-1038 cm^{-1}, 1557-1600 cm^{-1}, 2328-2321 cm^{-1}, and 2950 cm^{-1} with the tensile vibration of C = C bending (alkene) peak bands such as amine groups (C-N), aromatic carbon-carbon double bonds (C = C), carbon dioxide bonds (O = C = O) and alcohol bond (O-H, strong intermolecular bond), strong carbon-carbon confirmed the formation of double bonds (aromatic and alkene bonds). Peaks at 2950 cm^{-1}, 1557-1600 cm^{-1}, and 1027-1038 cm^{-1} indicate that Ag+ ions combine with activated carbons through reduction [44, 45].

3.8. Antimicrobial results of NPAgACs

3.8.1. Well diffusion results

Figure 7 illustrates the wide zone diameters formed due to the antimicrobial well diffusion study conducted using NPAg-coated activated carbons. This study was carried out to evaluate the antimicrobial efficacy of the synthesized materials against two bacterial strains, *E. coli* and *S. aureus*.
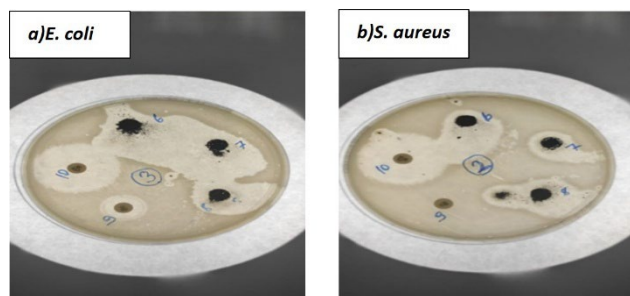
Figure 7. a) *E. coli* and b) *S. aureus* Zone diameters formed in the presence of NPAgAC and antibiotics

6) AC/NPAgAC 7) 0.5gNPAgAC 8) 1gNPAGgAC 9)10mg Ampicillin 10) 30mg Cefotaxim

S. aureus can be found as a part of the normal microbiota in the skin, upper respiratory tract, and intestinal mucosa of all warm-blooded animals, including humans. *S. aureus* is extremely important, as it is a pathogenic risk factor in respiratory tract infections and a significant concern in food safety. It is a microorganism with high mortality rates, especially in hospital infections with methicillin-resistant (MRSA) strains [46]. In our study, antibiotic resistance was confirmed, and the zone diameters (20-21 mm) observed in the Petri dishes indicated the effectiveness of the antimicrobial agent (Table 3). Consumption of water contaminated with *E. coli*, in particular, is one of the major causes of waterborne human infections [47]. Waterborne diarrheal disease causes 2 million deaths worldwide each year, mostly in children under 5 years of age [48]. *E. coli*, which is considered an indicator pathogen for drinking water, appears to be effectively inhibited by the NPAgAC produced in the study.

Table 3. Zone diameters measured for *E. coli and S. Aureus*

Sample	*S. aures*	*E. coli*
6)AC/NPAgAC	20 mm	20 mm
7)0.5gNPAgAC	18 mm	18 mm
8)1gNPAGgAC	21 mm	17 mm
9)10 mgAmpisilin	0 (18)*mm	11(14)*mm
10)30 mg Cefotaxim	30 mm	27 mm

The zone diameter difference between 0.5 g and 1 g is very low in NPAgACs, which act as actively as the third-generation cephalosporin group antibiotics used as the control group in the study (Table 3). This demonstrated that adding 0.5 g of NPAg has a sufficient effect in removing pathogenic bacteria, and there is no need to use more silver, which is an expensive product, especially in terms of cost.

3.9. Results of time- and temperature-dependent inhibition of NPAgAC2 classes of *E. coli*

Figure 8 shows the results of the smear plate method used to determine the inhibition of E. coli with the produced NPAgAC2 at different temperatures and at various time intervals.

Figure 8. Time- and temperature-dependent inhibition of *E. coli* in the presence of NPAgAC2

As seen in (Figure 9), since NPAgAC1 was added to the suspension diluted to approximately 1-2 x 10^5 CFU/mL E. coli by the Smear plate method and mixed, 0.1 ml samples were taken and planted in Petri dishes, the initial number of microorganisms was 1-2 x. 10^6 CFU/mL. Colony counts were performed in 12 Petri dishes after 24 hours of incubation at 36.5°C for bacteria cultivated at four different temperatures (20, 25, 30, and 35°C) and at three different time intervals (5, 10, and 15 minutes).

The Colony (*E. coli*) Count according to Time and Temperature is shown in Figure 10. In this study, which aimed to determine the effects of both time and temperature on the inhibition of microorganisms, the number of colonies and the logarithmic numerical expression of live microorganisms are presented in Figure 10. The analysis compared the number of colonies over time, specifically up to the 15th minute, for each experimental condition. In these experiments, an initial microbial concentration of approximately 1-2 × 10^6 CFU/mL was used across four different temperature settings. When the microbial counts were evaluated, it was observed that the most significant decrease in colony numbers occurred at 25°C, indicating that this temperature had the most potent inhibitory effect on microbial survival within the given timeframe.

Furthermore, when the correlation values were examined, it was found that the R² values were high for all tested temperatures, demonstrating a strong statistical relationship between time and microbial reduction. The consistently high R² values across different conditions suggest that the study's findings are reliable and that the

experimental methodology was appropriately designed to assess microbial inhibition. These results further emphasize the critical role of temperature in determining microbial viability over time and highlight the significance of understanding thermal inactivation patterns in microbial control applications.

Figure 11 shows the pattern of change in the growth (Log) of the starting microorganisms as a function of temperature and time.

When Figure 11 is examined, it is seen that the temperature-dependent inhibition of *E. coli* with an initial concentration of 10^6 CFU/mL increases over time. The death of microorganisms due to the effect of heat generally follows first-order reaction kinetics. In the first-order rate expression, the death rate is proportional to the current concentration of the component. Since the initial concentration is equal here, the effect of time on temperature was measured. When the results were examined, the correlation values were calculated as $R^2 = 0.9338$, $R^2 = 0.9541$, $R^2 = 0.9434$, and $R^2 = 0.9641$ for temperatures of 20, 25, 30, and 35 °C, respectively. The highest correlation and activation value was observed at 35 °C. It has been seen in.

As illustrated in Figure 11, the initial D-values of microorganisms tend to vary significantly depending on both temperature and exposure duration. This observed variation underscores the significant role of environmental conditions, particularly heat, in influencing microbial resistance and survivability. As the temperature increases, the D-value generally decreases, indicating that microorganisms become less resistant to thermal treatment. Conversely, at lower temperatures, higher D-values suggest a greater tolerance to heat, requiring longer exposure times to achieve the same level of microbial reduction. The relationship between D-value, temperature, and time provides valuable insights into optimizing thermal treatment processes for microbial control applications.

The textural characteristics, MB adsorption capacities, and iodine numbers of the synthesized

activated carbon and its silver-loaded derivatives (NPAgACs) are comprehensively summarized in Table 4 to evaluate their surface properties and overall adsorption performance. The iodine number indicates microporosity, while MB adsorption capacity reflects the mesoporous structure and surface interaction potential.

Comparing these values between pristine activated carbon and NPAgAC samples reveals how silver nanoparticle loading affects the material's structure and adsorption efficiency. This comparison offers key insights into the relationship between surface properties and performance, guiding the selection of effective adsorbents for specific applications.

Table 4. MB, Iodine number, and textural properties of activated carbon and NPAgACs

Sample	Number of MB (mg/g)	Number of Iodine (mg/g)	S_{BET} (m²/g)	t-Plot Micropore (m²/g)	t-Plot (m²/g)	V_{total} (cm³/g)	V_{micro} (cm³/g)	Average pore size (Å)
AC1	499	1237	1334	399.441	933.573	0.846	0.186	25.392
AC2	492	1612	1264	488.960	775.351	0.688	0.231	21.773
AC3	490	1047	1506	558.925	947.504	0.822	0.260	21,834
NPAgAC1	453	1022	1517	631.154	886.757	0.747	0.305	19.704
NPAgAC2	421	934	1178	456.710	721.339	0.621	0.215	21.112

As shown in Table 4, a comparative summary of the MB adsorption capacity, iodine number, and key textural properties, including surface area and pore structure, of pristine activated carbon and silver nanoparticle-impregnated activated carbons (NPAgACs) is presented. The MB adsorption capacity reflects the material's ability to remove dye molecules from aqueous solutions, primarily indicating the availability of mesopores. The iodine number is a classical indicator of microporosity and total surface area. A noticeable variation in these parameters is observed upon NPAg loading.

Typically, a slight decrease in both iodine number and surface area after Ag impregnation suggests partial pore blockage or surface coverage by silver nanoparticles. Nevertheless, the retained or even enhanced MB adsorption in some NPAgACs indicates that the functional surface chemistry may have improved due to the presence of silver, supporting dye molecule interaction. These results highlight the trade-off between surface area reduction and functional enhancement through silver nanoparticle incorporation.

Table 5 presents the number of surviving microorganisms and their corresponding D-values following the inhibition of E. coli by NPAgAC2 under varying temperature and time conditions. This data provides insight into the thermal resistance behavior of E. coli in the presence of the silver-loaded activated carbon, offering a quantitative evaluation of the antibacterial efficiency of NPAgAC2 over time.

When Table 5 is examined, the temperature with the highest D value is 30 °C. However, when the results were evaluated, 30°C proved unsuitable for inhibiting *E. coli*, and 20 °C was found to be the most suitable temperature.

Table 5. Number and D values of microorganisms surviving in the medium after inhibition of E. coli by temperature and time-dependent on NPAgAC2

Temperature ºC – (log)				
Time(mn)	20 ºC	25 ºC	30 ºC	35 ºC
0	6	6	6	6
5	2.466	2.444	2.201	1.724
10	2.423	2.103	1.968	1.204
15	2.264	1.68	1.41	0.95
D (mn)	0.0202	0.0755	0.0997	0.0774

The Colony (*E. coli*) Count according to Time and Temperature is shown in Figure 10. This study calculated D values to determine the heating time required to kill 90% of the live microorganism population in the environment at four different temperatures. The results were 0.0202 for 20°C, 0.0755 for 25°C, 0.0997 for 30°C, and 0.0774 for 35 °C. Upon examination of Table 5, the temperature with the highest D value is 30°C. However, upon evaluation of the results, 30°C proved unsuitable for inhibiting E. coli, and 20°C was found to be the most suitable temperature.

Figure 11 demonstrates that E. coli inhibition is time- and temperature-dependent, with lower D-values indicating higher sensitivity. At 20°C, the lowest D-value (0.0202) corresponds to a 90% reduction in bacterial numbers per minute with NPAgAC1. Figure 11 further supports this trend, showing strong correlations (R^2 = 0.901–0.9954) between Log D-values and time across different temperatures. The highest correlation was observed at 25 °C, indicating a strong linear relationship between Log D and time at this temperature.

These results align well with Figure 11, confirming the study's consistency, reliability, and overall validity. Furthermore, the findings suggest that 25°C and 15 min were sufficient to effectively eliminate E. coli from drinking water, demonstrating the rapid antimicrobial properties of the developed materials. The NPAgACs in this study were deemed highly effective in inhibiting E. coli, as strongly supported by existing literature [26, 2
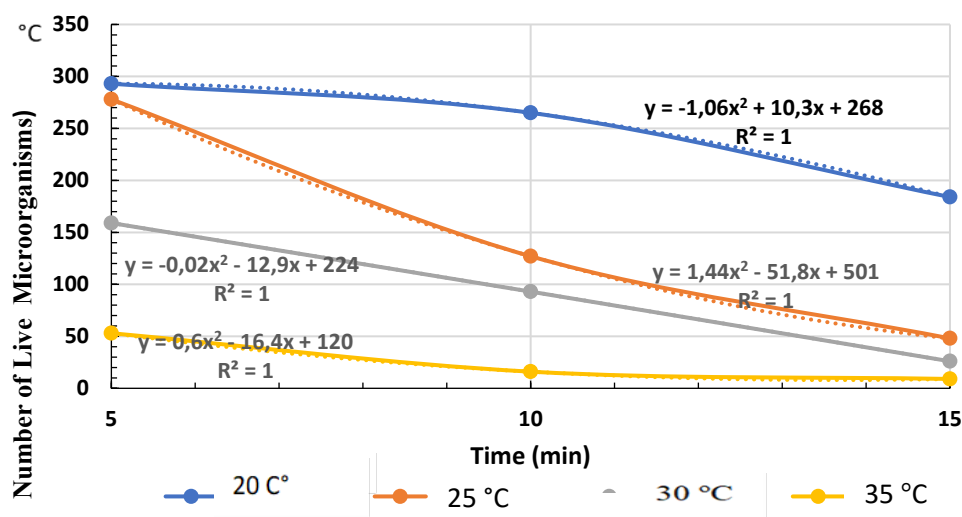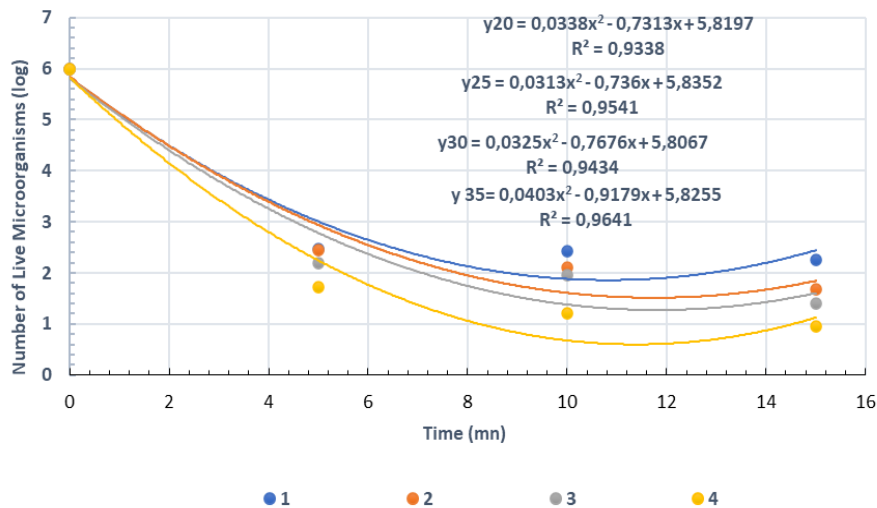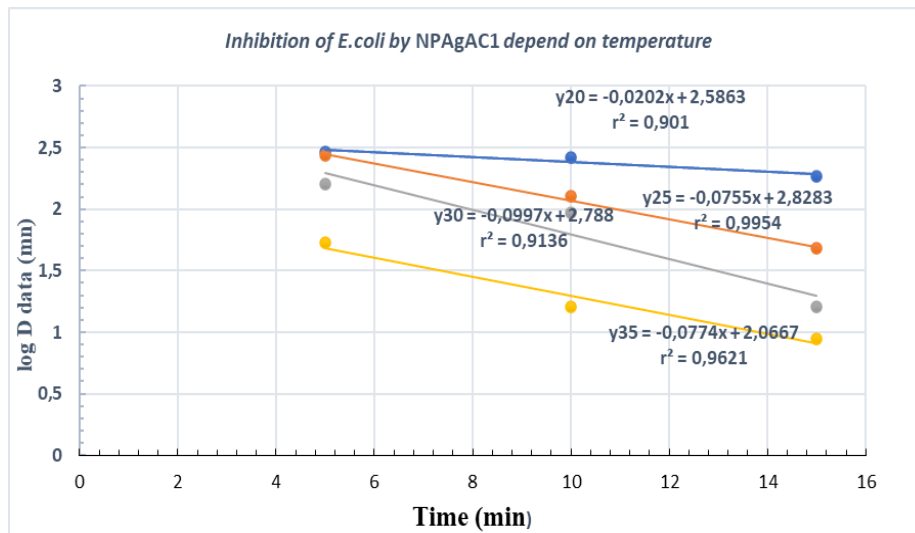

Figure 9. Time and temperature decreased colony (*E.coli*) number

Figure 10. Change in the number of living microorganisms (log) depends on temperature and time

Figure 11. Inhibition of *E.coli* by NPAgAC1 depends on temperature

4. Conclusion

In this study, NPAgAC was obtained by binding NPAg to activated carbon produced from hazelnut shells, an agricultural waste, to address and remove dyestuff and microbial pollution in waters, which pose a risk to food safety and public health. The antimicrobial activity and dye removal of the obtained NPAgACs were tested and found suitable for removing *E.coli* from polluted waters. Three different sizes (50, 70, 150 mesh) of hazelnut shells are obtained by carbonizing the hazelnut shells in an inert nitrogen (N_2) atmosphere at 700 °C in a thermal tube furnace, for three of which the best efficiency is obtained (AC1,50 mesh 1:4 (43%),

AC2, 70 mesh 1:2 (40%), and AC3, 150 mesh 1:3 (37%) characterization studies were performed.

SEM, FT-IR, and BET images were evaluated, revealing a honeycomb porous structure of activated carbon with a high surface area. Yield analysis showed the highest yield at 43%. The MB number of the produced ACs was 490-499 mg/g, while the iodine number ranged from 1047 to 1612 mg/g, consistent with the BET surface area. While the MB numbers of NPAgACs ranged from 421 to 453 mg/g, the iodine numbers decreased to 934-1022 mg/g due to the reduction in pores resulting from Ag binding. The BET surface area for ACs was 1264-1506 m²/g, while for NPAgACs, it was determined to be 1178-

$1517 \ m^2/g$. Well-diffusion and spreading plate methods were used to control the antimicrobial properties of NPAgAC. Escherichia coli (*E. coli*) and Staphylococcus aureus (*S. aureus*), which are considered risk factors for food safety and public health, were used as pathogenic microorganisms in the study. In the study, two different antibiotic discs (Ampicillin 10 mg and cefotaxim 30 mg) were used in the control group, and the results were determined to be highly effective according to EUCAST criteria. In addition, when the study of *E. coli* in drinking water was evaluated at three time points (5, 10, 15 min) and four different temperatures (20, 25, 30, and 35°C), 15 min at 25 °C was found to be sufficient. The hazelnut shell is a suitable starting material for raw carbon production, and NPAgAC exhibits high antimicrobial properties about food safety.

Article Information Form

Authors' Contribution
Birsen Sarıcı conducted the experiments and interpreted the microbiological studies. Esra Altıntığ carried out the characterization studies, interpretation, and manuscript writing. Şükrü Karataş supervised the manuscript and contributed to the experimental interpretations.

The Declaration of Conflict of Interest/ Common Interest
No conflict of interest or common interest has been declared by authors.

Artificial Intelligence Statement
No artificial intelligence tools were used while writing this article.

Copyright Statement
Authors own the copyright of their work published in the journal and their work is published under the CC BY-NC 4.0 license.

References

[1] J. Baruah, B.K. Nath, R. Sharma, S. Kumar, R.C. Deka, D. C. Baruah, E. Kalita, "Recent Trends in the Pretreatment of Lignocellulosic Biomass for Value-Added Products," Front Energy Res, vol. 6, no. 141, pp. 1-19, 2018.

[2] T. Q. Tuan, N. Van Son, H. T. K. Dung, H. L. Nguyen, T. T. Bui, T. V. A. Nguyen, D. H. Nguyen, H. H. Nguyen, "Preparation and properties of silver nanoparticles loaded in activated carbon for biological and environmental applications," Journal Hazard Mater, vol. 192, no. 3, pp. 1321-1329, 2011.

[3] A. A. Mostafa, A. A. Al-Askar, K. S. Almaary, T. M. Dawoud, E. N. Sholkamy, M. M. Bakri, "Antimicrobial activity of some plant extracts against bacterial strains causing food poisoning diseases," Saudi Journal of Biological Sciences, vol. 25, no. 2, pp. 361-366, 2018.

[4] A. Mani, M. Amalanathan, M. S. M. Mary, C. Parvathiraja, A. Alothman, S. M. Wabaidur, M. A. Islam, "Enhanced photocatalytic and biological observations of green synthesized activated carbon, activated carbon doped silver, and activated carbon/silver/titanium dioxide nanocomposites," Journal of Inorganic Organometallic Polymers Materials, vol. 32, no. 1, pp. 267-279, 2022.

[5] W. Trisunaryanti, K. Wijaya, T. Riyono, N. Wahyuningtyas, S. P. Utami, L. Larasati, "Characteristics of coconut shell-based activated carbon as Ni and Pt catalyst support for hydrotreating Calophyllum inophyllum oil into hydrocarbon-based biofuel," Journal of Environmental Chemical Engineering, vol. 10, no. 5, pp. 108-209, 2022.

[6] A. Sobhan, K. Muthukumarappan, L. Wei, T. Van Den Top, R. Zhou, "Development of an activated carbon-based nanocomposite film with antibacterial property for smart food packaging," Materials Today Communications, vol. 23, pp. 101-m124, 2020.

[7] J. C. M. Márquez, A. H. Partida, M. del Carmen, M. Dosta, J. C. Mejía, J. A. B. "Martínez Silver nanoparticles applications (AgNPS) in aquaculture," International Journal of Fisheries and Aquatic Studies, vol. 6, pp. 5-11, 2018.

[8] S. Yorgun, D. Yıldız, "Preparation and characterization of activated carbons from Paulownia wood by chemical activation with H_3PO_4," Journal of the Taiwan Institute of Chemical Engineers, vol. 53, pp. 122-131, 2015.

[9] H. Teramura, E. Yasuda, Y. Naisei, "Impact of Spreading Time to Recovery Rate in Suitability Test of Solid Agar Media," Biocontrol Science and Technology, vol. 26, no. 1, pp. 43-47, 2021.

[10] N. Söyler, J. L. Goldfarb, S. Ceylan, M. T. Saçan, "Renewable fuels from pyrolysis of Dunaliella tertiolecta: An alternative approach to biochemical conversions of microalgae," Energy, vol. 120, pp. 907-914, 2017.

[11] H. Ç. Kazici, V. Yönten, M. R. Kivanç, M. Ertas, F. Salman, M. Yayla, "Antimicrobial properties of multimetallic of silver compounds immobilized on active carbon and nano carbon tubes," Current Research in Green and Sustainable Chemistry, vol. 4, pp. 100-204, 2021.

[12] K. S. Ukanwa, K. Patchigolla, R. Sakrabani, E. Anthony, S. Mandavgane, "A review of chemicals to produce activated carbon from agricultural waste biomass," Sustainability, vol. 11, no. 22, p. 6204, 2019.

[13] T. V. Duncan, "Applications of nanotechnology in food packaging and food safety: Barrier materials, antimicrobials, and sensors," Journal of Colloid and Interface Science, vol. 363, no. 1, pp. 1-24, 2011.

[14] S. Moeinzadeh, E. Jabbari, "Nanoparticles and their applications. In Springer handbook of nanotechnology," Springer, Berlin, Heidelberg, pp. 335-361, 2017.

[15] U. Latif, K. Al-Rubeaan, A. T. Saeb, "A review on antimicrobial chitosan-silver nanocomposites: A roadmap toward pathogen targeted synthesis,"

International Journal of Polymeric Materials and Polymeric Biomaterials, vol. 64, no. 9, pp. 448-458, 2015.

[16] A. A. El-Sayed, A. M. Khalil, M. El-Shahat, N.Y. Khaireldin, S.T. Rabie, "Antimicrobial activity of PVC-pyrazolone-silver nanocomposites," Journal of Macromolecular Science, Part A, vol. 53, no. 6, pp. 346-353, 2016.

[17] P. Chingombe, B. Saha, R. J. Wakeman, "Sorption of atrazine on conventional and surface modified activated carbons," Journal of Colloid and Interface Science, vol. 302, no. 2, pp. 408-416, 2006.

[18] B. Sarıcı, Ş. Karatas, E. Altintig, "Removal of Methylene blue from aqueous solution with activated carbon produced from hazelnut shells by K_2CO_3 activation," Desalination and Water Treatment, vol. 254, pp. 287-301, 2022.

[19] Y. Zhao, Z.O. Wang, X. Zhao, W. Li, S. X. Liu, "Antibacterial action of silver-doped activated carbon prepared by vacuum impregnation," Applied Surface Science, vol. 266, pp. 67-72, 2013.

[20] S. Singh, A. Bharti, V. K. Meena, "Structural thermal zeta potential and electrical properties of disaccharide reduced silver nanoparticles," Journal of Materials Science: Materials in Electronics, vol. 25, pp. 3747–52, 2014.

[21] C. G. Giske, J. Turnidge, R. Cantón, G. Kahlmeter, "Update from the European committee on antimicrobial susceptibility testing (EUCAST), Journal of Clinical Microbiology, vol. 60, no. 3, pp. e00276-21, 2022.

[22] Y. Sudaryanto, S. B. Hartono, W. Irawaty, H. Hindarso, S. Ismadji, "High Surface area activated carbon prepared from cassava peel by chemical activation," Bioresource Technology, vol. 97, pp. 734-739, 20076.

[23] M. Uyttendaele, E. Franz, O. Schlüter, "Food safety, a global challenge," International Journal of Environmental Research and Public Health, vol. 13, no. 1, p. 67, 2016.

[24] P. Biswas, R. Bandyopadhyaya, "Water disinfection using silver nanoparticle-impregnated activated carbon: Escherichia coli cell-killing in batch and continuous packed column operation over a long duration," Water Research, vol. 100, pp. 105-115, 2016.

[25] S. Thomas, R.A. Gonsalves, J. Jose, S. H. Zyoud, A. R. Prasad, J. Garvasis, "Plant-based synthesis, characterization approaches, applications and toxicity of silver nanoparticles: A comprehensive review," Journal of Biotechnology, vol. 394, pp. 135-149, 2024.

[26] Y. Baran, H. S. Gökçe, M. Durmaz, "Physical and mechanical properties of cement containing regional hazelnut shell ash wastes," Journal of Cleaner Production, vol. 259, p. 120965,2020.

[27] Ö. Bağ, K. Tekin K. "Atık lignoselülozik biyokütleden hidrotermal karbon üretimi ve karakterizasyonu," Gazi Üniversitesi Mühendislik Mimarlık Fakültesi Dergisi, vol. 35 no. 2, pp. 1063-1076, 2019.

[28] X. Jian, X. Zhuang, B. Li, X. Xu, Z. Wei, Y. Song, E. Jiang, "Comparison of characterization and adsorption of biochars produced from hydrothermal carbonization and pyrolysis," Environmental Technology & Innovation, vol. 10, pp. 27-35, 2018.

[29] Z. Heidarinejad, M. H. Dehghani, M. Heidari, G. Javedan, L. Ali, M. Sillanpää, "Methods for preparation and activation of activated carbon: A review," Environmental Chemistry Letters, vol. 18, no. 2, pp. 393-415, 2020.

[30] Ç. Çuhadar, "Production and characterization of activated carbon from hazelnut shell and hazelnut husk," (Master's thesis, Middle East Technical University), pp. 23-82, 2005.

[31] E. Altintig, B. Sarıcı, S. Karataş, "Prepared activated carbon from hazelnut shell where coated nanocomposite with Ag+ used for antibacterial and adsorption properties," Environmental Science and Pollution Research, vol. 30, no. 5, pp. 13671-13687, 2023.

[32] D. Angın, E. Altintig, T. E. Köse, "Influence of process parameters on the surface and chemical properties of activated carbon obtained from biochar by chemical activation," Bioresource Technology, vol. 148, pp. 542-549, 2013.

[33] C. Tang, Y. W. Sun, "Green and facile fabrication of silver nanoparticles loaded activated carbon fibers with long-lasting antibacterial activity," RSC advances, vol. 4, no. 2, pp. 523-530, 2014.

[34] K. Y. Yoon, J. H. Byeon, C. W. Park, J. Hwang, "Antimicrobial effect of silver particles on bacterial contamination of activated carbon fibers," Environmental Science & Technology, vol. 42, no. 4, pp. 1251-1255, 2008.

[35] T. C. Chandra, M. M. Mirna, Y. Sudaryanto, S. J. C. E. J. Ismadji, "Adsorption of basic dye onto activated carbon prepared from durian shell: Studies of adsorption equilibrium and kinetics," Chemical Engineering Journal, vol. 127, no. 1-3, pp. 121-129, 2007.

[36] A. G. Blanco, J. A. de Oliveira, R. López, J. C. Moreno-Piraján, L. Giraldo, G. Zgrablich, K. Sapag, "A study of the pore size distribution for activated carbon monoliths and their relationship with the storage of methane and hydrogen. Colloids and Surfaces A," Physicochemical and Engineering, vol. 357, no. 1-3, pp. 74-83, 2010.

[37] N. Korkmaz, A. Ceylan, Hamid, A. Karadağ, A. S. Bülbül, M. N. Aftab, O. Cevik, F. Sen, "Biogenic silver nanoparticles synthesized via Mimusops elengi fruit extract, a study on antibiofilm, antibacterial, and anticancer activities,"

Journal of Drug Delivery Science and Technology, vol. 59, p. 101864, 2010.

[38] M. A. Islam, M. V. Jacob, E. Antunes, "A critical review on silver nanoparticles: From synthesis and applications to its mitigation through low-cost adsorption by biochar," Journal of Environmental Management, vol. 28, p. 1111918, 2021.

[39] Ş. Karadirek, H. Okkay, "Ultrasound assisted green synthesis of silver nanoparticle attached activated carbon for levofloxacin adsorption," Journal of the Taiwan Institute of Chemical Engineers, vol. 105, pp. 39-49, 2019.

[40] E. Altintig, S. Kirkil "Preparation and properties of Ag-coated activated carbon nanocomposites produced from wild chestnut shell by $ZnCl_2$ activation," Journal of Taiwan Institute of Chemical Engineers, vol. 63, pp. 180-188, 2016.

[41] S. Sharifan, "A comparative optimization study of activated carbon production from hazelnut shells by thermal and microwave heating methods," (Doctoral dissertation, Imperial College London), pp. 212-231, 2014.

[42] E. Altintig, O. F. Soydan, "Methylene blue adsorption and preparation silver bound to activated carbon with sol-gel method," Sakarya University Journal of Science, vol. 22, no. 6, pp. 1812-1819, 2018.

[43] L. Y. Le, F. Baron, M. Gautier, "Staphylococcus aureus and food poisoning," Genetics and Molecular Research: GMR, vol. 2, no. 1, pp. 63-76, 2003.

[44] H. B. Haberecht, N. J. Nealon, J. R. Gilliland, A. V. Holder, C. Runyan, R. C. Oppel, E. P. Ryan, "Antimicrobial-resistant Escherichia coli from environmental waters in Northern Colorado," Journal of Environmental and Public Health, vol. 2019, pp. 1-13, 2019.

[45] M. A. Lim, J. Y. Kim, D. Acharya, B. B. Bajgain, J. H. Park, S. J. Yoo, K. Lee, "A diarrhoeagenic enteropathogenic Escherichia coli (EPEC) infection outbreak that occurred among elementary school children in Gyeongsangbuk-Do province of South Korea was associated with consumption of water-contaminated food items," International Journal of Environmental Research and Public Health, vol. 17, no. 9, pp. 1-19, 2020.

[46] A. Yurtay, M. Kılıc, "Fast and effective production of industrial grade activated carbon," Journal of Porous Materials, vol. 30, pp. 1207-1220, 2023.

[47] S. Konyalı, M. Demir, "The agricultural policies applied for hazelnut and problems of hazelnut producers in Sakarya Province," Eurasian Journal of Agricultural Economics, vol. 4, no. 1, pp. 11-21, 2024.

[48] M. A. Kara, "Investigation of hazelnut producing provinces with cluster analysis methods," Ordu University Journal of Science and Technology, vol. 14, no. 2, pp. 396-410, 2024.

Antibiotic Resistance Profiles and Biochemical Characterization of Bacteria Isolated from Gökçeada Salt Lake Lagoon (Çanakkale) Sediment Samples

İlke Karakaş[1*] (iD), Nurcihan Hacıoğlu Doğru[2] (iD)

[1] Çanakkale Onsekiz Mart University, Vocational School of Health Services, Çanakkale, Türkiye, ilke.karakas@comu.edu.tr, ror.org/05rsv8p09
[2] Çanakkale Onsekiz Mart University, Department of Biology, Faculty of Science, Çanakkale, Türkiye, nhacioglu@comu.edu.tr, ror.org/05rsv8p09
*Corresponding Author

ARTICLE INFO

ABSTRACT

Gökçeada Salt Lake Lagoon in Çanakkale, Türkiye, is a hypersaline environment that supports halophilic bacterial communities. This study examined the antibiotic susceptibility of 60 bacterial isolates obtained from four seasonal sediment samples. Morphological and biochemical characterization of the isolates included Gram staining, indole production, nitrate formation tests, and elemental analysis using ICP-OES. Antibiotic resistance was assessed via the disk diffusion method using seven antibiotics: Novobiocin (5 μg), Erythromycin (15 μg), Streptomycin (10 μg), Bacitracin (10 μg), Penicillin G (10 μg), Ampicillin (10 μg), and Tetracycline (30 μg). ICP-OES results showed elevated S, Ca, Mg, Na, and Fe concentrations, particularly in April 2024. The Multiple Antibiotic Resistance (MAR) index exceeded 0.2 in all isolates, with the highest value (0.7142) also detected in April 2024. The Shapiro-Wilk test indicated non-normal distribution of MAR values; thus, the Kruskal-Wallis test was used for statistical analysis. Although no significant difference was found between sampling periods ($p > 0.05$), seasonal increases in resistance suggest gradual adaptation. The consistently high MAR indices point to ongoing anthropogenic pressure, likely due to tourism, agriculture, and livestock activities in the region. This persistent exposure may drive resistance development in microbial populations. The findings underscore the importance of monitoring antibiotic resistance in halophilic bacteria, as such resistance may pose public health risks through environmental pathways.

1. Introduction

Coastal lagoons are rich in biodiversity and represent environmentally sensitive ecosystems. These wetlands serve as transitional zones between freshwater and saltwater, creating unique hydrological conditions that support a diverse array of plants, animals, and microbial species [1]. The dynamic interplay between freshwater inflows and seawater intrusion results in fluctuating salinity levels, which shape the ecological structure of these environments and facilitate the adaptation of specialized organisms.

Gökçeada Salt Lake Lagoon (Çanakkale), located in western Türkiye, is one such unique ecosystem. It has a relatively shallow depth of approximately 0.8–1.2 meters and covers a surface area of 2 km². Due to its high salinity and distinctive environmental conditions, the lagoon provides an optimal habitat for extremophilic microorganisms, particularly halophiles [2, 3]. These microorganisms have evolved remarkable physiological and genetic adaptations that enable them to survive in hypersaline conditions, making them integral components of the lagoon's microbial community. The lagoon is located within the administrative boundaries of Eşelek village in Gökçeada district of Çanakkale

province, with the village having a small population of approximately 170 people.

The lagoon is situated about 1 km from the village center and lies only 0.3 km from the main road, indicating relatively easy access. Its surroundings exhibit various anthropogenic influences: to the south and east, just 180 meters from the lagoon, there are livestock farming facilities, including a dairy farm and a goose breeding operation. Additionally, a beach used for tourism purposes is also located nearby, contributing to seasonal human activity in the area. Agricultural lands are present approximately 100 meters northeast of the lagoon, potentially impacting the ecosystem through runoff or nutrient input. Although there is no direct waste discharge into the lagoon at the sampling points, these localized human activities may influence its physicochemical and microbial characteristics, indicating a degree of anthropogenic pressure on this otherwise unique hypersaline environment.

Halophilic microorganisms play a crucial role in biogeochemical cycles, contributing to nutrient recycling, organic matter degradation, and overall ecosystem functioning in saline environments. Their unique adaptation mechanisms allow them to withstand extreme osmotic stress, which has also been linked to their ability to develop resistance to antibiotics [4]. The genetic plasticity of halophilic bacteria enables them to acquire and maintain antibiotic resistance genes, often through horizontal gene transfer, further enhancing their resilience to environmental stressors. Antibiotic resistance has emerged as a critical global health concern, with an increasing number of resistant bacterial strains being detected in natural ecosystems, particularly those subjected to anthropogenic pressures.

The widespread and often indiscriminate use of antibiotics in human medicine, agriculture, and aquaculture has contributed to the selection and proliferation of resistant bacterial populations [5]. Coastal ecosystems, including lagoons, are particularly vulnerable to the accumulation and dissemination of antibiotic-resistant bacteria due to their exposure to agricultural runoff, industrial discharge, and untreated or partially treated wastewater [6].

One of the key indicators used to assess antibiotic resistance in bacterial populations is the Multiple Antibiotic Resistance (MAR) index, which reflects the extent to which bacteria have developed resistance to multiple antibiotics. A high MAR index suggests significant selective pressure exerted by anthropogenic activities, leading to the persistence of resistant strains in the environment. In ecosystems influenced by human activity, such as coastal lagoons, the presence of MAR bacteria poses potential risks not only to microbial communities but also to public health, as resistant genes can be transferred to clinically relevant pathogens [7].

Given the ecological significance of Gökçeada Salt Lake Lagoon and the increasing concerns regarding antibiotic resistance in extreme environments, this study aims to characterize the biochemical properties and antibiotic resistance profiles of halophilic bacteria isolated from the lagoon. Specifically, the study focuses on evaluating the MAR index to assess the impact of environmental and anthropogenic factors, such as agriculture, animal husbandry, and tourism, on the prevalence of antibiotic-resistant bacteria in this hypersaline ecosystem. Understanding these resistance patterns is essential for developing strategies to mitigate the spread of antibiotic resistance and for preserving the ecological integrity of saline environments.

2. Materials and Methods

2.1. Field studies and halophile isolation

Sediment samples were taken from the lagoon at 20-25 cm depth in four different periods (September 2023, December 2023, April 2024, July 2024), brought to the laboratory under aseptic conditions, and stored at +4°C for isolation. In situ measurements of physicochemical parameters, including temperature, dissolved oxygen (DO), pH, and electrical conductivity (EC), were conducted using a Hach-Lange multiparameter probe (Model HQ40d18).

ICP-OES elemental analyses (sulfur (S), calcium (Ca), magnesium (Mg), sodium (Na), manganese (Mn), copper (Cu), iron (Fe), zinc (Zn), boron (B), selenium (Se)) of sediment samples collected from field studies were carried out as a service purchase.

SW-25 medium (NaCl; 202,5 g/L, MgCl$_2$; 17,5 g/L, MgSO$_4$; 24 g/L, CaCl$_2$; 0,9 g/L, KCl; 5 g/L, NaHCO$_3$; 0,15 g/L, NaBr; 0,065 g/L, Yeast extract; 5 g/L, Agar; 20 g/L) was determined to be suitable for halophilic bacteria by Bozkurt [8] and SW-25 medium was used in the studies. 10 g of sample was suspended in 0.9% physiological serum isotonic solution, and serial dilutions were made from this solution up to 10^{-5}. The spread plate method cultured 100 µL of each dilution on selective media for halophiles. After 7 days of incubation at 37-40°C, the purification process of bacterial isolates was carried out on SW-25 agar. All purified isolates were stored in a glycerol medium at –20°C [8].

2.2. Biochemical analysis

The cell morphology of pure cultures was examined by Gram staining. Gram (+) bacteria were observed in purple, and Gram (-) bacteria were observed in pink [8]. For the indole test, bacteria were incubated at 40°C for 7 days in a SW-25 medium containing 1% tryptone, and a red ring was considered a positive result [9]. The nitrite test was incubated in a SW-25 medium containing 1% KNO$_3$. Nitrite and nitrate presences were determined by color changes [10, 11].

2.3. Characterization of antibiotic resistance profiles

To assess antibiotic resistance profiles, the resistance of isolated bacterial strains to various antibiotics was evaluated. Bacterial cultures were prepared and spread on SW-25 agar according to the 0.5 McFarland standard. Novobiocin (NV, 5 µg), Erythromycin (E, 15 µg), Streptomycin (S, 10 µg), Bacitracin (B, 10 µg), Penicillin G (P, 10 µg), Ampicillin (AM, 10 µg), and Tetracycline (TE, 30 µg) disks were placed on each bacterial strain using the disk diffusion method. Plates were incubated at 37°C for 24 hours. At the end of incubation, inhibition zone diameters formed around each antibiotic disk were measured, and resistance was classified as intermediate or susceptible according to CLSI (Clinical and Laboratory Standards Institute) standards. The selection of these antibiotics was made both to evaluate the resistance profile of environmentally derived bacteria and to determine their susceptibility levels to different antibiotic classes. In addition, the combined use of antibiotics from different groups allows the determination of broad-spectrum resistance profiles of halophilic bacteria.

The number of antibiotics to which each isolate showed resistance was recorded to determine the Multiple Antibiotic Resistance (MAR) index. The MAR index was calculated by dividing the number of antibiotics to which the isolate was resistant by the total number of antibiotics tested, and strains higher than 0.2 were considered high-risk groups [12].

2.4. Statistical analysis

In this study, a one-way ANOVA test was applied to evaluate whether the MAR index values obtained in different periods showed a statistically significant change. The Levene test was performed to evaluate whether the variances of the groups were homogeneous. Mean, standard deviation (SD), minimum (min), and maximum (max) values were calculated for each period. Shapiro-Wilk normality test and Kruskal-Wallis were applied to test the conformity of the data to a normal distribution [13].

PCA (Principal Component Analysis) was used to scale and visualize large data sets based on antibiotic resistance profiles of bacterial isolates. This analysis was applied to determine the variability in the dataset and to visually represent the similarities between isolates. The resistance and susceptibility profiles of each isolate against antibiotics (S: susceptible, R: resistant) were converted into numerical data and made suitable for PCA. The data were analyzed in a standardized manner, and the first two principal components obtained (PC1 and PC2) were selected to reflect the largest variation in the resistance profiles of bacterial isolates. PCA analysis was applied to visualize the representation of each isolate on a two-

dimensional plane, and the grouping trends among the isolates were revealed [14]. NMDS (Non-metric Multidimensional Scaling) was used to visualize the multi-dimensional data of the resistance profiles of bacterial isolates against antibiotics.

This analysis provides a non-metric method to represent similarities between isolates and allows visualization of data in two or more dimensions without reducing the number of dimensions of the dataset, preserving the original structure. Each bacterial isolate was converted to numerical values according to its resistance to antibiotics, and a distance matrix was created. This distance matrix was used to determine similarities between isolates. Using this distance data, NMDS analysis located the isolates based on their antibiotic resistance profiles and color-coded them according to their resistance levels. This visualization was used to clearly distinguish isolates with high and low resistance levels [15].

3. Results

3.1. Isolation and biochemical characterization of halophilic bacteria

Seasonal variation in physicochemical parameters of the Gökçeada Salt Lake Lagoon was evident across the sampling periods. The highest water temperature was recorded in Sep 2023 ($32.1 \pm 0.31\,°C$) and Jul 2024 ($30.6 \pm 0.54\,°C$), while the lowest was observed in Dec 2023 ($14.2 \pm 1.47\,°C$). pH values ranged from slightly acidic to neutral, with the lowest in Sep 2023 (5.06 ± 0.16) and the highest in Dec 2023 (7.41 ± 0.29). Dissolved oxygen levels were markedly elevated in Dec 2023 ($16.15 \pm 3.37\,mg/L$), whereas lower concentrations were detected during the warmer months. Electrical conductivity showed a clear increase during the summer, reaching its peak in Jul 2024 ($140.1 \pm 2.74\,mS/cm$), and the lowest values occurred in Dec 2023 ($52.07 \pm 1.71\,mS/cm$).

In this study, the concentrations of S, Ca, Mg, Na, Mn, Cu, Fe, Zn, B, and Se were evaluated across four sampling periods—Sep 2023, Dec 2023, Apr 2024, and Jul 2024 using ICP-OES analysis. The results revealed a notably high concentration of Ca (14,869.75 ppm), Mg (1,765.0 ppm), Na (571.25 ppm), and Fe (4,932.0 ppm) in Apr 2024. In the same period, Zn (66.585 ppm) and B (98.11 ppm) levels were also within a sufficient range. In Sep 2023, the highest concentrations were observed for S (8,718.5 ppm) and Na (73,609.25 ppm).

In contrast, elemental concentrations in Dec 2023 were generally low, with particularly minimal levels of S (21.068 ppm), Fe (<0.006 ppm), and Cu (<0.689 ppm). In Jul 2024, elevated levels of Mg (2,147.75 ppm) and Na (3,267.25 ppm) were detected, while B remained below the threshold (<13.232 ppm). The markedly elevated concentrations of Ca, Mg, Na, and Fe in Apr 2024 highlight this period as a peak phase for elemental accumulation.

A total of 60 halophilic bacteria were isolated within the scope of the study (Fig 1).

Figure 1. Halophilic bacteria isolated from sediment samples

When the Gram properties were evaluated, 33 of the isolates were determined as gram-positive bacilli, 15 as gram-positive cocci, 7 as gram-negative bacilli, 2 as gram-negative cocci, 2 as gram-negative cocci and 1 as gram-positive coccobacillus. In addition, when the biochemical test results of 60 isolates were examined, it was found that 37 isolates were indole negative (-), 23 isolates were indole positive (+), 32 were nitrite negative (-), and 28 were nitrite positive (+). The results related to nitrate show that 38 isolates were nitrate negative (-) and 22 were nitrate positive (+) (Fig. 2).
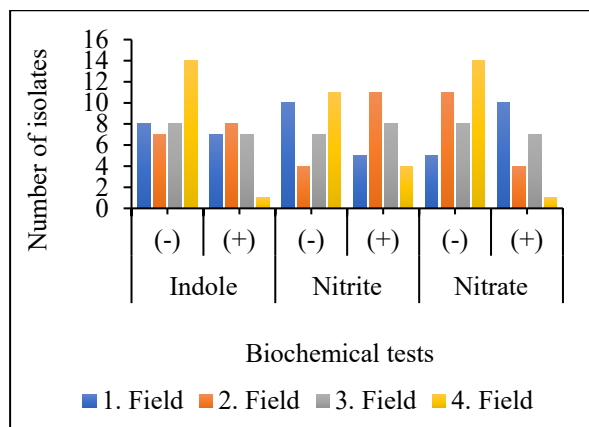
Figure 2. Biochemical analysis results of isolates

3.2. Antibiotic resistance profiles of isolates

The antibiotic susceptibility profiles of bacterial strains isolated from Gökçeada Salt Lake Lagoon were analyzed, revealing variations in resistance (R), intermediate resistance (I), and sensitivity (S) rates to different antibiotics (Table 1, Fig 3). The highest resistance rate was observed for the antibiotic E15, where 55.0% of the strains were found to be resistant. The intermediate resistance rate was the highest for the antibiotic TE30, which was determined as 16.7%. The highest sensitivity rates were determined as 45.0% for S10 and AM10 antibiotics.

Table 1. Antibiotic susceptibility percentages of isolates

Antibiotics	S (%)	I (%)	R (%)
NV5	43.3	13.3	43.3
E15	31.7	13.3	55.0
S10	45.0	8.3	46.7
B10	36.7	11.7	51.7
P10	33.3	13.3	53.3
AM10	45.0	13.3	41.7
TE30	36.7	16.7	46.7

NV: Novobiocin, E: Erythromycin, S: Streptomycin, B: Bacitracin, P: Penicillin G, AM: Ampicillin, T: Tetracycline, S: Susceptible, I: Intermediate, R: Resistant

MAR index data show (Fig 4) the antibiotic resistance profiles of bacterial isolates obtained in different periods. MAR indexes of isolates isolated in Sep 2023 ranged between 0.285 and 0.571, which reveals that some isolates (1T9 and 1T6) had high resistance values (0.571) in Sep 2023.
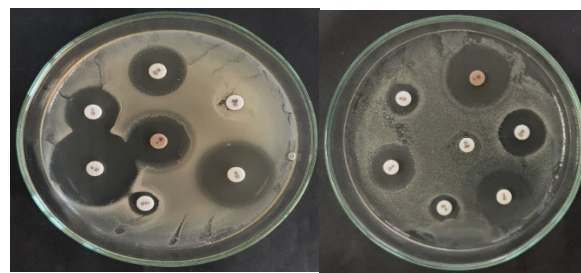

Figure 3. Antibiotic susceptibility test images of sediment isolates

In Dec 2023, MAR indexes were again observed to be between 0.285 and 0.571, with isolates such as 2T10 and 2T4 showing high resistance. There was an increase in the Apr 2024 period. Isolates coded 3T2 and 3T9 reached the highest resistance level with 0.714. Data from the Jul 2024 period show that resistance levels generally decreased slightly compared to Apr 2024, but isolates coded 4T2 and 4T5 still exhibited high values.
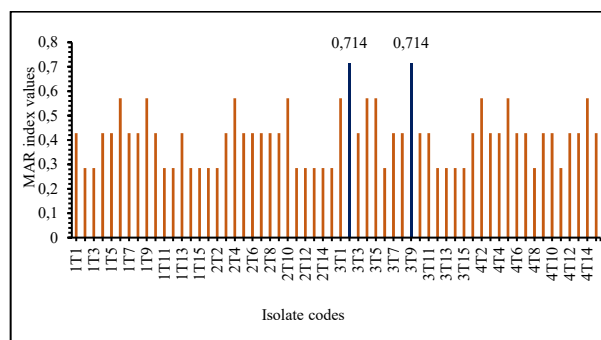
Figure 4. MAR index values of isolates (1T1: 1st sample of 1st fieldwork)

3.3. Statistical analysis

Descriptive statistics for MAR index values obtained in different periods are presented (Table 2) and Shapiro-Wilk analysis results are presented (Table 3).

Table 2. Statistical data on MAR index values

Period	Mean values	Standard deviation (SD)	Min.	Max.	Sample number (n)
Sep 2023	0.3899	0.1006	0.285	0.571	15
Dec2023	0.3803	0.1035	0.285	0.571	15
Apr 2024	0.4471	0.1516	0.285	0.714	15
Jul 2024	0.4375	0.0849	0.285	0.571	15
Control Strain (*Halomonas elongata* ATCC 33173)	0.3125	0.0678	0.250	0.400	5

Table 3. Shapiro-Wilk analysis results

Period	Shapiro-Wilk Test (p)
Sep 2023	0.003
Dec 2023	0.002
Apr 2024	0.026
Jul 2024	0.001

As a result of the Shapiro-Wilk Test (p), it was determined that the MAR index data did not conform to the normal distribution since $p < 0.05$ in all periods. These p-values indicate that the null hypothesis of the test (H_0: Data are normally distributed) was rejected for each period. In other words, MAR index values do not exhibit normal distribution. This is a common situation in data obtained from natural microbial communities. Resistance profiles of environmental microorganisms are generally affected by many factors, including antibiotic exposure, seasonal changes, environmental stresses, and microbial competition.

Failure to provide normal distribution restricted the use of parametric tests and required the use of nonparametric methods for statistical analysis. Therefore, the nonparametric Kruskal-Wallis test was applied to evaluate the difference between periods. The Shapiro-Wilk test results show that MAR index values show high variation and do not exhibit clearly normal distribution in different periods. According to the Kruskal-Wallis test results, the test statistics were calculated as $H=3.57$ and the p-value as $p=0.312$. Since this p-value is greater than the generally accepted significance level of $\alpha=0.05$, it was concluded that the MAR index values did not show a statistically significant difference between the four different periods. The distribution of MAR index values of bacteria isolated in four different periods is shown (Fig. 5).
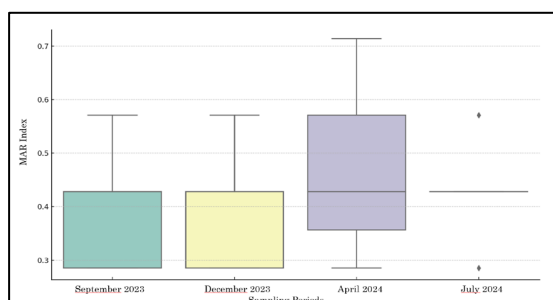
**Figure 5.** MAR index distribution by periods

The resulting PCA plot (Fig. 6) illustrates the spatial separation of isolates along the first two principal components (PC1 and PC2), which together account for the majority of the variance in the dataset. A gradient in MAR index values is evident, with isolates exhibiting higher resistance levels (MAR index > 0.57) clustering in specific regions of the plot, while those with lower resistance (MAR index < 0.43) are distributed more broadly. This suggests that bacterial isolates with higher antibiotic resistance share common resistance profiles, potentially influenced by selective pressures in the environment. Additionally, the dispersion of isolates indicates variability in resistance mechanisms among the bacterial population.
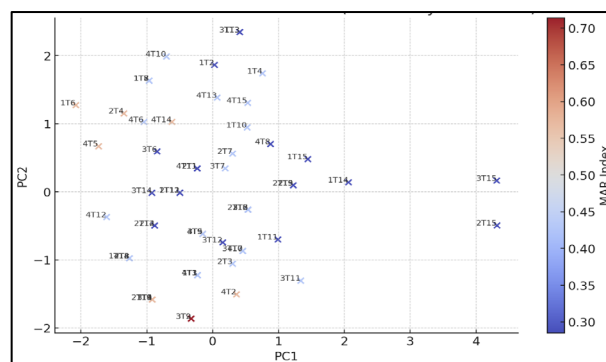
Figure 6. PCA analysis of antibiotic resistance profiles

The NMDS analysis graph (Fig. 7) shows that the points representing each bacterial isolate are positioned in a two-dimensional space according to their resistance patterns to antibiotics. The similarities and differences between the isolates are shaped according to their susceptibility to the antibiotics used in the analysis, and if the isolates are located close to each other, they have similar resistance profiles, while those that are far away indicate that they have different resistance patterns. The colored scale is visualized based on the MAR index of each isolate. Red tones indicate isolates with a high MAR index, and blue tones indicate isolates with a low MAR index.

This visualization allows visual discrimination of resistance levels between isolates. In particular, it was observed that isolates with a high MAR index are generally located in red tones, and isolates with a low MAR index are concentrated in blue tones. The resulting NMDS graph reveals that the resistance profiles of bacterial isolates to

antibiotics are distributed in a multivariate structure and that different isolate groups cluster by exhibiting similar resistance patterns.
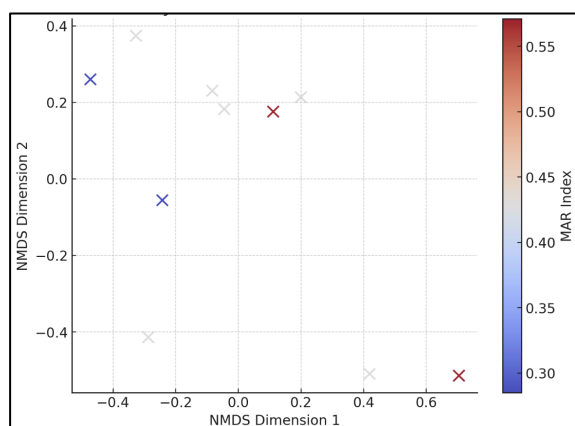
Figure 7. NMDS analysis of antibiotic resistance profiles

4. Discussion

Investigating bacterial diversity and antibiotic resistance profiles in lagoon ecosystems is of great importance for understanding the ecology of these dynamic environments and assessing potential sources of pollution. Compared to terrestrial systems, more variable environmental conditions in lagoons exert continuous selective pressure on microbial communities, promoting the development of diverse resistance mechanisms. The presence of bacterial isolates resistant to various contaminants reflects the ecosystem's exposure to such compounds [16, 17].

Antibiotic resistance is one of the most critical global health concerns of our time. The tendency of bacteria to adhere to surfaces such as sediments makes coastal and benthic zones particularly active areas for the persistence and spread of resistance traits against antibiotics and heavy metals [18-20].

This study investigated the antibiotic resistance profiles of culturable halophilic bacterial communities isolated from the Gökçeada Salt Lake Lagoon during different seasons. The marked differences in Gram staining and various biochemical reaction profiles of the isolates indicate that they belong to taxonomically diverse groups. This suggests that the observed antibiotic resistance patterns should not be attributed to resistance adaptation of a single

bacterial lineage over time. Rather, they reflect the dynamic responses of distinct microbial groups or resistant fractions within the culturable community shaped by the lagoon's seasonal environmental conditions.

Highly dynamic habitats such as lagoons can alter the composition of microbial populations and the prevalence of resistance genes or genetic elements through seasonal environmental pressures. Therefore, the variations in resistance profiles observed across sampling periods are likely associated with shifts in community structure or seasonal fluctuations in selective pressures. This approach provides a valuable perspective for understanding environmental reservoirs of resistance.

The findings demonstrate that culturable bacterial isolates from the Gökçeada Salt Lake Lagoon exhibited resistance to a wide range of antibiotics. Notably, high resistance rates were observed against antibiotics such as E10, B10, and P10. Similar studies conducted in other marine and coastal environments of Türkiye have also reported a high prevalence of antibiotic resistance among sediment-derived bacteria.

Comparable results were found in isolates from the Red Sea, Gölbaşı Lake, Tuzla Lagoon, and Shatkhira, where high resistance rates were reported against antibiotics including AM10, TE30, P10, Cephalothin, and Oxacillin [21-26]. The overall high resistance levels detected in this study support the hypothesis that the culturable bacterial community in Gökçeada Lagoon has been exposed to antibiotics and harbors multiple resistance traits, aligning with general knowledge about resistance prevalence in hypersaline environments. However, direct quantitative comparisons remain limited due to differences in antibiotic panels and taxonomic compositions among studies.

Seasonal variations in environmental element concentrations and physicochemical parameters are believed to influence the microbial community structure in the lagoon, thereby affecting resistance profiles. The study identified significant seasonal fluctuations in water temperature, salinity, dissolved oxygen, and pH. Sediment elemental analyses also revealed

notable differences in element concentrations across sampling periods. Particularly in Apr 2024, elevated levels of Ca, Mg, Na, and Fe were detected. Previous studies in the Gökçeada region have reported the presence and, in some cases, high concentrations of heavy metals in various environmental matrices [26]. Heavy metals, commonly found in marine environments due to both natural processes and anthropogenic activities, tend to accumulate in sediments. These metals can exert co-selective pressure on antibiotic resistance through metal resistance genes that are often co-located with antibiotic resistance genes on mobile genetic elements [27].

The MAR index is a key indicator for assessing the risk of antibiotic pollution in the environment, with values above 0.2 generally considered indicative of high-risk contamination. In the current study, a substantial proportion of the culturable bacterial isolates (95.5%) exhibited MAR index values exceeding this threshold, suggesting a significant potential risk of antibiotic resistance in the sediments of the Gökçeada Salt Lake Lagoon.

Although no statistically significant differences were found between sampling periods in terms of MAR index values, descriptive statistics and isolate-specific data revealed a trend toward higher average MAR values in isolates obtained in Apr 2024. This period also included isolates with the highest individual MAR values. This trend suggests that environmental conditions specific to Apr 2024 may have selected for or enriched bacterial populations with higher resistance levels. Increased water temperature and biological activity during this period could promote bacterial growth [28].

More importantly, the high concentrations of certain elements detected in Apr 2024 may reflect elevated environmental loading. The intensification of agricultural and livestock activities during spring in the region could lead to the runoff of fertilizers and animal waste into the lagoon, thereby increasing both elemental concentrations and the potential introduction of antibiotic residues or resistance determinants. This co-selective pressure driven by increased elemental load may be a critical factor contributing to the observed rise in resistance during Apr 2024.

The increase in MAR index during Apr 2024, compared to the tourism-heavy month of Jul 2024, suggests that environmental resistance is shaped not only by direct human density but also by complex seasonal environmental pressures. PCA and NMDS analyses showed that isolates clustered based on their resistance profiles, with high MAR isolates sharing similar patterns. These analyses highlight the presence of distinct resistance groups within the culturable community and the concentration of multidrug resistance in specific subpopulations. This supports the idea that the resistance profile of the lagoon's culturable bacterial community is not homogeneous and varies according to environmental factors.

The location of the Gökçeada Salt Lake Lagoon along major migratory bird routes raises concerns about the potential dissemination of environmental antibiotic resistance via wildlife to other ecosystems or human and animal populations [29]. Resistant bacteria and resistance genes in environmental settings may be transmitted through the food chain or direct contact, posing significant public health risks. Therefore, monitoring and understanding antibiotic resistance in ecologically dynamic and wildlife-interactive systems such as this lagoon are crucial not only for ecological health but also for human and animal health.

5. Conclusion

In conclusion, this study revealed that the antibiotic resistance profiles of culturable halophilic bacterial communities in the Gökçeada Salt Lake Lagoon vary seasonally and are shaped by the lagoon's physicochemical dynamics, elemental composition, and potential anthropogenic inputs. The increased resistance observed in Apr 2024, along with elevated elemental concentrations and MAR indices, suggests that specific environmental pressures during this period may favor the enrichment of resistant phenotypes. Focusing on the culturable community level, this study provides important baseline data on the functional status of environmental resistance reservoirs. It also

establishes a solid foundation for future molecular investigations into the mechanisms underlying these complex interactions and resistance dynamics. A deeper understanding of environmental resistance in vulnerable ecosystems, such as the Gökçeada Salt Lake Lagoon is essential for managing potential public health risks.

Article Information Form

Authors' Contribution
İK: Conducted the field studies, performed the halophile isolation and biochemical analyses, characterized antibiotic resistance profiles, and drafted the initial manuscript. NHD: Served as the supervisor for the research, contributed to the study's conception and design, assisted with data interpretation, and critically reviewed and revised the manuscript.

The Declaration of Conflict of Interest/ Common Interest
No conflict of interest or common interest has been declared by authors.

Artificial Intelligence Statement
No artificial intelligence tools were used while writing this article.

References

[1] J. L. Rodrigues-Filho, R. L. Macêdo, H. Sarmento, V. R. Pimenta, C. Alonso, C. R. Teixeira, V. M. Cionek, "From ecological functions to ecosystem services: Linking coastal lagoons biodiversity with human well-being," Hydrobiologia, vol. 850, no. 12, pp. 2611–2653, 2023.

[2] H. Aslan, O. Gonulal, E. Can-Yilmaz, B. Elipek, O. Baytut, M. Tosunoglu, "Species diversity in lentic, lotic, marine and terrestrial biotopes of Gökçeada Salt Lake Wetland (Canakkale, Turkey)," Fresenius Environmental Bulletin, vol. 5, pp. 2853–2866, 2018.

[3] B. Dutta, R. Bandopadhyay, "Biotechnological potentials of halophilic microorganisms and their impact on mankind," Beni-Suef University Journal of Basic and Applied Sciences, vol. 11, no. 1, p. 75, 2022.

[4] A. Ventosa, J. J. Nieto, A. Oren, "Biology of moderately halophilic aerobic bacteria," Microbiological Reviews, vol. 55, no. 3, pp. 423–444, 2015.

[5] D. G. Larsson, C. F. Flach, "Antibiotic resistance in the environment," Nature Reviews Microbiology, vol. 20, no. 5, pp. 257–269, 2022.

[6] J. Davies, D. Davies, "Origins and evolution of antibiotic resistance," Microbiology and Molecular Biology Reviews, vol. 74, no. 3, pp. 417–433, 2010.

[7] D. Gambino, D. Savoca, A. Sucato, V. Gargano, A. Gentile, L. Pantano, R. Alduina, "Occurrence of antibiotic resistance in the Mediterranean Sea," Antibiotics, vol. 11, no. 3, p. 332, 2022.

[8] D. Bozkurt, "Bor içeren ortamlarda prokaryotik çeşitliliğinin belirlenmesi," M.S. thesis, Eskişehir Osmangazi University, Institute of Science, 2016. [Online]. Available: https://tez.yok.gov.tr. Thesis number: 436619

[9] R. Montalvo-Rodríguez, A. Ruíz-Acevedo, J. López-Garriga, "New isolates of extremely halophilic archaebacteria (*Halobacteria*) from Puerto Rico and the Caribbean," Caribbean Journal of Science, vol. 33, no. 1, pp. 98–104, 1997.

[10] D. Rathakrishnan, A. K. Gopalan, "Isolation and characterization of halophilic isolates from Indian salterns and their screening for production of hydrolytic enzymes," Environmental Challenges, vol. 6, p. 100426, 2022.

[11] F. I. Kesbiç, N. Gültepe, N. Tüzemen, "Halobacillus trueperi CT7: A spore-forming, gelatinase producing, salt-tolerant bacteria isolated from Çankırı Salt Mine," Kastamonu University Journal of Engineering and Sciences, vol. 9, no. 2, pp. 46–52, 2023.

[12] A. Yasmin, A. Fariq, M. Jamil, "A statistical approach to determine co-existence of heavy metal and antibiotic resistance in environmental isolates of Khewra salt range, Pakistan," Biologia, vol. 76, no. 12, pp. 3801–3809, 2021.

[13] S. W. Lee, "Methods for testing statistical differences between groups in medical research: statistical standard and guideline of Life Cycle Committee," Life Cycle, vol. 2, 2022.

[14] I. T. Jolliffe, "Principal component analysis for special types of data," Springer New York, pp. 338–372, 2002.

[15] H. Li, D. Ye, X. Wang, M. L. Settles, J. Wang, Z. Hao, Z. Ma, "Soil bacterial communities of different natural forest types in Northeast China," Plant and Soil, vol. 383, pp. 203–216, 2014.

[16] P. Joshi, V. Pande, P. Joshi, "Microbial diversity of aquatic ecosystem and its industrial potential," Journal of Bacteriology & Mycology: Open Access, vol. 3, pp. 177–179, 2016.

[17] L. Tang, "The responses of soil microbes to climatic and anthropological factors in the Tibetan grasslands," PhD thesis, School of Environment and Sc, 2021. [Online]. Available: https://research-repository.griffith.edu.au/items/b7b5f9af-06af-4866-a30f-09b4f20a459d

[18] E. Marti, J. Jofre, J. L. Balcazar, "Prevalence of antibiotic resistance genes and bacterial community composition in a river influenced by a wastewater treatment plant," Plos One, vol. 8, no. 10, e78906, 2013.

[19] K. Abe, N. Nomura, S. Suzuki, "Biofilms: hot spots of horizontal gene transfer (HGT) in aquatic environments, with a focus on a new HGT mechanism," FEMS Microbiology Ecology, vol. 96, no. 5, fiaa031, 2020.

[20] L. X. He, L. Y. He, F. Z. Gao, M. Zhang, J. Chen, W. L. Jia, G. G. Ying, "Mariculture affects antibiotic resistome and microbiome in the coastal environment," Journal of Hazardous Materials, vol. 452, 131208, 2023.

[21] K. A. A. AbdelRahim, E. S. M. Soltan, M. A. Abu-Garbia, F. El-Zien, "Heavy metals and antibiotics resistance of halophilic bacteria isolated from different areas in Red Sea, Egypt," Egyptian Academic Journal of Biological Sciences, G. Microbiology, vol. 6, no. 1, pp. 77–89, 2014.

[22] V. D. Shinde, R. S. Thombre, "Antibiotic resistance profiling of marine halophilic bacteria and haloarchaea," Journal of Applied Pharmaceutical Science, vol. 6, no. 10, pp. 132–137, 2016.

[23] F. B. Kayış, S. Dinçer, F. Matyar, H. A. M. Takcı, M. S. Özdenefe, A. Arkut, "Gölbaşı ve Azaplı Göllerinden (Adıyaman) izole edilen bakterilerin tiplendirilmesi ve çoklu antibiyotik dirençliliklerinin araştırılması," Turkish Journal of Agriculture-Food Science and Technology, vol. 5, no. 1, pp. 43–47, 2017.

[24] M. Gençoğlu, "Tuzla lagününün (Karataş) mikrobiyal kalitesinin belirlenmesi, antibiyotik dirençlilik frekansının tespiti," M.S. thesis, Çukurova University, Institute of Science, 2019. [Online]. Available: https://tez.yok.gov.tr/UlusalTezMerkezi/tezDetay.jsp?id=GnUZbeBUbLDLdbFcigshXg

[25] M. K. Mohanta, S. Nasrin, M. F. Haque, A. S. Hasi, A. K. Saha, "Isolation and characterization of halophilic bacteria from salinity sediment of Shatkhira, Bangladesh," Journal of Advances in Microbiology, vol. 20, no. 5, pp. 67–76, 2020.

[26] P. Ş. Ç. Türetken, S. Kalkan, G. Altuğ, "Investigation of multiple resistance frequencies (antibiotic and heavy metal) of bacteria isolated from Gökçeada Island coastal marine sediment," Aquatic Research, vol. 8, pp. 1–11, 2025.

[27] K. Çetinkuş, "Çamaltı Tuzlası halofilik mikroorganizmaların izolasyonu ve karakterizasyonu," M.S. thesis, Anadolu University, Council of Higher Education National Thesis Center, [Online]. Available: https://tez.yok.gov.tr/UlusalTezMerkezi/tezDetay.jsp?id=WvkBlPSrRZb3vw45U9ggzQ

[28] S. K. Çelik, "A preliminary metabarcoding study of prokaryotes in Gökçeada Salt Lake Lagoon, Turkey," European Journal of Biology, vol. 80, pp. 69–74, 2021.

[29] H. Aslan, B. Elipek, O. Gönülal, Ö. Baytut, Y. Kurt, Ö. E. İnanmaz, "Gökçeada Salt Lake: A case study of seasonal dynamics of wetland ecological communities in the context of anthropogenic pressure and nature conservation," Wetlands, vol. 41, 23, 2021.

Unleashing the Hidden Potential: The Transformative Influence of Occupational Health and Safety Education on Chemical Engineers

Sümeyye Dilek [iD], Fatoş Ayça Özdemir Olgun* [iD]

Istanbul Health and Technology University, Faculty of Engineering and Natural Sciences, Department of Chemical Engineering, Istanbul, Türkiye, sumeyye.dilek@istun.edu.tr, fatos.olgun@istun.edu.tr, ror.org/008rwr521
*Corresponding Author

ARTICLE INFO	ABSTRACT
	Occupational Health and Safety (OHS) education plays a crucial role in shaping the professional development of chemical engineers, equipping them with the necessary knowledge and skills to ensure workplace safety and prevent occupational hazards. This manuscript presents a comprehensive review of the impacts of OHS education on chemical engineers, focusing on its role in enhancing awareness, knowledge acquisition, and practical application. The study explores the influence of OHS education on promoting a safety culture, improving risk assessment and management practices, and fostering a proactive approach towards identifying and mitigating occupational hazards. It also investigates the effects of OHS education on job satisfaction, professional growth, and career opportunities within the chemical engineering field. By analyzing relevant literature and case studies, this review provides valuable insights into the positive outcomes resulting from integrating OHS education into the curriculum at universities. The findings emphasize the significance of OHS education in cultivating competent and safety-conscious chemical engineers who contribute to sustainable and responsible industrial practices.

1. Introduction

Considering the occupational accidents that occur in Türkiye, the importance of occupational health and safety (OHS) education will be clear. The beginning of occupational health and safety awareness during the university years will provide convenience in business life, as well as helping to prevent many accidents. Measures and strategies designed to prevent, control, reduce or eliminate occupational hazards and risks have been continuously developed and implemented over the years in order to keep up with technological and economic changes.

The role of education in creating an OHS culture in our country and creating awareness about preventive activities are very important. There are occupational accidents that occur every year as a result of mistakes caused by lack of

education [1, 2]. Therefore, with the Law No. 6645 dated 04/04/2015 and the regulation in paragraph (i) of Article 5 of the Higher Education Law No. 2547 in Türkiye, according to the Occupational Health and Safety Law No. 6331 dated 20/06/2012, the course "Occupational Health and Safety" has been made mandatory in faculties that train graduates who can become occupational safety specialists [3]. Thus, young and newly started individuals will start to create measures to be taken against these risks at work by acting more consciously against the risks in the environments where they work.

Chemical engineers study the chemical and physical processes of substances and ensure the more efficient use of products with newly developed technology. Chemical engineering, as in many other engineering fields, requires high attention in the field of occupational health and

safety [4]. Chemical engineers should act by ensuring the safety of work and life.

With regards to literature reviews, it has been observed that there is a significant gap in studies examining the usefulness of occupational health and safety courses for chemical engineers in their professional careers, as well as the effectiveness of course content. In order to address this deficiency, the present study aims to investigate the effects of the mandatory occupational health and safety course offered in engineering faculties across universities.

The study examines the course content and includes interviews with the Istanbul Branch of the Chamber of Chemical Engineers to assess the impact of this course on experienced chemical engineers in the field. The findings of this research indicate that the occupational health and safety course is indeed beneficial in raising awareness among young chemical engineers entering the workforce [5]. However, it also highlights the need for customizing course content based on different engineering departments and delving into subjects in greater detail, rather than superficially [6]. By investigating these aspects, this study aims to contribute to the understanding of the role and impact of occupational health and safety courses for chemical engineers in academia and business environments.

2. Occupational health and safety (OHS) lecture curriculum

Occupational Health and Safety (OHS) encompasses a series of reviews and practices that aim to ensure employee safety by adhering to statutes and laws focused on mitigating potential accidents and occupational hazards. Türkiye, specifically, introduced Law No. 6645 on 04/04/2015, along with a regulation stated in paragraph (i) of Article 5 of the Higher Education Law No. 2547 [7], making OHS lectures mandatory. By law, starting from 2016, faculties of architecture and engineering were required to incorporate OHS lectures into their curriculum. In a study conducted in 2016, it was observed that 26% of the engineering faculties implemented the course within their programs. However, according to a study conducted in 2018, the rate

of implementation for engineering departments was 23%, while compliance with the legislation across all departments remained at 20% [8].

Various universities have different course timetables [9], spanning the first two terms and the last two terms of the standard four-year university education. In the long run, it has been observed that the final two terms of the course are more effective for students. During their internships, students gain valuable experience and practical knowledge that enables them to grasp the course contents better, thus significantly contributing to their professional lives in terms of up-to-date information.

Table 1. Gazi University Engineering Faculty OHS402 lecture syllabus [11]

1. Week	Fire and Fire Protection
2. Week	Explosion and Explosion Protection
3. Week	Occupational Health and Safety in Electric Consisting Works
4. Week	Occupational Health and Safety in Indoor Workplaces
5. Week	Occupational Health and Safety in Working in Pressure Vessels
6. Week	Occupational Health and Safety in High-altitude Works
7. Week	Occupational Health and Safety in Designing, Producing and Using of Work Equipments
8. Week	Occupational Health and Safety in Maintenance and Repair Works
9. Week	Midterm
10. Week	Risk Management Approachs
11. Week	Risk Assessment Methods
12. Week	A Field-Specific Example of an OHS Approach at Work (Construction)
13. Week	A Field-Specific Example of an OHS Approach at Work (Mining)
14. Week	Presentations of Project Studies
15. Week	Finals

The primary objective of OHS lectures can be defined as acquiring an understanding of risk assessment methodologies, learning to identify and manage risks specific to various business types and industries, conducting risk assessments outside their own field, and determining the necessary preventive measures. The students

who undergo these lectures gain valuable skills in risk management, the ability to organize workplaces according to OHS principles, and develop planning skills to prevent potential occupational accidents and diseases in their professional lives [10].

The OHS lecture curriculums published online by two different universities are given below for further discussion. Table 1 displays the lecture syllabus of OHS402 lecture of Gazi University Engineering Faculty.

Table 2. Altınbaş University Engineering Faculty ISG402 lecture syllabus [12]

1. Week	Occupational Health and Safety Services
2. Week	Supervision of the Working Environment, Workplace, Building and its Extensions
3. Week	Identification of Hazards/Risks, Attention and Human Factors
4. Week	Risk Factors
5. Week	Hierarchy of Controls and Transmission of Hazards
6. Week	Fire and Fire Protection, Ergonomics
7. Week	Midterm
8. Week	Occupational Health and Safety in Construction Workplaces, Occupational Health and Safety in Manual Lifting and Transportation Work, Occupational Health and Safety in High-altitude Work
9. Week	Occupational Health and Safety in Mining Workplaces, Occupational Health and Safety in Working in Pressure Vessels
10. Week	Occupational Health and Safety in Agricultural Areas, Occupational Health and Safety in Indoor Workplaces
11. Week	Warning Inspection, Accident Investigation and Report
12. Week	Personal Protective Equipment, Emergency Management at Workplaces
13. Week	Occupational Hygiene, Health Surveillance and Occupational Diseases
14. Week	The Controls to be Carried Out in Terms of Occupational Safety and the Documents to be Issued, the International Ethical Rules for Occupational Health and Safety Professionals

In order to compare the contents of the same lectures of different universities Table 2 is proposed for the evaluation.

When the tables above are examined, it may be resulted that the course contents differ among the universities apart from some major topics such as fire and fire protection, risk assessment, OHS in confined working areas, etc. In addition, these syllabi showed lack at topics such as chemical labeling, safety precautions against hazardous chemicals, chemical laboratory safety, that reveal vital importance for chemical engineering students.

These observations may be interpreted that OHS course should be customized according to different departments of the engineering faculties increasing the efficiency of the professional life and enabling the students to gain more knowledge about their field of work and occupational safety. As the most important target of the lecture is to have OHS culture, the benefits of the lecture will be in harmony with the professional life. Thus, it would be a success for the professional life to make chemical engineers gain awareness of the possible risks in their own working areas and be informed about preventing possible accidents. Also, this point of view may be applied in other departments of the engineering faculties considering their priorities.

3. Impacts of OHS course

The definition of "Occupational Accident" may vary depending on different organizations or legislations, but the underlying meaning remains the same. According to the World Health Organization (WHO), it is described as an event that is not planned in advance and often leads to personal injury, equipment damage, and a temporary halt in production [13]. The International Labor Organization (ILO) defines it as an unexpected and unplanned event that causes specific harm or injury [14]. In Law No. 6331 on Occupational Health and Safety, it is defined as an event resulting in death or a mental or physical disability, occurring in the workplace or due to work execution [15]. While definitions may differ, occupational accidents are essentially unexpected situations causing personal or financial harm. However, it is important to note

that work accidents can be prevented. In such cases, Occupational Health and Safety (OHS) training plays a crucial role in safeguarding individuals working in hazardous areas, including chemical engineers.

Chemical engineers undertake various tasks such as process design, optimization, quality assurance, safety, and environmental quality. They work in laboratory settings as well as chemical production facilities. Project engineers operate in engineering offices, while business engineers work directly in the business field. The scope of work for chemical engineers is vast, including industrial plants, labs, project offices, import-export companies, and various sectors such as petrochemicals, automotive, pharmaceuticals, and more. The risks and potential occupational accidents can differ depending on the equipment used, processes involved, and work environment. Therefore, OHS expertise is crucial for chemical engineers to ensure the safety of themselves and their co-workers. Especially for those in managerial positions, it is essential to inform and raise awareness among their subordinates because protecting lives and ensuring safety is of utmost importance.

Table 3. Chemicals and chemical products manufacturing sector 2010-2021 occupational accidents SSI records [16]

Years	Male	Female	Total
2010	789	44	833
2011	717	47	764
2012	691	53	744
2013	1662	1860	3522
2014	1608	192	1800
2015	1754	230	1984
2016	1914	276	2190
2017	2495	382	2877
2018	2927	461	3388
2019	3269	525	3794
2020	3719	690	4607
2021	4588	743	5331

In other words, the impact of occupational health and safety training for chemical engineers cannot be solely assessed based on occupational accident statistics within their profession. To comprehensively address this impact, it is necessary to analyze the occupational accident data of employees working alongside chemical engineers. In this study, the occupational accident data from the Social Security Institution (SSI) in the chemical and chemical product manufacturing sector between 2010 and 2021 were analyzed, tabulated (Table 3), and interpreted.

In order to accurately interpret occupational accidents, it is crucial to consider multiple parameters. Factors such as the sector's development, the number of workers involved, and the reliability of accident data must be carefully evaluated during the analysis. For instance, according to records declared by SSI, only one out of every ten work accidents in Türkiye is reported [16]. Thus, considering this data, it is possible to draw the following conclusions.

Comparing records from previous years with more recent ones, it is evident that occupational health and safety (OHS) has gained prominence and significance. The chemical industry, which experienced a growth rate of 18.54% in 2019, serves as a prime example of this trend [17]. Thanks to the implementation of OHS laws, employees in this expanding sector are being increasingly protected. Analyzing the data presented in the table, it becomes apparent that there was a significant decline in work accidents after the OHS Law came into effect in 2012. This suggests that prior to this, work accidents were not given adequate attention, and records were not being kept properly.

However, looking at the data after 2012, there is a clear decrease in accidents, which can be attributable to the impact of the OHS Law. Although the number of occupational accidents appears to have increased after the introduction of the compulsory OHS course in 2015, when considering the sector's growth and increased employment, it can be argued that there is a positive momentum in the field of occupational health and safety within the chemical sector.

In a survey conducted with students enrolled in occupational health and safety courses, the majority answered negatively to questions such as "Do you have knowledge about the OHS Law No. 6331?" and "Are you aware of your legal rights in case of workplace accidents?".

However, they responded positively to questions like "Does a focus on OHS lead to increased work efficiency and quality?" and "Should every workplace provide OHS training to workers before they start their jobs?" [18]. In another study comparing students who did and did not take OHS courses, similar questions were asked, and it was observed that students who completed the course demonstrated greater awareness. These results indicate that students gain an understanding of the importance and culture of OHS through these courses. However, despite their interest in the subject matter, students still lack sufficient knowledge regarding the OHS Law and their legal rights. This underscores the need for an improved content in the course material.

4. Customizing OHS course for chemical engineering department

Chemical engineering is widely acknowledged for its extensive practical applications within the field. As part of their academic curriculum, students undergo laboratory courses that provide them within valuable hands-on experience, working extensively with a diverse range of chemicals. It is important to note that these laboratories house an array of potent acids, bases, and other hazardous or irritating substances. Therefore, students must exercise utmost caution when handling these chemicals and comply strictly with Occupational Health and Safety (OHS) regulations [19-21].

Additionally, it is imperative for students to acquire comprehensive knowledge and skills to respond appropriately in the event of accidents or damage to laboratory materials. A thorough review of the existing studies highlighted certain deficiencies in the OHS course specifically tailored for chemical engineering students, particularly in relation to laboratory equipment and chemical aspects [22-25]. Addressing these gaps in curriculum design is crucial, as chemical engineers entering the professional world must possess a thorough understanding of occupational safety and risk mitigation.

By incorporating greater customization into the Occupational Health and Safety (OHS) course to meet the precise needs of chemical engineering, its efficacy can be substantially bolstered. These enhancements will not only help alleviate potential workplace hazards for prospective employees but also foster the cultivation of exceptionally skilled practitioners in this field. These findings carry profound implications for chemical engineers, as they will be equipped to effectively handle real-life situations and facilitate a secure work environment within their respective industries.

5. Conclusion

In summary, our investigation focused on evaluating the efficacy and sufficiency of the Occupational Health and Safety (OHS) course for chemical engineers, as well as the course's subsequent impact on their professional trajectories. This research was motivated by a recognized gap in the literature concerning the influence of the OHS course on both chemical engineers and the chemical industry at large.

Through collaboration with the Union of the Chamber of Chemical Engineers, we engaged in a series of interviews to address this gap comprehensively. Furthermore, our analysis incorporated accident statistics spanning from 2010 to 2021 within the chemical and chemical products industry, sourced from SSI (Social Security Institution). This meticulous data scrutiny enabled us to form a holistic perspective on the potency and effectiveness of the OHS course within the domain of chemical engineering.

The outcomes of our study revealed that the OHS course is indeed successful in cultivating a general awareness surrounding occupational health and safety matters. However, our findings also illuminated noteworthy deficits in the course's theoretical content. Thus, we recommend a thorough revision of the curriculum to rectify these short comings and amplify its overall impact.

Additionally, our exploration indicated that positioning the OHS course during the final two semesters of the undergraduate program yields superior efficiency. This outcome prompts a call for universities to revisit their programs and align the OHS course accordingly.

Furthermore, as part of curriculum reform, we emphasize the importance of tailoring the course content according to the distinct departments within the Faculty of Engineering. Notably, within the realm of chemical engineering, we propose the inclusion of subjects like adept handling of laboratory apparatus, adherence to chemical safety protocols, proficient chemical labeling practices, and preemptive measures against hazardous chemicals. By weaving these elements into the curriculum, the competencies of future chemical engineers can be significantly augmented, ultimately bolstering their capacity to address occupational health and safety concerns in their professional capacities.

Article Information Form

Authors' Contribution
Fatos Ayca Ozdemir Olgun who is the corresponding author of this study, designed the major outline of the study, contributed at writing and revision. Sumeyye Dilek conducted the scientific research, wrote the main text and contributed at the revision of the manuscript.

The Declaration of Conflict of Interest/ Common Interest
No conflict of interest or common interest has been declared by authors.

Artificial Intelligence Statement
No artificial intelligence tools were used while writing this article.

Copyright Statement

References

[1] A. I. Dewı, E. Wardani, N. Z. Umami, "Occupational Health and Safety Management System and Work-related Accidents Among Hospital Nurses," Enfermería Clínica, vol. 32, no. 2, pp. 6-10, 2022.

[2] N. Z. Umami, "Literature Review: Relationship Between Occupational Health and Safety Knowledge with Work Accidents," Muhammadiyah International Public Health and Medicine Proceeding, vol. 2, no. 1, pp. 458-464, 2022.

[3] B. Doğan, C. Yalçınkaya, M. G. Balcı, "Türkiye'de Mühendislik Fakültelerinde İş Sağlığı ve Güvenliği Eğitimi," Mühendis ve Makina, vol. 58, no. 685, pp. 1-15, 2017.

[4] Y. Qian, S. Vaddiraju, F. Khan, "Safety education 4.0–A critical review and a response to the process industry 4.0 need in chemical engineering curriculum," Safetyscience, vol. 161, 106069, 2023.

[5] S. Topgüland Ç. Alan, "Öğrencilerin İş Güvenliği ve İş Güvenliği Eğitimi Algısının Değerlendirilmesi," Süleyman Demirel Üniversitesi İktisadi ve İdari Bilimler Fakültesi Dergisi, vol. 22, no. 2, pp. 587–598, 2017.

[6] A. T. Özgüler, K. Kaya, B. Kağızmanlı, M. Altuğ, "Mühendislik Fakültesi Öğrencilerinin İş Sağlığı ve Güvenliği Eğitimi Yeterliliği," Eğitim ve Öğretim Araştırmaları Dergisi, vol. 5, no. 10, 2016.

[7] İş Sağlığı ve Güvenliği Kanunu (2012, 6, 20.) [Online]. Available: https://casgem.gov.tr/poco-pages/mevzuatlar/6331-say%C4%B1l%C4%B1-%C4%B1s-ve-guvenl%C4%B1g%C4%B1-kanunu/

[8] G. Sönmez, "Yükseköğretim Kurumlarında Zorunlu Olarak Okutulan İş Sağlığı ve Güvenliği Dersleri İçin Müfredat Önerisi," İstanbul Aydın Üniversitesi Eğitim Fakültesi Dergisi, vol. 7, no. 1, pp. 147–162, 2021.

[9] K. Salsabila, (2023). Occupational Health and Safety (OHS) Planning at the Facilities and Infrastructure Used by Students of the Faculty of Engineering, Universitas Andalas (Doctoraldissertation, Universitas Andalas).

[10] P. M. Arezes, P. Swuste, "Occupational Health and Safety post-graduation courses in Europe: A general overview," SafetyScience, vol. 50, no. 3, pp. 433-442, 2012.

[11] Gazi Üniversitesi. (2019, Feb. 6). ISG402 İş Sağlığı ve Güvenliği II, OHS402 Dersi Programı [Online] Available: https://mf.gazi.edu.tr/view/GetMainAnno uncementPage/219618/isg402-Is-sagligi-ve-guvenligi-ii-ohs402-dersi-programi?type=1

[12] Altınbaş Üniversitesi. Altınbaş Üniversitesi Bilgi Paketi / Ders Kataloğu [Online]Available: https://ects.altinbas.edu.tr/DerecePrograml ari/Ders/1/4197/32292/54908/1

[13] World Health Organization. (2019, Sep. 17). Occupational Health [Online]Available: https://www.who.int/health-topics/occupational-health

[14] International Labour Organization. (2019) Safety and health at work [Online] Available: https://www.ilo.org/topics-and-sectors/safety-and-health-work

[15] 6331 Sayılı İş Sağlığı ve Güvenliği Kanunu, Tanımlar Başlıklı 3. Maddesi, g) bendi.

[16] Sosyal Güvenlik Kurumu. Yıllık İstatistik [Online]Available: https://www.sgk.gov.tr/Istatistik/Yillik/fcd 5e59b-6af9-4d90-a451-ee7500eb1cb4

[17] M. Tarim, "Kimya Sektöründe İş Kazaları ve Meslek Hastalıkları," İstanbul Ticaret Üniversitesi Fen Bilimleri Dergisi, vol. 16, no. 32, pp. 49–64, 2017.

[18] Habertürk. (2020, Jan. 08). AB ülkeleri ihracatta başı çekti [Online] Available: https://www.haberturk.com/kimya-sektorunde-2023-hedefi-30-milyar-dolar-2556786-ekonomi

[19] A. T. Özgüler, T. Koca, "Meslek Yüksekokullarında İş Sağlığı ve Güvenliği Eğitiminin Gerekliliği," Ejovoc (Electronic Journal of Vocational Colleges), vol. 3, no. 4, pp. 15–20, 2013.

[20] Ş. Yavuz, "Organik Kimya Laboratuvarında Kullanılan Kimyasalların İş Sağlığı ve Güvenliği Açısından Zararlarının İncelenmesi," Ohs Academy, vol. 3, no. 3, pp. 221-229, 2020.

[21] Ş. Yılmaz, M. Bilici, "Mühendislik Fakültesi Bünyesinde Bulunan Laboratuvarlarda İş Sağlığı ve Güvenliği," Ohs Academy, vol.3, no.2, pp. 102–113, 2020.

[22] M. N. K. Öner, "Kimya Eğitiminde Laboratuvar Güvenliği Kültürünün Yerleştirilmesi," İSG Akademik, vol. 2, no. 1, pp. 15–25, 2020.

[23] V. Goodwin, D. Cobbin, P. Logan, "Examination of the occupational health and safety initiatives available within the chemistry departments of Australian universities," Journal of chemical education, vol. 76, no. 9, pp 1226-1229, 1999.

[24] A. U. Walters, W. Lawrence, N. K. Jalsa, "Chemical laboratory safety awareness, attitudes and practices of tertiary students," Safetyscience, vol. 96, pp. 161-171, 2017.

[25] A. Ozsahin, M. Demir, M. Zencir, S. Demir, I. Kaleli, "Safety awareness among laboratory workers," Advances in Therapy, vol. 23, pp. 414-420, 2006.